

Genetic analysis of genes linked to lumen formation in  
the zebrafish vasculature

**Inauguraldissertation**

zur Erlangung der Würde eines Doktors der Philosophie

vorgelegt der

Philosophisch-Naturwissenschaftlichen Fakultät der Universität Basel

von

Daniel Heutschi

Basel, 2023

Genehmigt von der Philosophisch-Naturwissenschaftlichen Fakultät auf Antrag von

Erstbetreuer: Prof. Dr. Markus Affolter

Zweitbetreuer: Prof. Dr. Alexander Schier

Externe Expertin: Prof. Dr. Anna Jazwinska

Basel, 14.12.2021

Prof. Dr. Marcel Mayor

Dekan der Fakultät

# Table of contents

1	Abstract	1
2	Introduction	2
2.1	Zebrafish as a model system for development	2
2.2	Early development of zebrafish	2
2.3	Vasculogenesis	4
2.4	Tip-cell selection and migration	5
2.5	Anastomosis and cellular rearrangement	6
2.6	Lumen formation in the vasculature and other systems	8
2.6.1	<i>de novo</i> lumen formation	8
2.6.2	Lumen formation in trachea and vasculature	8
2.7	The multiple roles of Rab7	12
2.7.1	Rab-proteins	12
2.7.2	The Rab cycle	12
2.7.3	Structure and important domains of Rab7	13
2.7.4	The effectors of Rab7 and their function	16
2.7.5	Differences between <i>rab7a</i> and <i>rab7b</i> function	17
2.8	Endocytosis	18
2.8.1	Vesicle formation	18
2.8.2	Uncoating and the early endosome	18
2.8.3	The Recycling back to the plasma membrane	18
2.8.4	The Late endosome and Lysosome	19
2.8.5	Lysosome related organelles	21
2.8.6	Lysosome related organelles in the zebrafish vasculature	21
3	Aims of the thesis	22
4	Results: Chapter I	23
4.1	Genetic analysis of <i>rab7</i> mutants in zebrafish	23
4.1.1	Abstract	24
4.1.2	Introduction	24
4.1.3	Results	26
4.1.4	Discussion	41
4.1.5	Material and Methods	43
4.1.6	Supplementary Data	50
5	Results: Chapter II	53
5.1	Generation and preliminary screening of <i>unc13d</i> mutants	53

5.1.1	Generation of <i>unc13d</i> mutants	54
5.1.2	Analysis of survival and vascular development of <i>unc13d</i> mutants	57
6	Material and Methods	59
6.1	Materials	59
6.1.1	Buffer, Media and Solutions	59
6.1.2	Antibiotics & Bacteria	61
6.1.3	Basic Material	62
6.1.4	Injection & Mounting Material	63
6.1.5	Fish lines	64
6.1.6	Plasmids	64
6.1.7	Primers	65
6.1.8	Morpholinos	66
6.1.9	Reference Peptides for MS	66
6.1.10	Microscopes and binoculars	67
6.2	Methods	68
6.2.1	Molecular biology protocols	68
6.2.2	Zebrafish protocols	70
6.2.3	Injections	73
6.2.4	General experimental setup for Image acquisition	74
6.2.5	Targeted MS of <i>rab7</i> proteoforms	75
6.2.6	Assembly of phylogenetic tree	76
6.2.7	Transcriptomics data	77
7	Discussion	78
7.1	Identification and description of a novel <i>rab7</i> gene	78
7.2	Generation of <i>rab7</i> mutant alleles	79
7.3	Viability of <i>rab7</i> mutant alleles	80
7.4	Maternal contribution of <i>rab7</i>	80
7.5	Lumen formation in <i>rab7</i> single and double mutants is only slightly impaired.	81
7.6	<i>rab7</i> single and double mutants are capable of lumen fusion	82
7.7	<i>rab7</i> single and double mutants show difference in vesicle size but not number.	83
7.8	Conclusion and outlook on the role of Rab7 in the zebrafish vasculature	83
7.9	Generation and analysis of <i>unc13d</i> <sup>ubs54</sup>	84
8	Contributions to publications	86
8.1	Junction-based lamellipodia drive endothelial cell rearrangements in vivo via a VE-cadherin-F-actin based oscillatory cell-cell interaction.	86
8.2	Building the complex architectures of vascular networks: Where to branch, where to connect and where to remodel?	100

9	Acknowledgements _____	118
10	Appendix _____	120
10.1	<i>rab7</i> knockdown leads to vascular phenotypes _____	120
11	References _____	122
12	Curriculum Vitae _____	132



## 1 Abstract

Formation of a functional vascular network is a crucial step in vertebrate early development. After formation of the first two major vessels, the dorsal aorta and the posterior cardinal vein, the vasculature expands through sprouting angiogenesis. Vascular network formation requires the interconnection of individual sprouts by the process of anastomosis. This process can be subdivided into different steps: initial filopodial contact, junction formation and lumen formation. With respect to lumen formation, two distinct mechanisms have been described: Transcellular lumen formation – driven by apical membrane invagination - and cord hollowing, which requires by cell rearrangements. It was proposed that during transcellular lumen formation, the growth of the invaginating apical membrane is dependent on vesicular trafficking, since punctae of the apical membrane marker mCherry-CAAX were seen to disperse in the growing apical membrane. It was shown that the observed vesicles colocalize with late endosomal/lysosomal markers Lamp2, Rab9 and Rab7, therefore, labeling them as part of the late endocytic/ lysosomal pathway. An essential step during transcellular lumen formation is the fusion between the apical membrane within the endothelial cell. Previous work in tracheal lumen formation in *D. melanogaster* identified the tethering factor *staccato* as a critical component of this process. In this study, we want to further investigate the role of late endocytic trafficking for lumen formation in the zebrafish vasculature. We therefore generated mutant lines for all three *rab7* paralogues and the zebrafish homologue of *stac*, *unc13d*. Targeted mass spectrometry validated the isolated *rab7* mutant alleles and showed that all wild-type protein and residual fragments thereof were absent in the respective mutant. *rab7* single and double homozygous mutants are viable and fertile but triple homozygous *rab7* mutants are lethal. Taken together, the phenotypic analysis of single and compound mutants showed, that *rab7a* and the newly described copy *rab7bb* are functionally redundant and that the third copy *rab7ba* seems to have a distinct function, potentially similar to what was proposed for mammalian *rab7b*. Furthermore, of the three *rab7* genes in zebrafish, at least two provide maternal contribution and embryos maternal homozygous for these two alleles show phenotypes in the yolk of laid eggs. This Phenotype resembles what was previously reported in *C. elegans*. However, none of the mutants displayed any strong phenotypes linked to lumen formation or lumen fusion, but a conclusion on the role of this pathway cannot be drawn due to the early death of triple homozygous embryos, or the presence of additional *unc13* genes. In order to be able to follow *rab7* depleted endothelial cells and its role on lumen formation, inducible systems are required.

## 2 Introduction

### 2.1 Zebrafish as a model system for development

The zebrafish (*danio rerio*) has been used as model organism to study developmental processes since the early 1980s, when it has been introduced by George Streisinger at the University of Oregon (Streisinger, Walker et al. 1981). While initially, the easy genetical manipulability and its large spawn number, as well as the extrauterine development were the biggest benefits to study zebrafish development (Grunwald, Kimmel et al. 1988), it soon became an important model organism for live imaging due to its transparency (Fetcho, Cox et al. 1998). The discovery of GFP (Chalfie, Tu et al. 1994) and the generation of transgenic fluorescent lines allowed to study developmental processes down to single cell resolution (Megason and Fraser 2003). As vertebrates, zebrafish share many homologous genes with humans and has rapidly turned into a suitable model to study the development of several organs or has been used to model human diseases (Glass and Dahm 2004, Legendijk, Yap et al. 2014, Bournele and Beis 2016).

### 2.2 Early development of zebrafish

To form a functioning organism from a symmetrical single cell, a tightly controlled network of signalling factors is necessary. Early establishment of asymmetry in zebrafish can already be seen in Stage-III of oogenesis, where the sperm entry site is predefined by a single specialized follicle cell at the animal pole. But already before, molecular mechanisms are used to store maternal mRNAs at opposite, animal (A) or vegetal (V), poles. So are *cycB1*, *pou2*, *notch*, *zorba* and *vg1* mRNAs localized at the animal pole, whereas *dazl*, *wnt8*, *bruno-like*, *syntabulin* and *grip2a* mRNAs are localized at the vegetal pole (Howley and Ho 2000, Escobar-Aguirre, Elkouby et al. 2017). The main organizer of A-V polarity and therefore mRNA distribution in the oocyte is the gene *buckyball* (*buc*). When *buc* function is lost, oocytes fail to establish A-V polarity and instead of only one defined micropyle, several sperm entry sites are established (Ge, Grotjahn et al. 2014) (Fig 1A-B).

This early polarity influences the second axis that is formed in the zygote. On the one hand, the transcription factor  $\beta$ -catenin, which is evenly distributed in the cytoplasm during oogenesis, becomes dorsally restricted and enters the nucleus after cell divisions have been initiated and activates genes encoding BMP and Wnt antagonists such as *chordin* and *dickkopf*. On the other hand, the expression of *vox* and *vent* by BMP inhibits ventral cells to express these antagonists. Finally, the *nodal* homologues in zebrafish, *sqnt* and *cyc*, define the marginal-most edge of the blastomere to become the future mesoderm (Schier 2001). This mesoderm activation has later been shown to be mediated via Elabela (ELA).



ELA acts downstream of Nodal to drive late onset of mesodermal specification and the migration of mesoderm and endoderm towards the vegetal pole during gastrulation. The two germ layers are coupled via Cxcr4-tethering (Norris, Pauli et al. 2017). Loss of Cxcr4a releases this tether and results in excessive animal pole-directed migration of endodermal cells, while mesodermal cell migration is unaffected (Mizoguchi, Verkade et al. 2008) (Fig 2C-D).

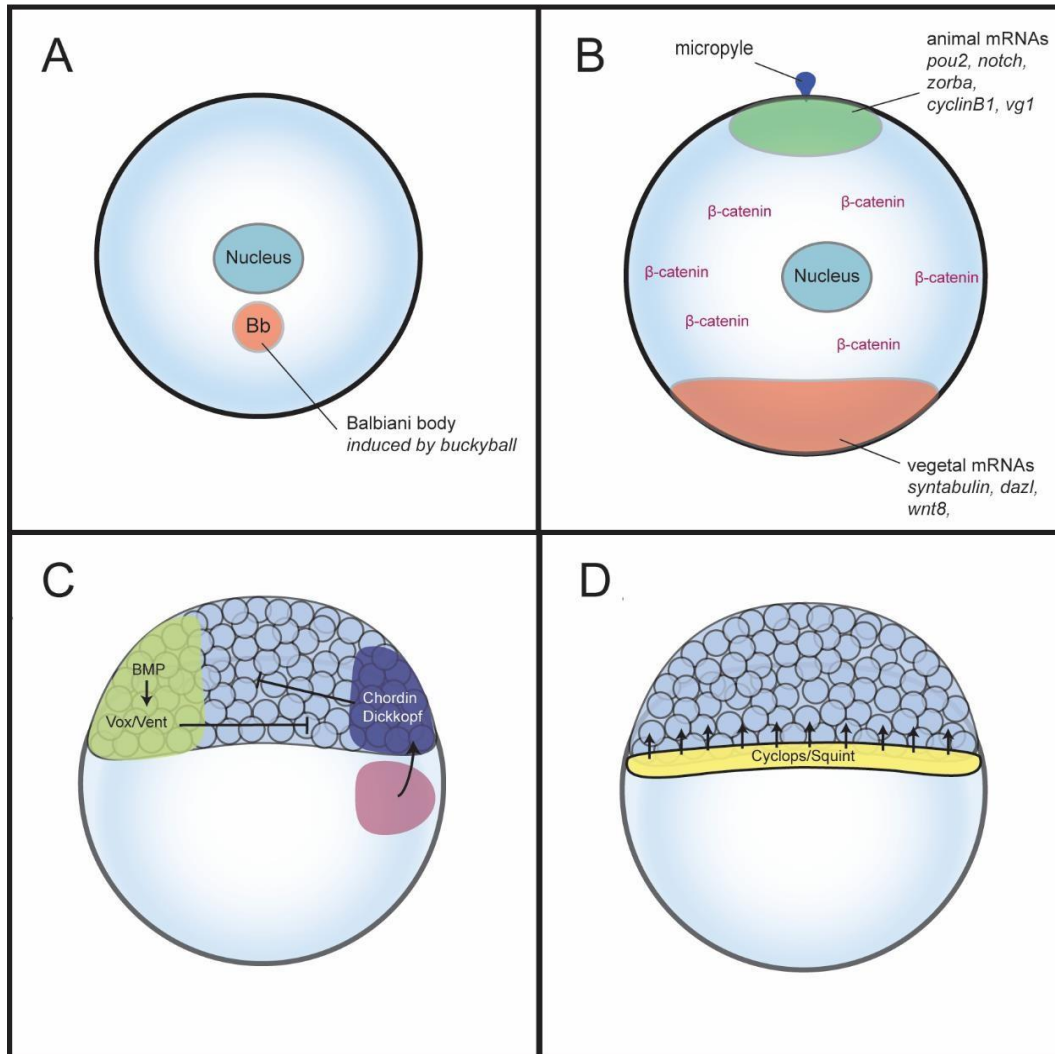


**Figure 1** Early organization of the zebrafish egg and embryo

**A** Schematic of animal-vegetal cytoplasmic domain formation and spatiotemporal mRNA localization during zebrafish oogenesis. Animal (green) and vegetal (red) transcripts are shown. The early stage I oocyte polarizes and the nucleus becomes asymmetric as Balbiani body (Bb) components first begin to aggregate during meiosis. **B** Later the Bb disassembles at the oocyte cortex, with vegetal mRNAs becoming anchored to the cortex (early pathway), thus forming a vegetal cytoplasmic domain. In stage III oocytes, additional mRNAs localize to the vegetal pole (late pathway). The localization of transcripts to the opposite pole establishes an animal cytoplasmic domain. Additional determination of the sperm entry site (micropyle) at the vegetal pole of the egg. **C** Dorsal restriction of β-catenin induces induction of BMP antagonists *chordin* and *dickkopf*. BMP induced expression of Chordin and Dickkopf antagonists *vox* and *vent*. **D** Nodal induced specification of mesendodermal tissue from the yolk-blastodisc border.

## 2.3 Vasculogenesis

The earliest precursors of the vascular system are found in the mesoderm, more specifically in the posterior lateral mesoderm (Zhong, Childs et al. 2001). One of the earliest specification events of endothelial cell fate has recently been shown to be the activation of *cloche/npas4l*, without which the previously well-established endothelial and hematopoietic cell-specific transcription factors *etv2* and *tal1* are absent (Reischauer, Stone et al. 2016). Once the first endothelial cells have been specified, they migrate towards the embryonic midline, where they coalesce and form the first embryonic vessels, the dorsal aorta (DA) and the cardinal vein (CV). Arterial and venous progenitors are known to emerge at different times and distinct locations, with arterial progenitors originating earlier and closer to the midline than venous progenitors. These lines of endothelial cells migrate to the midline in two waves, with the medial arterial progenitors migrating first, followed by the laterally located venous progenitors (Kohli, Jennifer et al. 2013). This process has been described to be reliant on vascular endothelial growth factor (VEGF) (Verma, Bhattacharya et al. 2010). However, more recent evidence shows that the signalling molecules ELA and Apelin (APLN) and their corresponding receptors, *Aplnra* and *Aplnrb*, show much stronger effects on migrating angioblasts when deleted (Helker, Schuermann et al. 2015) (Fig2). Nonetheless, chemical inhibition of VEGF signalling using a tyrosine kinase inhibitor in zebrafish embryos resulted in the loss of overall endothelial marker expression, including the loss of expression of pan-endothelial marker *Fli1a*, arterial marker *Ephb2a* and venous marker *Flt4* (Chan, Bayliss et al. 2002) These results argue that VEGF signalling plays two distinct roles in vasculogenesis separated from migration: overall endothelial differentiation and arteriovenous specification, respectively, which differ in the level and timing of VEGF signalling (Casie Chetty, Rost et al. 2017).

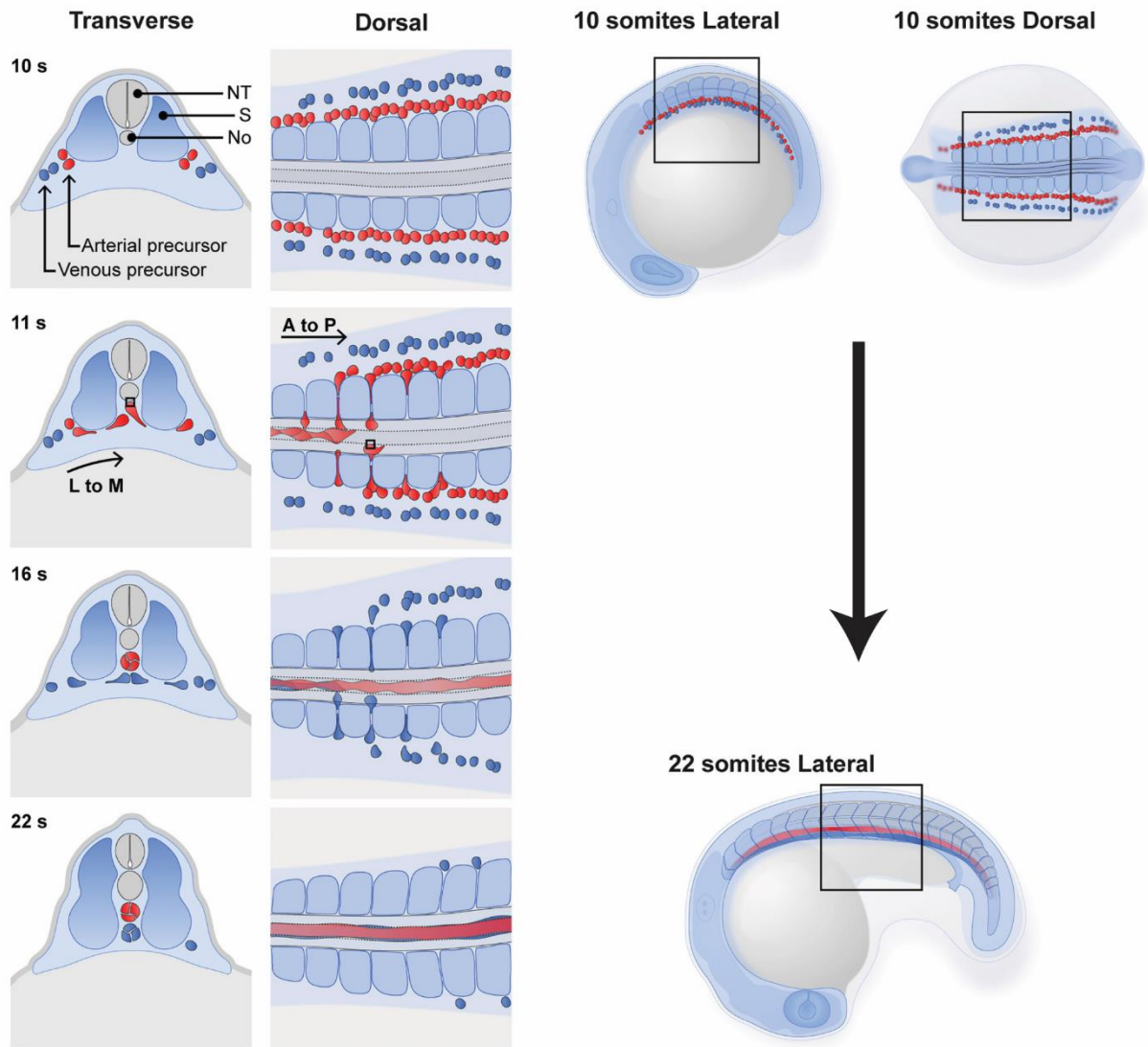


**Figure 2** Origin and migration of early angioblasts during vasculogenesis

Lateral and dorsal views of 10 and 22 somite embryos illustrating arterial (red) and venous (blue) precursor cells. Transverse, lateral, and dorsal views of vasculogenic events between the 10 and 22 somite stage. At the 10 somite stage, arterial precursors begin to migrate medially, in between somites and toward the notochord. A few hours later, venous precursors follow. Transverse embryo sections. At the 22 somite stage, arterial and venous endothelial cells have aggregated into distinct cords ventral to the notochord. Lumenization depends on the activities of *Egfl7*, *Scf/Tal1*, and *Amotl2*, and occurs just prior to the onset of blood flow. At 26 hpf, DA and PCV contain blood cells. A, anterior; DA, dorsal aorta; hpf, hours post fertilization; L, lateral; M, medial; No, notochord; NT, neural tube; P, posterior; PCV, posterior cardinal vein; s, somite. Figure adapted from Hogan and Schulte-Merker (2017)

## 2.4 Tip-cell selection and migration

After specification of endothelial cells and their assembly into the first major vessels, most of the remaining blood circulatory system is formed via sprouting angiogenesis (Risau 1997, Wacker and Gerhardt 2011, Betz, Lenard et al. 2016). In this process, endothelial cells from the pre-existing vessels are activated by VEGF signalling. Activation of signalling in tip cells via VEGF-A binding to VEGFR-2 results in proliferation and migratory behaviours via Erk kinase signalling (Shin, Beane et al. 2016) and Plcy (Lawson 2003). Furthermore, VEGF signalling leads to high Delta-like-4 (Dll4) secretion, which downregulates

VEGFR expression in neighbouring cells, making them irresponsive to VEGF-A signalling and thus preventing hypersprouting (Blanco and Gerhardt 2013). During migration, the vessel sprouts are guided by chemokines. In zebrafish ISVs, for example, vessels only grow in between the somites, although VEGF-A is expressed along the entire midline. This migration is negatively controlled by Semaphorin3 (Sem3a) expression of somitic cells. Sem3a is recognized by the PlexinD1 receptor expressed in endothelial cells, and prohibits them from migrating into the somitic tissue (Torres-Vázquez, Gitler et al. 2004). PlexinD1 signalling appears to act via the VEGFR-1 (Flt1 in zebrafish). Its soluble variant sFlt1 is absent in endothelial cells in *plexinD1* mutants. It has been postulated that sFlt1 depletes the pool of accessible VEGF to titrate its signalling potential (Zygmunt, Carl et al. 2011). Efficient migration of sprouts is also dependent on stalk cell elongation. If endothelial cells lack Vascular endothelial (VE) cadherin, stalk cells fail to elongate; sprouts that normally show elongated junctions through the entire stalk, consist of only one cell for the majority of their length, with a cluster of non-elongated cells at the bottom of the stalk. In the most severe cases, stalk and tip cells detach from each other and the stalk retracts (Sauteur, Krudewig et al. 2014). The VE-cadherin dependant elongation of stalk cells has been shown to be driven by junction-based lamellipodia (JBL), a ratchet-like behaviour of endothelial cell junctions, in which a secondary more distal junction is established before the primary junction merges with the distal end. This ratchet mechanism is dependent on actin filaments and more specifically on VE-cadherin dependant anchoring of the junction to the actin cytoskeleton (Paatero, Sauteur et al. 2018).

## 2.5 Anastomosis and cellular rearrangement

The final step of sprouting angiogenesis is anastomosis. During anastomosis, tip cells of two different sprouts form contacts and ultimately connect with each other. To maintain initial contacts, VE-cadherin and ZO-1 are deposited at the contact site in order to establish a new cell junction. In the absence of VE-cadherin, tip cells fail to efficiently recognize each other, and initial junction formation is slowed down. The establishment of novel cell junctions is then followed by polarization of the cell, which can be observed by the deposition of apical markers, such as Podocalyxin, at the membrane between the newly formed junctional ring. Finally, the junctional ring elongates and tilts until the two tip cells are split, and a functioning multicellular vessel is established (Lenard, Ellertsdottir et al. 2013). During this process, the newly formed vessels need to be lumenized in order to be functionally integrated into the vascular network (Fig 3 “Anastomosis”).

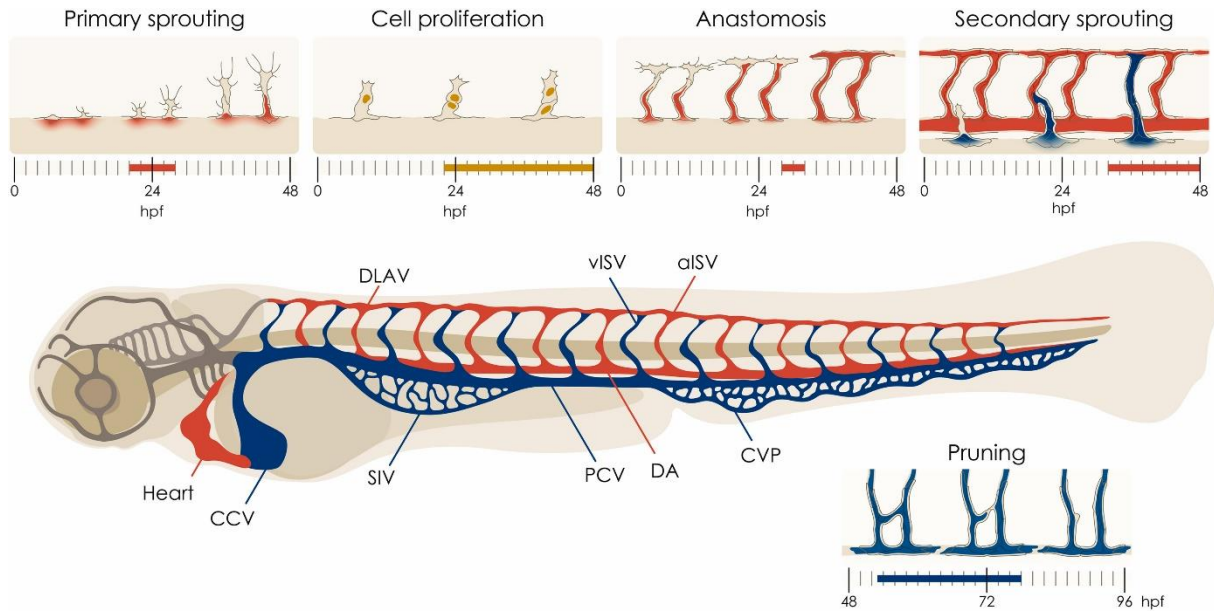


**Figure 3** Processes of vascular morphogenesis commonly studied in the zebrafish embryo.

A simplified schematic of the zebrafish trunk vasculature and blood flow pattern between 2 and 3 days post fertilisation (dpf). In the trunk region, arterial intersegmental vessels (aISVs, red) and venous ISVs (vISVs, blue) are indicated. At this stage the subintestinal vein (SIV) plexus and the caudal vein plexus (CVP) form ramified networks, which become simplified in later stages of development. The posterior cardinal vein (PCV) drains into the common cardinal vein (CCV) and the sinus venosus at the heart. From the heart the blood is pumped into the cranial and trunk arteries. Primary sprouting: At around 1 dpf, primary sprouts emerge from the DA to form primary ISVs. The sprouts extend dorsally driven by endothelial cell (EC) migration and proliferation. Anastomosis (blood vessel fusion): This process is essential to generate vascular networks. In the example shown, two tip cells of neighboring primary ISV sprouts interact and generate the dorsal longitudinal anastomotic vessel (DLAV). Secondary sprouting: At around 1.5 dpf the PCV forms secondary sprouts, which will contribute to the venous and the lymphatic vasculature. In the zebrafish trunk about 50% of the secondary sprout anastomose with a primary ISV, transforming it into a vISV. The primary ISV-DA connection is pruned. Pruning: In some vascular plexi such as the SIV plexus, supernumerary vessel segments are removed to redirect blood flow or to simplify blood flow patterns. Figure from Phng and Belting (2021)

## 2.6 Lumen formation in the vasculature and other systems

### 2.6.1 *de novo* lumen formation

A lot of insight in *de novo* lumen formation has been gained by studying 3D cell cultures. Human umbilical vein endothelial cells (HUVECs), for example, can establish tubular structures with multicellular lumen via two processes that have been described: Cell hollowing or cord hollowing. During cell hollowing, the cells form large vacuoles via pinocytosis which eventually coalesce to form one continuous lumen (Sacharidou, Stratman et al. 2012). During cord hollowing, cells polarize upon contact with neighbouring endothelial cells and establish an apical domain, which eventually fuses with that of neighbouring complexes to form a continuous lumen (Tung, Tattersall et al. 2012). In all cases, formation of a lumen requires endothelial cells to polarize. In cell culture, this polarization relies strongly on  $\beta$ 1-integrin. Without Integrin interaction with the extracellular matrix (ECM), cells fail to polarize and lumen formation does not occur (O'Brien, Jou et al. 2001). Polarization leads to several changes of cytoskeletal dynamics. It has been shown that cytoskeletal organizers such as Rac1, RhoA, Cdc-42 and Arp2/3 all play a role in setting up polarity in MDCK cells (Bayless and Davis 2002, Davis and Bayless 2003). With cell polarity and cytoskeleton set up, vesicle trafficking can deliver apical determinants, such as Podocalyxin, to the apical membrane initiation site (AMIS). It has been shown that Rab GTPases Rab11A and Rab8A are required to deliver apical polarity proteins such as Cdc42, Crumbs, atypical protein kinase C (aPKC) and PAR3 to the AMIS (Bryant, Datta et al. 2010).

### 2.6.2 Lumen formation in trachea and vasculature

Similar events of lumen formation have been shown in *in vivo* models, in which the final step during the formation of a patent, branched network consists in the lumenization of the anastomosing cells. This process has been described in zebrafish to occur via two distinct mechanisms: cord hollowing and transcellular lumen formation. During cord hollowing, the junctional ring that has formed during anastomosis remodels while cells rearrange to form a multicellular vessel. This remodeling results in connecting and opening up of the apical patches formed at the initial contact sites during anastomosis and finally, in opening of the lumen in the multicellular vessel (Fig 4B). Transcellular lumen formation is a process that in zebrafish is driven by blood pressure and happens in vessels upon anastomosis before cellular rearrangement takes place. It has been shown that blood flow driven invagination of the apical membrane leads to inverse blebbing. These spherical deformations of the apical membrane are a result of the pressure in the lumen, and the cytoplasm of the cell reacts to these deformations by recruiting and contracting of the actin cytoskeleton around the apical blebs.

This process has been described to be a driving force of membrane invagination into the endothelial cells (Gebala, Collins et al. 2016). Eventually, the lumen progressively expands into the vessel through the tip cell, where the apical membranes must fuse with the apical patch of the initial contact site during anastomosis. Once these membranes have fused, the lumen progresses through the adjacent cell until the two luminal fronts meet (Fig 4A). (Herwig, Blum et al. 2011).

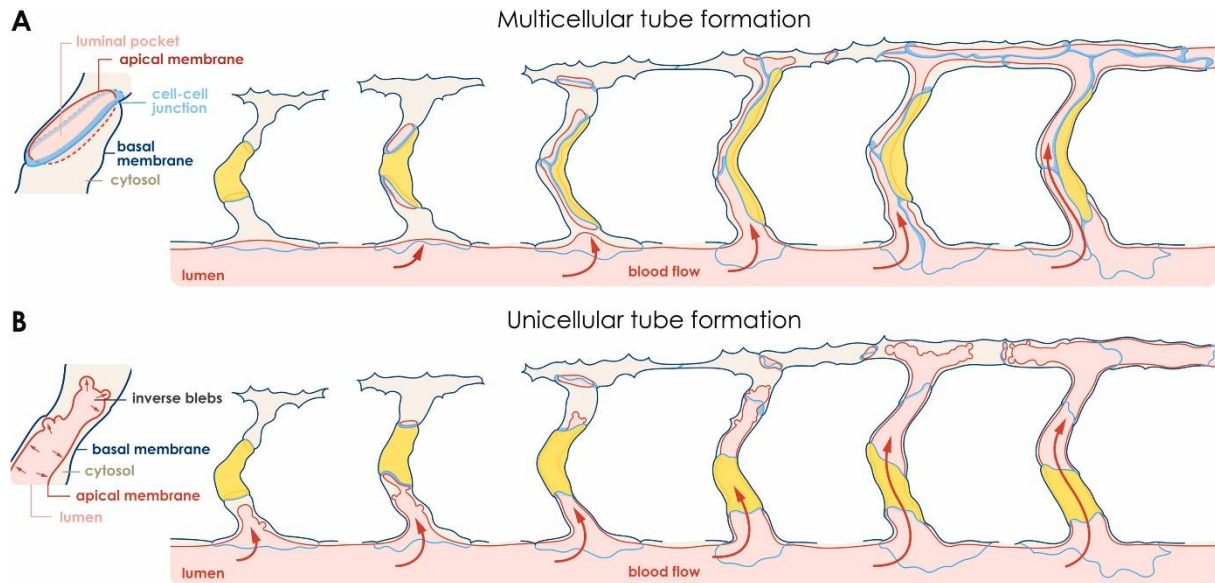


**Figure 4** Distinct morphogenetic processes generate lumens in primary ISVs.

During primary ISV sprouting, ECs are initially stacked behind each other. The cells are connected by junctional ring surrounding apically polarised membranes forming a local luminal pocket. Lumenisation of the ISV can occur in two different ways. (A) Multicellular tube formation by cord hollowing and cell rearrangement. In this process, the stalk cells elongate and move over each other in a convergent fashion, thus elongating the luminal pockets. Cell rearrangements lead to the formation of new contacts which cause the local lumens to merge in a multicellular configuration. (B) Unicellular tube formation by transcellular lumen formation. Alternatively, ECs may not rearrange. In this situation, blood pressure from the DA causes invagination of the apical cell membrane through the cytoplasm. Subsequent intra-cellular membrane fusion will occur and generate a hollow cell. Blood vessels generated by transcellular lumen formation are unicellular. Figure from Phng and Belting (2021)

This process shares striking similarities with lumen formation in the trachea of *Drosophila melanogaster*. In the trachea, the two fusion cells of neighbouring segmental branches also stabilize initial contacts via the deposition of junctional proteins and establish an apical domain in between this newly formed junction. The growing luminal tube is surrounded by a dense actin network. It is the interaction of this network with the luminal membrane via a protein complex comprising Moesin (Moe) and Bitesize that aids the incorporation of apical membrane material into the growing luminal tube (Jayanandanan, Mathew et al. 2014). Additionally,  $\alpha$ -tubulin, which labels newly formed microtubuli, can be found along the growing lumen. These cables run along the entire length of the fusion cells and are used for Rab35-dependent transport of membrane material to the growing tip of the lumen.

In tracheal fusion cells, the vesicle and microtubule-associated small GTPase Arf-like 3 (Arl3) directs exocytic vesicles to the fusion site (Kakihara, Shinmyozu et al. 2008). In a more recent study, the molecular understanding of how lumen fusion is regulated in terminal cells of *D. melanogaster* has been molecularly refined. In embryos mutant for the membrane tethering factor *staccato* (*stac*) (*munc13-4* in mammals or *unc13d* in zebrafish), the initial lumen forms and elongates but cannot fuse with the apical patch generated at the contact site and form a continuous, lumenized dorsal trunk. Interestingly, mutation in *arl3* show a similar discontinuous luminal phenotype, indicating a connection between *arl3* and *stac*. It has been shown that the observed Stac-positive punctae in fusion cells colocalize with late endosomal and lysosomal markers Rab7, Rab39 and Lamp1, indicating that lysosome related organelles (LRO) play a role in lumen fusion (Caviglia, Brankatschk et al. 2016). Furthermore, it could be shown that endogenously tagged YFP-Rab7 is strongly expressed in tracheal terminal cells, and that tracheal specific knockdown leads to an increased number of unfused dorsal branches. Consistent to Caviglia et al they saw the same effect also with Rab39. They could also show that this effect is maternal dependent, with the effect become stronger when mothers were homozygous for the YFP-tagged *rab7*. When screening overall morphology of the tracheal network in YFP-Rab knockdowns. Rab7 was the only screened Rab-protein that showed all five scored Phenotypes, like misguided terminal cells or unfused branches. However, when looking only at terminal cell morphology, Rab7 didn't show any of the scored phenotypes. They conclude that terminal cell specification is already altered before in Rab7 knockdowns and that these cells do not specify as terminal tracheal cells (Best and Leptin 2020). They showed in a second study, that guidance of terminal cells and luminal tubes is strongly dependent on late endocytic mediated actin cytoskeleton guidance, and that late endosomes always locate in front of the growing tube. They showed that Wash an actin nucleation factor localizes to late endosomes and when it is knocked-down they saw misguided tubes similar to loss of late endosomes. They showed that wash is recruited to late endosomes upon acidification and regulates the actin meshwork to guide tubule growth (Rios-Barrera and Leptin 2021).



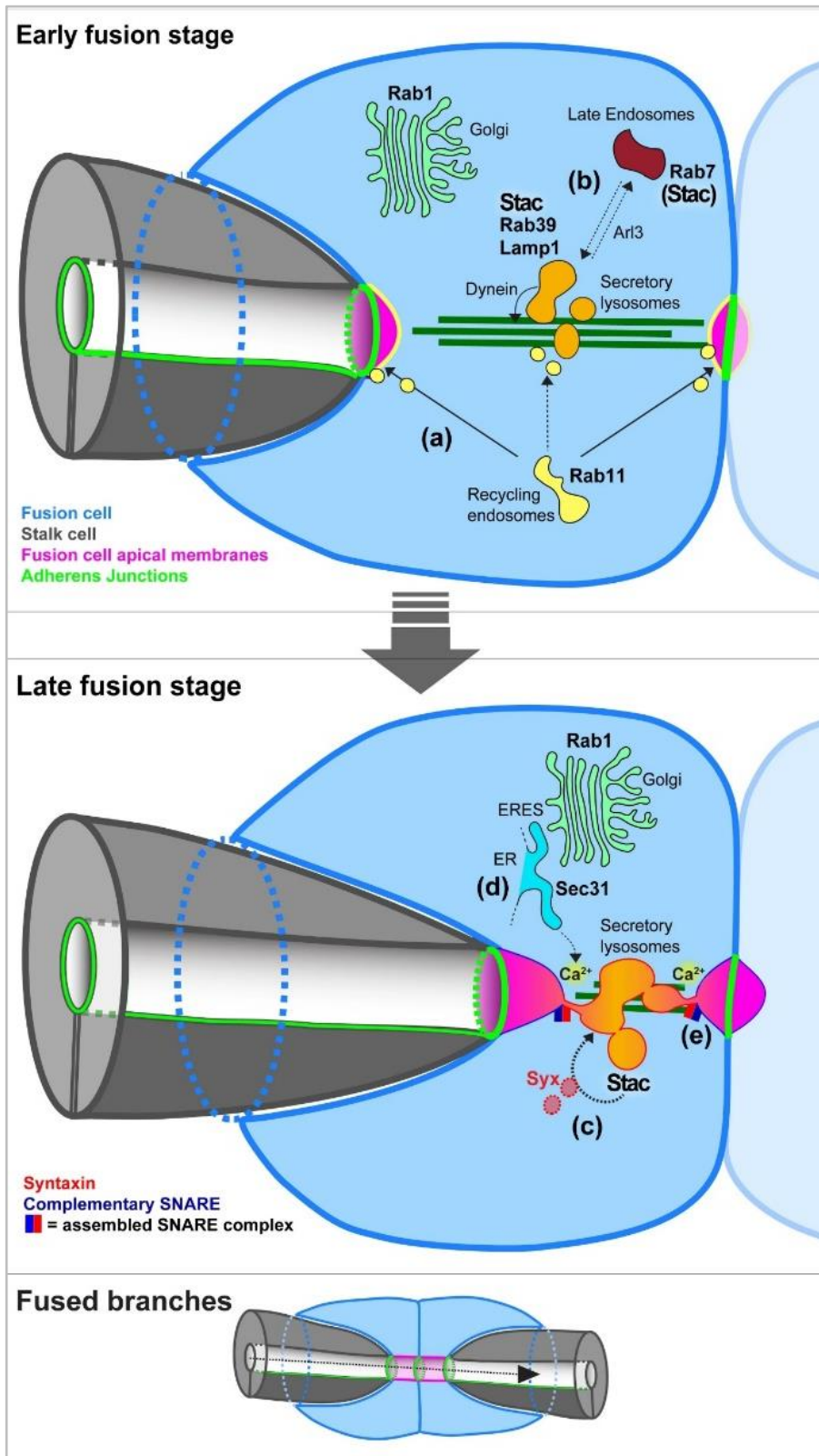


**Figure 5 Model of membrane trafficking in fusion cells.**

Schematic view of early (top) and late (bottom) stages of lumen fusion. Extension of the stalk cell lumen (left) into the fusion cell (right) is brought about by recycling endosomes (yellow), while, in a second step, fusion of the extending stalk cell lumen with the central lumen is mediated by Stac-positive secretory lysosomes (orange). Top: Early during fusion, Rab11-positive recycling endosomes (a, yellow) contribute to expansion of the two apical domains (magenta), which are possibly being pulled towards each other by the cytoskeletal track (dark green). Arl3-mediated maturation of late endosomes (b, dark red) gives rise to secretory lysosome-like vesicles (orange), which are marked by Rab39, Lamp1 and Stac, and are brought into vicinity of the apical membrane domains through Dynein-mediated anchoring to microtubules. Bottom: Late during fusion, Stac recruits Syntaxin (red) to secretory lysosomes (c), which may engage with other SNARE proteins (blue) on opposite membranes. The local release of Ca<sup>2+</sup> (d) from ER close to the site of lumen fusion may trigger the formation of mature SNARE complexes between the juxtaposed Stac vesicle and apical plasma membrane to promote fusion (e). The stage after completion of fusion, where the intracellular FC lumen has expanded, is depicted as a small cartoon at the bottom. Figure from Caviglia, Brankatschk et al. (2016)

## 2.7 The multiple roles of Rab7

### 2.7.1 Rab-proteins

Rab-proteins are the key regulators of intracellular vesicular trafficking. The roughly 60 different Rab-proteins in vertebrates associate to specific membranes and mediate their motility, targeting and fusion. Their stereotypic localization orchestrates and identifies all trafficking pathways within the cell. Rab-proteins cycle through repeated rounds of activation and inactivation and acquire their various functions by binding of effectors that recruit complexes or bind motor proteins to mediate their function. Rab proteins, therefore, coordinate many essential functions such as immunity, hormone secretion, neurotransmission and degradation (reviewed in *Stenmark 2009*).

### 2.7.2 The Rab cycle

After their initial post-translational modification on the C-terminal CXCX motif, the lifecycle of all Rab proteins is defined by several rounds of activation and deactivation. The GTP-bound state is considered the active state (*Stenmark, Parton et al. 1994*), in which Rabs can bind their effector proteins, which mediate functionality and targeting of the corresponding vesicles (*Zerial and McBride 2001*). Exchange of the GDP molecule bound to Rab proteins is brought about by the so-called guanine exchange factors (GEFs), while GTP to GDP hydrolysis is facilitated by the guanine activating proteins (GAPs). In their inactive state, Rab proteins bind the GDP dissociation inhibitor (GDI) and the Rab escort protein (REP). GDI has a hydrophilic pocket, which allows the geranylgeranylated C-terminal cysteines to be incorporated and thereby allowing the Rab proteins to remain in the cytoplasm. While most GEFs, GAPs and effector proteins are rather specific for individual Rab proteins, the GDI is shared between all Rab-GTPases.

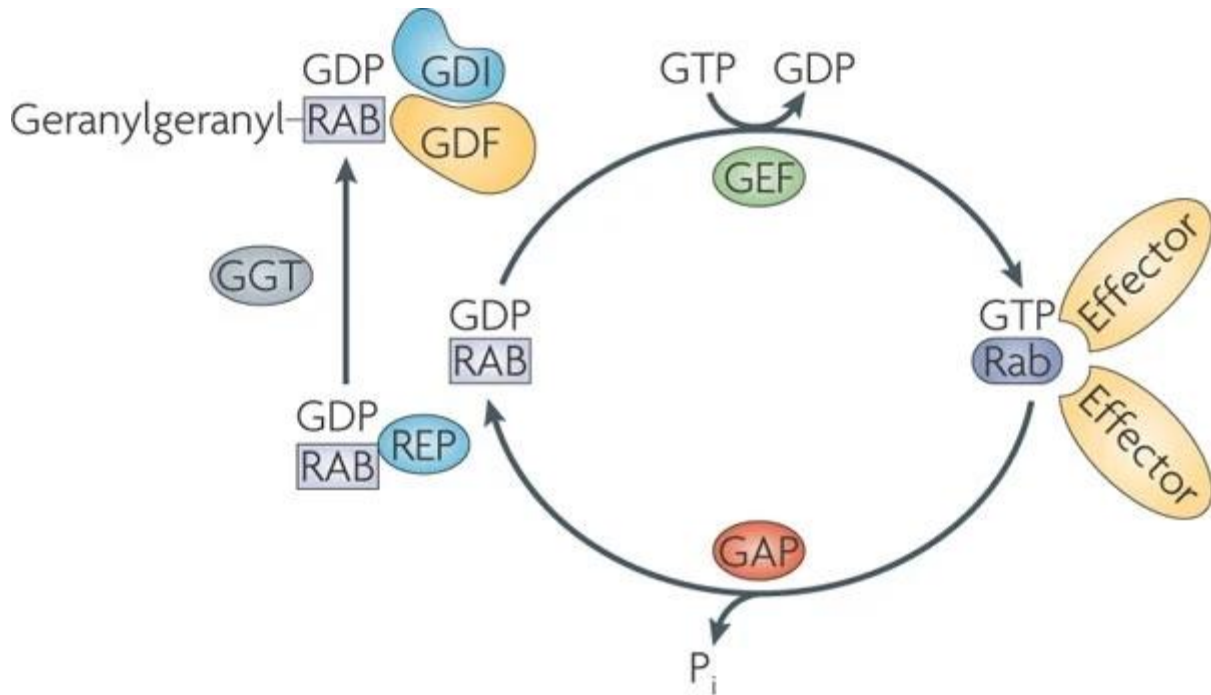


**Figure 6 The Rab cycle**

Conversion of the GDP-bound Rab into the GTP-bound form occurs through the exchange of GDP for GTP, which is catalysed by a guanine nucleotide exchange factor (GEF) and causes a conformational change. The GTP-bound 'active' conformation is recognized by multiple effector proteins and is converted back to the GDP-bound 'inactive' form through hydrolysis of GTP, which is stimulated by a GTPase-activating protein (GAP) and releases an inorganic phosphate (P<sub>i</sub>). The newly synthesized Rab, in the GDP-bound form, is recognized by a Rab escort protein (REP). The REP presents the Rab to a geranylgeranyl transferase (GGT), which geranylgeranylates the Rab on one or two carboxy-terminal Cys residues. The geranylgeranylated, GDP-bound Rab is recognized by Rab GDP dissociation inhibitor (GDI), which regulates the membrane cycle of the Rab. Targeting of the Rab–GDI complex to specific membranes is mediated by interaction with a membrane-bound GDI displacement factor (GDF). Figure from Stenmark (2009)

### 2.7.3 Structure and important domains of Rab7

Rab7 is a 207 amino acid long protein adopting the typical Rab-GTPase folding, consisting of 7 beta sheets and 6 alpha helices. The two most important domains in the protein are the two so-called switch regions, which undergo the most prominent conformational change when Rab7 is bound to GTP compared to its inactive, GDP bound, form (Wu, Wang *et al.* 2005). Switch regions are highly conserved across all small GTP-ases, but what defines the Rab proteins, and their effector specificity are the five Rab family (F) domains and the four Rab subfamily (SF) domains (Fig 7A yellow and blue boxes). Three of the F domains which lie within the switch domain, are specific for Rab proteins and, together with the four SF domains, are proposed to be the effector-interacting regions of Rabs. Another crucial sequence of amino acids is located at the C-terminal end of Rab7. This is the hypervariable domain (HVD), which consist of the last 25 amino acids before the CXCX domain and mediates insertion into the membrane after geranylgeranylation. The HVD has been shown to determine membrane specificity of Rab proteins and chimeras; the replacement of the HVD with a HVD of a different Rab leads to relocalization to membranes typical for the Rab from which the HDV stems originates (Stenmark, Parton *et al.* 1994). However, recent evidence suggests that this interaction is

not as stringent as previously believed and that localization is not solely dependent on the HVD (Ali 2004, Li, Yi et al. 2014). One more important motif lies at the N-terminus of the Rab proteins within the first 25 amino acids, which has been shown to be crucial for geranylgeranylation of the CXCX-motif at the C-terminus. A shared YXYLFK (SF1) motif just before the phosphate binding loop, a shared motif in all GTPase binding proteins, leads, when missing, to almost the same levels of absence of geranylgeranylation as when the CXCX motif itself is absent (Sanford, Pan et al. 1995). All these motifs, apart from the HVD, are almost completely (96-98%) identical in all 3 paralogues of *rab7* in zebrafish and are also conserved across species from *D.melanogster* to mouse and human *rab7*. Despite the observation that alternative splicing does occur in *rab* transcripts (Echard, Opdam et al. 2000, Dou, Ji et al. 2005), all transcripts reported for *rab7* in zebrafish contain all the 5 coding exons.

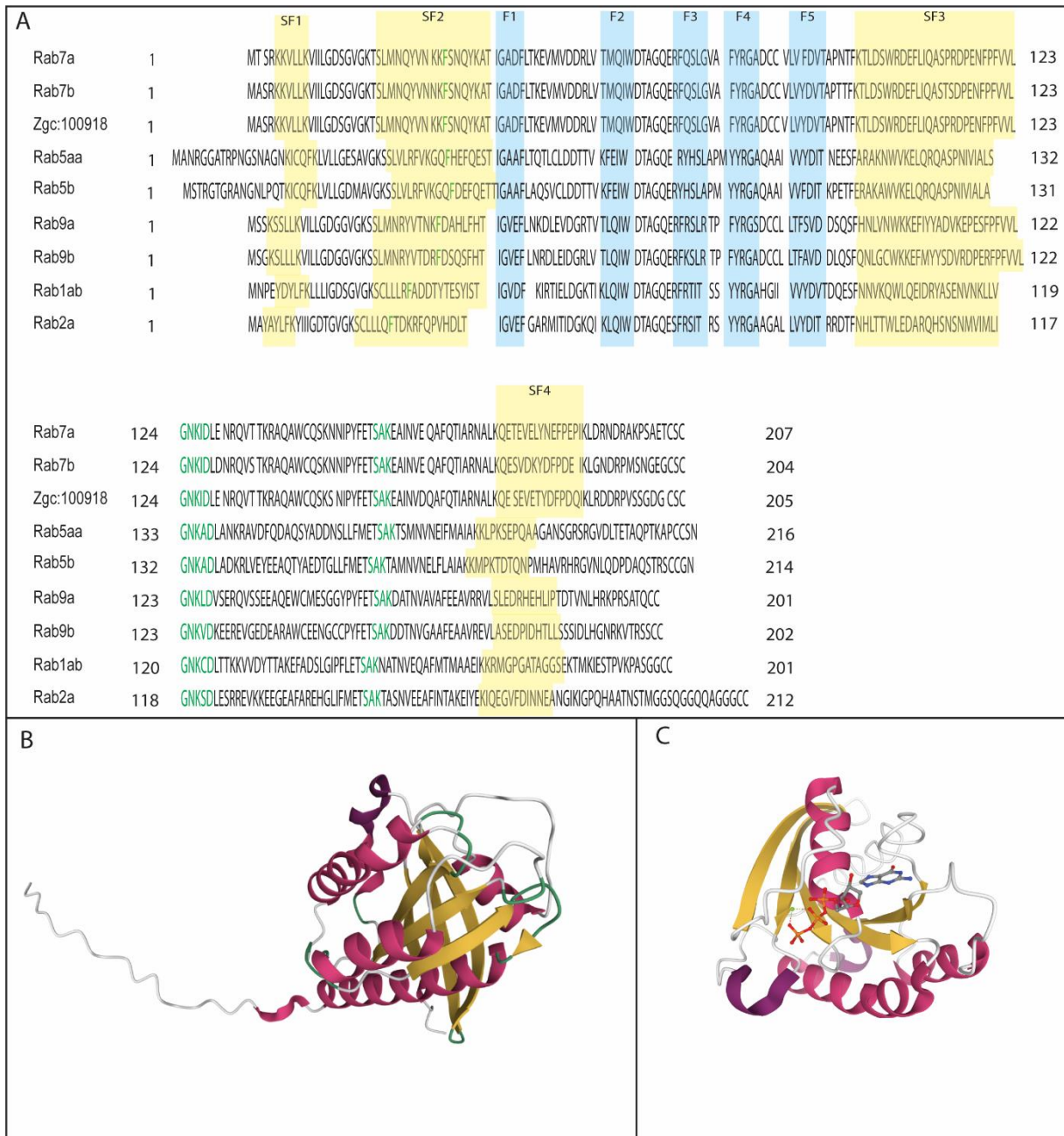


**Figure 7** Sequence and structure characteristics of Rab-protein family members

**A** Alignment of amino acid sequences of different *D. rerio* Rab-proteins. Rab family domains (F) highlighted in blue and Rab subfamily domains highlighted in yellow. Green letters indicate residues responsible for GTP binding of the Rab-proteins (3 regions with one being a single Phenylalanine in SF2). Numbers label first and last amino acid of each line. **B** Predicted structure of *D. rerio* Rab7a. Alpha-helices are colored in magenta, beta-sheets are colored yellow. In white are sequences without secondary structure. Long unfolded sequence pointing to the left is the HVD at the C-terminus. **C** Crystallography structure of *H. sapiens* Rab7a bound to GTP from (Wu, Wang et al. 2005). Alpha-helices are colored in magenta, beta-sheets are colored yellow. In white are sequences without secondary structure. Ball and Stick representation of GTP in the center of Rab7.

#### 2.7.4 The effectors of Rab7 and their function

Once Rab proteins are being activated by binding to GTP, the conformational changes occurring in the SwitchI and SwitchII regions allows them to bind their effectors. Effectors are often specific for a single Rab protein and mediate a variety of functions. Rab7 is primarily involved in identifying membrane organelles as late endosomes and lysosomes. Rab7 is recruited to early endosomes and its presence with its effectors indicates the transition to late endosomes. GTP-bound Rab7 recruits the tethering and fusion complex HOPS, which is crucial for recognition and fusion of targeted membrane compartments (Brocker, Kuhlee et al. 2012) (Fig 8 “Endosoma/lysosome fusion”). Furthermore, Rab7 mediates vesicle motility by anchoring LE/lysosomes to the microtubule network via the effector Rab Interacting Lysosomal Protein (RILP) and oxysterol-binding protein-related protein 1 L (ORP1L), which bind Dynein, or the FYVE and coiled-coil domain containing protein (FYCO) 1, which bind Kinesin (Fig 8 “Endosome motility”). Through these interactions, Rab7 controls plus- and minus-end motility of LE/lysosomes (Pankiv, Alemu et al. 2010, Van Der Kant, Fish et al. 2013). Additionally, it has also been shown that there is a link between Rab7 and the actin cytoskeleton regulator Rac1 via a Rab7 GAP called ARMUS (Carroll, Mohd-Naim et al. 2013). It has been shown that Rab7 colocalizes with actin in membrane protrusions and that Rab7 overactivation promotes their formation (Mascia, Gentile et al. 2016). Finally, Rab7 controls acidification of late endosomes and lysosomes via RILP and HOPS. Their binding to the hydrogen pumping v-ATPase regulates the drop of pH in the endosomal cascade vital for lysosomal hydrolases and, therefore, lysosomal degradation (De Luca and Bucci 2014, De Luca, Cogli et al. 2014). Apart from its role of delivering cargo towards the lysosome in many pathways (endocytosis, autophagy, lipophagy and phagocytosis), Rab7 also seems to play a role in retrograde transfer of receptors back to the trans-golgi network (TGN). The cyclic Mannose-6-phosphate receptor (ci-M6PR), for example, is routing hydrolases synthesized in the TGN to late endosomes. The retrograde of these receptors back to the TGN is dependent on Rab7 (Rojas, Van Vlijmen et al. 2008).

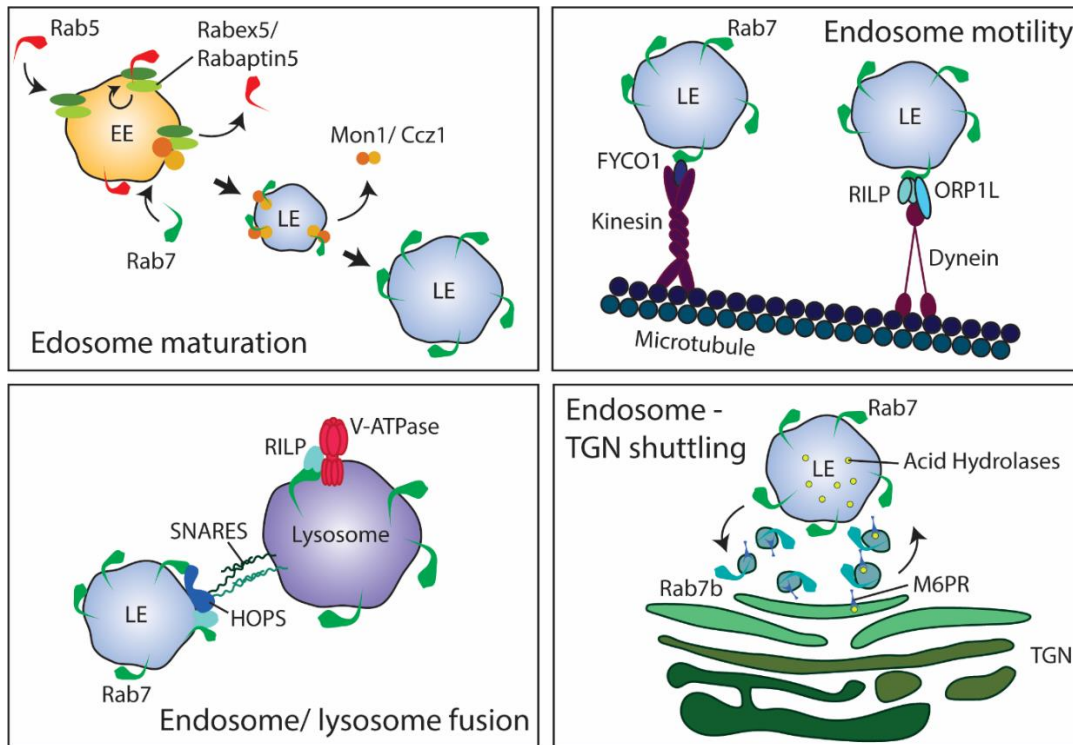


**Figure 8 Rab7 in the late endocytic pathway and in retromer regulation**

**Endosome maturation:** sequential and dynamic cooperation between Rab5 and Rab7 to determine the Rab5 to Rab7 switch; Release of Rab5 positive feedback loop by Mon1-Ccz1 complex that then recruits Rab7 to EE transitioning them into LE. **Endosome/Lysosome fusion:** RILP interaction with HOPS complex for late endosome-lysosome fusion and Rab7–RILP interaction to regulate assembly and function of the V-ATPase for acidification. **Endosome motility:** Movement of late endosomes on microtubules is determined by interaction of Rab7 with RILP and Dynein for minus-end motility while interaction with FYCO1 and kinesin mediates motility in plus-end direction. **Endosome-TGN shuttling:** Transport of synthesized Hydrolases and other cargo from and to the TGN has been shown to be mediated by Rab7. Recently it was suggested that this is a distinct function mediated via the vertebrate paralogue Rab7b. Figure adapted from Guerra and Bucci (2016)

### 2.7.5 Differences between *rab7a* and *rab7b* function

In recent years, evidence has accumulated suggesting that this retrograde transport to the TGN and the identification of late endosomes and their fusion with lysosomes are functions that are regulated by the two orthologues of *rab7*, *rab7a* and *rab7b*. It has become clear that Rab7b is responsible for shuttling hydrolases and LAMP proteins from the TGN to the LE, while it also orchestrates the recycling of the corresponding receptors back to the TGN (Progida, Cogli et al. 2010). It has also been shown that Rab7b regulates actin polymerization via Rho A and that Rab7b positive vesicles migrate along actin tracks via binding to Myosin-II. Rab7b also has the potential to organize actin polymerization in migrating cells and during stress fiber formation (Borg, Bakke et al. 2014). Lastly, a GAP has been identified, which is called TBC1D5 and is specific for Rab7b. When TBC1D5 is knocked down, fewer vesicles positive for ciM6P-receptor (M6PR) and sortilin are formed. Both proteins have been shown previously to cycle back from the lysosome to the TGN via Rab7b trafficking (Borg Distefano, Haugen et al. 2018).

## 2.8 Endocytosis

### 2.8.1 Vesicle formation

Endocytosis starts with the cargo-induced formation of vesicles at the plasma membrane. The best studied mechanism of vesicle formation is the Clathrin-mediated endocytic pathway but many Clathrin-independent ways of forming vesicle have also been described (the CLIC/GEEC endocytic pathways, Arf6-dependent endocytosis, Flotillin-dependent endocytosis, macropinocytosis, circular dorsal ruffles, phagocytosis, and trans-endocytosis (reviewed in *Doherty and McMahon 2009*)). In Clathrin mediated endocytosis, the first step involves the nucleators of the Clathrin machinery to assemble and form a pit in the otherwise flat membrane (*Henne, Boucrot et al. 2010*). These initiation sites are believed to be determined by assembly of cargo that needs to be endocytosed and/or physical properties of the membrane in these specific areas. One of these factors, the lipid phosphatidylinositol-(4,5)-bisphosphate (PIP<sub>2</sub>), appears to not only allow cargo to assemble in its proximity, but also to interact with the Clathrin nucleation factors (*Antonescu, Aguet et al. 2011*). Once the vesicle is formed, the final step consists of its scission from the membrane, which is aided mainly by Dynamin and the BAR-proteins (*Takei, Slepnev et al. 1999, Antonny, Burd et al. 2016*). Both proteins oligomerize in a ring-shaped manner with a small inner diameter (e.g. 10nm for dynamin), forcing the membrane into the formation of a very tight neck. Dynamin then uses the energy from GTP hydrolysis to bring about membrane fission.

### 2.8.2 Uncoating and the early endosome

Once vesicles have formed, but before their sorting can take place, they have to shed the Clathrin coat. Uncoating is mainly regulated by the protein HSC70, which can bind Clathrin and Auxilin and leads to disassociation of this complex when activated by ATP (*Barouch, Prasad et al. 1994*). Another important factor is the dephosphorylation of PIP<sub>2</sub>. A recently identified phosphatase is OCRL, which is recruited by Rab35 to newly formed endosomes. Rab35 is also thought to be the earliest endomembrane-identifying protein on the uncoated vesicle (*Cauvin, Rosendale et al. 2016*). The membrane of early endosomes (EE) is enriched in phosphatidylinositol 3-phosphate (PI<sub>3</sub>P) and proteins found within the membrane of EE such as Fab1, Vac1 and EEA1 all contain a so called FYVE domain which allows them to interact with PI<sub>3</sub>P (*Corvera, D'Arrigo et al. 1999*). Among the many Rab GTPases found on the EE, Rab5 is by far the most prominent, while other Rab proteins associated with EE play a role in recycling from the EE (*Pfeffer 2017*).

### 2.8.3 The Recycling back to the plasma membrane

Despite a fast-recycling pathway through which receptors are being rapidly recycled to the plasma membrane and which is mediated by Rab4, Rab35 and Syntaxins, many cargoes remain longer in the endocytic pathway and are recycled via recycling endosomes. Recycling endosomes are characterized



by the presence of Rab8 and Rab11 family proteins, Arf6 and EHD1 (*Naslavsky and Caplan 2005, Naslavsky and Caplan 2011*). Eps15 homology domain-containing (EHD) proteins in particular have been identified to play an important role in recycling. For example, depletion of EHD3 in HeLa cells has shown an increase of EE in the cell periphery and a failure in the TfR receptor reaching the endocytic recycling compartment (ERC); TfR is measurably recycled faster, presumably via fast-recycling routes. Additionally, many effectors of Rabs that are involved in recycling have a direct link to EHD proteins. The Rab4 and Rab5 shared effector Rabenosyn 5 binds EHD1 and EHD3 (*Naslavsky, Boehm et al. 2004*), and also the Rab11 effector Rab11FIP2 has binding sites for EDH1 and EDH3 (*Naslavsky, Rahajeng et al. 2006*). These evidences hint towards an import role of EDH proteins in the targeted recycling of receptors via the ERC.

#### 2.8.4 The Late endosome and Lysosome

Cargo that is not being recycled upon endocytosis continues to a route that is mostly used for degradation: the late endosomal/lysosomal pathway. Due to their molecular similarities, late endosomes are much closer to lysosomes than they are to early endosomes (*Scott, Vacca et al. 2014*). Both vesicles are characterized by the presence of LAMP1, LAMP2 and Rab7. They are distinguishable only by their physical properties when observed under the electron microscope. Lysosomes can be distinguished from late endosomes because of their very high electron density and spherical shape. Additionally, late endosomes and lysosomes are separable by subcellular fractionation gradients; using these methods, the formerly known light lysosomes, which were described to transport lysosomal enzymes to the lysosomes, turned out to be late endosomes (*De Duve 2005*). Both compartments, however, are thought to originate from early endosomes. Their conversion to the late endosomal/lysosomal pathway is accompanied by a replacement of several factors. The most prominent is the Rab5 to Rab7 conversion. Rab5 molecules present on EE establish a positive feedback loop via the Rab5 effector Rabaptin-5 and the Rab5 GEF Rabex-5 (*Horiuchi, Lippé et al. 1997*). This loop strengthens continuous binding of Rab5 to EE. Interruption of this feedback loop has been shown to be mediated via the Mon1 (Sand1 in *C.elegans*)-CCZ1 complex, which is recruited from the cytoplasm. This complex acts simultaneously as an effector of Rab5 and a GEF for Rab7, by recruiting Rab7 to maturing EE compartments and turning them into LE (*Poteryaev, Datta et al. 2010*). The Rab5 to Rab7 switch is also accompanied by changes that ensure that docking and fusion of LE can only take place at desired membranes. The CORVET complex found on EE is replaced with the HOPS complex and also the set of SNAREs binding to EE and LE differ (*Solinger and Spang 2013*). The final step in the endosomal pathway is the fusion of LE or autophagosomes with lysosomes. Late endosome and lysosome fusion is mediated by the small GTPase Arl8 and its effector HOPS, which orchestrate the assembly of the trans-SNARE complex. Arl8 and Rab7 additionally interact with the tethering protein PLEKHM1 to promote late endosome-lysosome fusion (*Marwaha, Arya et al. 2017*).

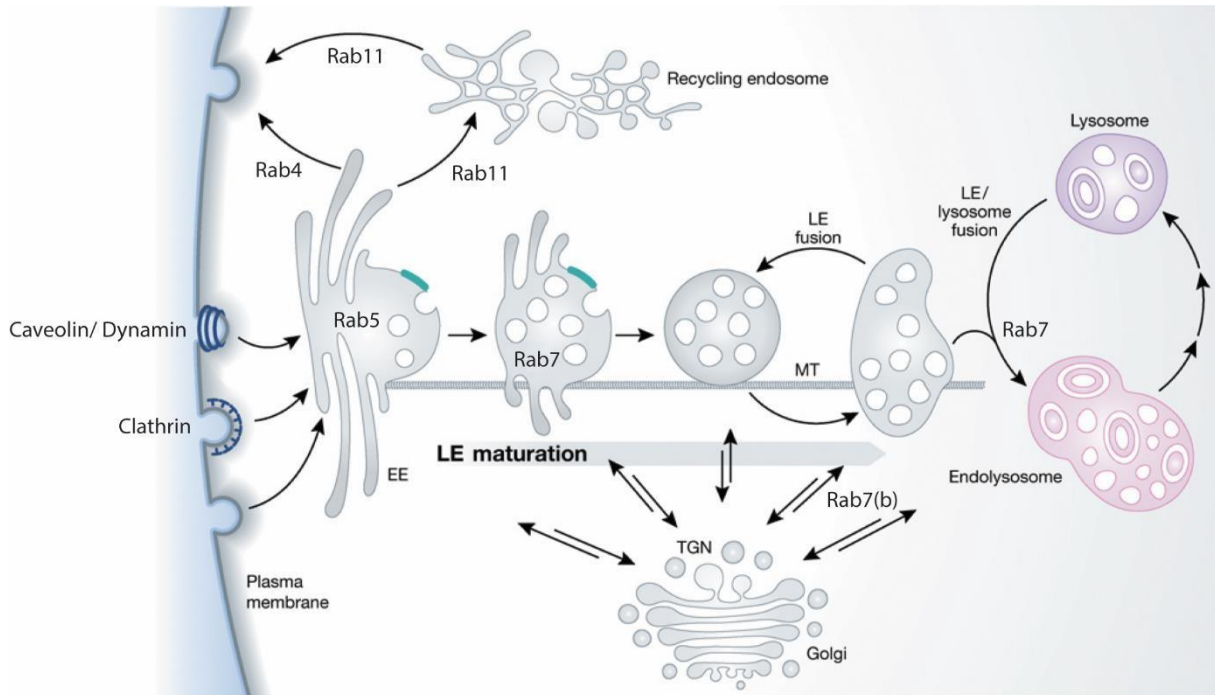


**Figure 9 The endosome/lysosome system.**

The primary endocytic vesicles deliver their contents and their membrane to the Rab5 labeled EEs in the peripheral cytoplasm. The EEs accumulate cargo and support recycling to the plasma membrane (directly orchestrated by Rab4 or via Rab11 dependent recycling endosomes), conversion of the EEs to LE takes place. Thus, as the endosomes are moving towards the perinuclear space along microtubules (MT), the nascent LE are formed (Rab5 to Rab7 switch) inheriting the vacuolar domains of the EE network. They carry a selected subset of endocytosed cargo from the EE, which they combine en route with newly synthesized lysosomal hydrolases and membrane components from the TGN, possibly organised by Rab7b. They undergo homotypic fusion reactions, grow in size, and acquire more ILVs. Their role as feeder system is to deliver this mixture of endocytic and secretory components to lysosomes. To be able to do it, they continue to undergo a maturation process that prepares them for the encounter with lysosomes. The fusion of an endosome with a lysosome generates a transient hybrid organelle, the endolysosome, and later lysosomes in which active degradation takes place. Figure adapted from Huotari and Helenius (2011)

The most prominent proteins that are found within the membrane of LE and lysosomes are the LAMP1 and LAMP2 proteins, which make up nearly 80% of all lysosomal proteins (Saftig and Klumperman 2009). These proteins are heavily glycosylated on their luminal side and form the glycocalyx, a barrier protecting against autodigestion (Kornfeld and Mellman 1989). Furthermore, vATPase hydrogen channels are present in the membrane of late endosomes and lysosomes. These channels interact, among others, with the HOPS complex and are responsible for the drop of pH in endosomal maturation, going down from a pH of 6 in EE (Murphy, Powers et al. 1984) to a pH of 4.5- 5 in LE and lysosomes (Griffiths, Back et al. 1989). Finally, the lysosome has recently also been described to function as a regulatory and signalling hub sensing nutrient availability and signaling to the mTOR pathway via its recruitment to the lysosomal membrane. Lysosomes can do so by the help of amino-acid-dependent activation of RAG GTPases and their interaction with regulator (Lawrence and Zoncu 2019) or the cholesterol-binding Niemann–Pick type C1 protein (NPC1) (Castellano, Thelen et al. 2017).

### 2.8.5 Lysosome related organelles

As mentioned before, the lysosomal pathway is not exclusively used for degradation. In the last couple of years, several organelles have been studied that carry all the characteristic markers for lysosomes, but seem to have entirely different functions. These lysosome related organelles (LRO) were first described as specific compartments in specialized cell types. Among the LROs are melanosomes, Weibel-Palade bodies (WPBs), as well as platelet  $\alpha$ -granules and cytotoxic T lymphocytes (CTLs). Recent studies analysing plasma membrane wound repair showed that not only highly specialized, secretory cell types exhibit exocytosis of lysosomes; upon membrane damage,  $\text{Ca}^{2+}$  influx induces exocytosis of lysosomes and lysosome-mediated resealing of the plasma membrane (reviewed in (Andrews, Almeida et al. 2014)). The best studied LROs in endothelial cells are WPBs, which were shown to be storage granules for the von Willebrand Factor and P-selectin in its membrane (Weibel and Palade 1964, Wagner and Frenette 2008). Upon vessel injury or inflammation, Histamine and Thrombin release lead to an increase of intracellular  $\text{Ca}^{2+}$  and induces controlled fusion of WPBs with the plasma membrane (reviewed in (Nightingale and Cutler 2013)). Generally, it is thought that fusion of WPBs leads to a rapid change of the surface of endothelial cells, turning its anti-adhesive cell membrane to an adhesive surface, allowing platelets and leukocytes to adhere (Chehab, Santos et al. 2017). Maturing WPBs have already been shown to be labelled by Rab27 and Rab3 (Nightingale and Cutler 2013). Rab27a has also been reported to label other lysosome-related organelles such as melanosomes and lytic granules (Marks, Heijnen et al. 2013, Chehab, Santos et al. 2017).

### 2.8.6 Lysosome related organelles in the zebrafish vasculature

As mentioned above, LRO have been described in the tracheal system of *D. melanogaster* to play a crucial role in the luminal membrane fusion in fusion cells. Since there are many similarities between tracheal and vascular anastomosis, Vahap Aydogan and Etienne Schmelzer, have investigated the role of vesicle trafficking in the lumenization of the zebrafish vasculature. While Vahap Aydogan has found that vesicles labeled with the membrane marker mcherry-CAAX, linger around and seem to fuse with the growing luminal membrane, extensive yet unpublished work from Etienne Schmelzer identified these compartments as part of the late endocytic/lysosomal pathway. He showed that these vesicles colocalize with the LE and lysosomal markers Rab7a, LAMP2, Rab9 and Rab39bb. These colocalization studies, together with high resolution *in vivo* live imaging analyses, showed that these Lamp2-RFP positive vesicles indeed integrate into the growing membrane. This hints towards a similar pathway in lumenization of the zebrafish vasculature as has been described in the tracheal system of *D. melanogaster*.

### 3 Aims of the thesis

Anastomosis in the zebrafish vasculature shows many similarities to anastomosis in the tracheal system of *Drosophila melanogaster*. This stereotypical process has been shown to rely on organelles and key organizers of the endosomal trafficking pathway. Previous studies in our lab indicate that these organizers could play a similar role in the zebrafish vasculature. This notion is based on the observation that membranous compartments, which are part of the late endocytic/ lysosomal pathway by their colocalization with Rab7, Rab9, Rab39 and Lamp2, disperse along the apical luminal membrane. In this study I generate zebrafish knockout mutants for all *rab7* orthologues, that orchestrate the maturation of early endosomes into late endosomes and lysosomes, and *unc13d*, the zebrafish homologue of the *Drosophila melanogaster* gene *staccato*, a key regulator of lumen fusion in tracheal anastomosis. Using vascular and endosomal trafficking markers such as: *Tg(kdrl:mcherryCAAX)*, *Tg(kdrl:EGFP-CAAX)*, *TgBAC(lamp2:LAMP2-RFP)*, *Tg(fli:EGFP-Rab9b)* and *Tg(fli:PECAM-GFP)* will allow me to study the role of *rab7* and *unc13d* dependant endosomal trafficking in lumen formation and fusion in the zebrafish vasculature. In order to analyse the developing zebrafish vasculature, I will use high resolution confocal imaging paired with high temporal resolution spinning disk acquisition to better understand to which extent vascular lumen formation follows the same principles as tracheal lumen formation and whether this process is reliant on endosomal trafficking pathways.

# 4 Results: Chapter I

## 4.1 Genetic analysis of rab7 mutants in zebrafish

Daniel Heutschi, Etienne Schmelzer, Vahap Aydogan, Alexander Schmidt, Heinz-Georg Belting, Anne Spang, Markus Affolter, Maria Kotini

#### 4.1.1 Abstract

Vascular network formation requires the fusion of newly built blood vessels and the emergence of a patent lumen between the newly established connections so that blood flow can start. Lumen formation has been shown to depend on the late endosomal/lysosomal pathway in various organs of animal systems. Here, we identified a late endosomal/lysosomal vesicular fraction (Rab7/Lamp2) in early zebrafish angiogenic sprouts, which appears to contribute to apical membrane growth during lumen formation. To study the effect of the late endocytic pathway on vascular development, we generated mutant alleles for all three *rab7* genes in zebrafish (*rab7a*, *rab7ba*, *rab7bb*). All *rab7* genes are expressed in wild-type zebrafish and we did not detect any compensatory effects by the other *rab7* isoforms in single knockout mutants, which were all viable. Only the triple mutant was lethal suggesting some functional redundancy. However, the different *rab7* isoforms fulfil also at least partially independent functions because eggs laid from mothers lacking two *rab7* contained enlarged yolk granules, suggesting maternal contribution of these two *rab7*. Finally, we observed minor effects on lumen formation in embryos which still express one copy of *rab7*. Our results support the notion that the late endocytic/lysosomal compartment contributes to lumen expansion.

#### 4.1.2 Introduction

The vasculature is the first organ to form in the vertebrate embryo. Its function is to supply the surrounding tissue with nutrients and oxygen and it is vital for the growth of the embryo. An essential step in the establishment of a functional vascular network is the formation and expansion of the lumen. The onset of vascular lumen formation begins with the apical polarization of endothelial cells (ECs) upon contact of two vessel segments (anastomosis) and the expansion of the initial apical patch in a ring-like structure. In the final step, the lumens of the two contacting vascular branches must be connected to allow for blood flow. Lumen expansion has been described to occur via two distinct processes, transcellular lumen formation and cell rearrangements, a process also referred to as cord hollowing (*Ellertsdóttir et al., 2010; Herwig et al., 2011*).

During cord hollowing, the lumen is formed between ECs, while during transcellular lumen formation, the lumen is formed within ECs and is driven by blood pressure. The transcellular lumen forms via membrane invagination through the cell body and subsequent fusion of the invaginating membrane with the newly-formed distal apical patch. The process then progresses into the next cell (*Francis et al., 2022; Gebala et al., 2016; Herwig et al., 2011; Lenard et al., 2013*). It is not clear how the apical membrane emerges at the right place or which membranous cell compartment contributes to its formation.

The Rab GTPases vesicle trafficking program, and more specifically the Rab35, has been recently shown to regulate the establishment of apicobasal polarity during angiogenesis *in vitro* and *in vivo* in

the zebrafish embryo (Francis et al., 2022). Apart from the vasculature, vesicular trafficking has been involved in the formation of lumen in other systems.

The mechanism of lumen connection in the vertebrate vasculature shares many morphological similarities with the one in the tracheal system of *D. melanogaster* (Camelo et al., 2022; Caviglia and Luschnig, 2014; Hayashi and Kondo, 2018; Kotini et al., 2019). In the embryonic trachea, the formation of a continuous lumen via apical membrane fusion has been described to be dependent on vesicular trafficking (Caviglia et al., 2016). In the absence of the tethering protein Unc-13-4/Staccato, individual branches of the tracheal system fail to connect their lumens and do not form a continuous network. In tracheal fusion cells, Unc-13-4/Staccato recruits vesicles that have been characterized by the presence of Rab7, Rab39 and Lamp1 as secretory lysosomes, which accumulate in the cytoplasm between the two growing luminal membranes of the fusion cell (Caviglia et al., 2016).

Formation of late endosomes and lysosomes is dependent on Rab7. In the endocytic pathway, Rab7 is recruited to early endosomes, converts them into late endosomes and promotes their fusion with lysosomes (Marwaha et al., 2017; Poteryaev et al., 2007, 2010; Rojas et al., 2008). Rab7 recruits the HOPS tethering complex that interacts with SNARE proteins and leads to membrane-membrane recognition and mediates fusion of late endosomes with lysosomes (Bröcker et al., 2012; Solinger and Spang, 2013). Loss of Rab7 leads to severe defects in early development. In *C. elegans*, yolk granules are enlarged upon reduction of the Rab7 by RNAi or in a knockout of its guanine exchange factor (GEF) SAND-1; loss of Rab7 causes embryonic lethality (Poteryaev et al., 2007). In mice, the absence of Rab7 yield a loss of endoderm specification due to a lack of Wnt signalling (Kawamura et al., 2012).

Since the precise role of late endocytic trafficking in vertebrate vascular lumen formation is not known, and since Rab7 is a main organizer of late endosomal trafficking, we analysed the expression of EGFP-Rab7a during lumen formation/expansion in zebrafish embryos. We find that Rab7a colocalizes with dot-like structures also marked by a CAAX membrane marker. These structures often elongate along the apical membrane, suggesting that they fuse with the latter. The dot-like structures also colocalize with Lamp2, a lysosomal-associated membrane protein. These results suggest that a late endosomal, lysosomal compartment might contribute to apical membrane growth in angiogenesis.

To analyse the role of Rab7 in vascular development, we generated mutant alleles for the three *rab7* genes in zebrafish, *rab7a*, *rab7ba* and the newly found *rab7bb*, which we analysed in this study. We showed that this third *rab7* gene, *rab7bb*, shares some redundant function with *rab7a*. We also found that loss of maternally contributed *rab7* leads to an increase in yolk granules, similar to what was observed in *C. elegans*, and that complete loss of Rab7 in triple mutants is lethal. High resolution

confocal imaging revealed that lumen formation in the analysed double mutants is not significantly impaired. In order to study the role of Rab7 in angiogenesis and lumen formation, endothelial-specific knockout or knockdown strategies will be needed.

### 4.1.3 Results

#### 4.1.3.1 Rab7 colocalises with mCherry-CAAX at dots

To visualize membrane dynamics during vascular lumen formation, we used a transgenic reporter *Tg(kdrl:HsHRAS-mCherry)<sup>s916</sup>*, which effectively labels membrane compartments in endothelial cells. Previous live-imaging studies (Lenard *et al.*, 2013; Phng *et al.*, 2015) have shown that this reporter preferentially labels the apical membrane of nascent blood vessels. We therefore reasoned that this reporter is ideally suited to detect and identify vesicular membrane structures which contribute to the nascent apical cell membrane. Time-lapse analysis revealed local accumulation of mCherry-CAAX protein in the cytoplasm as dots. (Fig 10 A-B).

In order to identify the nature of these CAAX dots and detect the origin of the apical membrane, we transiently expressed different EGFP-fusions of Rab proteins, such as Rab5c (marker for early endosomes), Rab7a (marker for late endosomes) and Rab11a (marker for recycling endosomes) in the developing vasculature. While no clear colocalization was observed with Rab5c and Rab11 (Fig 17). While mCherry-CAAX appeared as filled dots, EGFP-Rab7a was visible in doughnut-like structures around these dots (see arrows in Fig 10C). The colocalization of mCherry-CAAX and Rab7a suggests that these structures represent late endosomal-lysosomal compartments, and that such a compartment could contribute to apical membrane growth in angiogenic sprouts. Indeed, when we compared EGFP-Rab7a and mCherry-CAAX localisation during lumen expansion, we observed co-migration of Rab7/CAAX structures along the apical membrane (Figure 10 G-I), suggesting that they might integrate into the apical membrane and may be a major source for this membrane compartment.



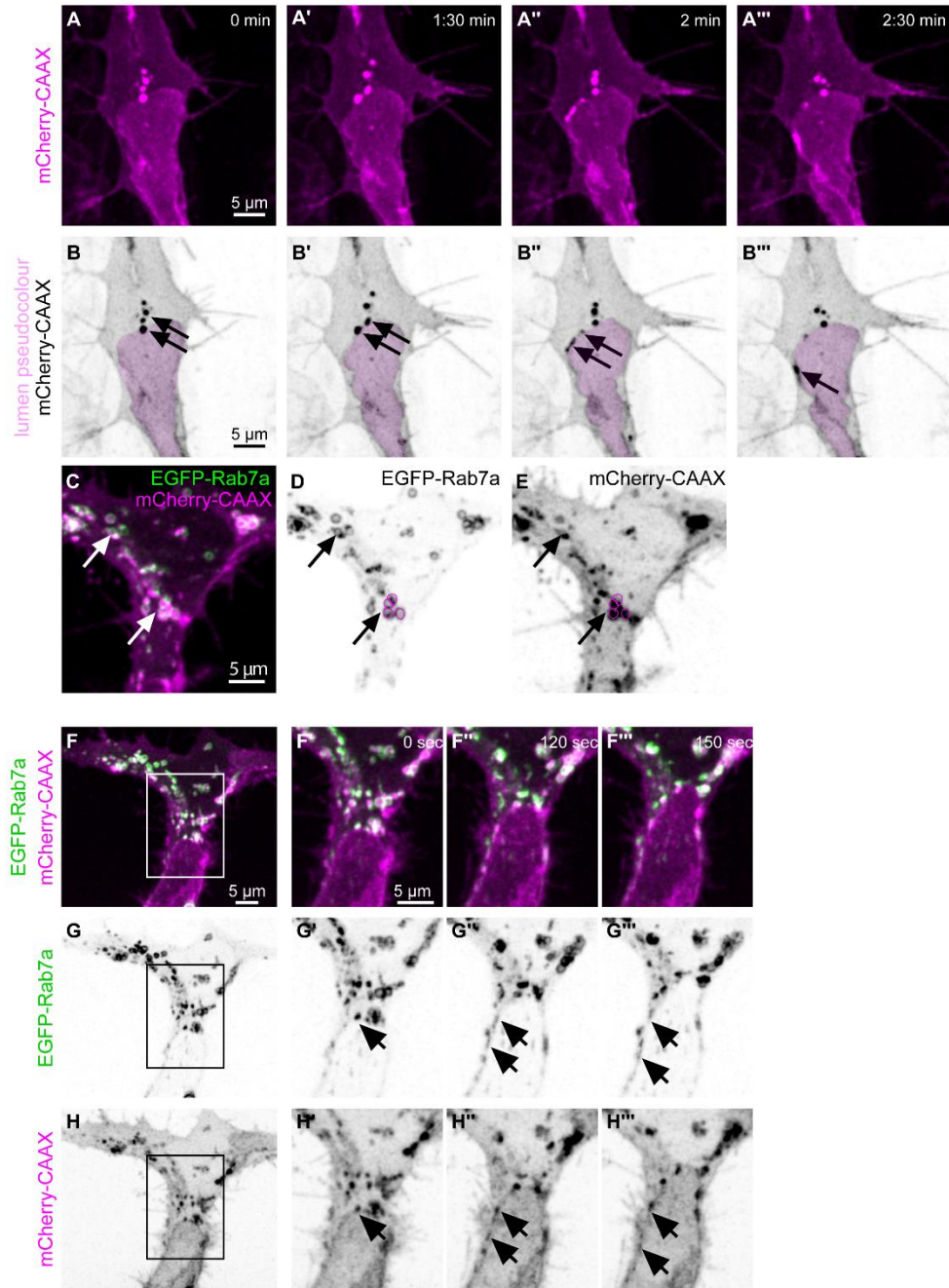


**Figure 10 Rab7 co-localization with the apical marker CAAX and elongation of CAAX/Rab7 dots at the apical membrane**

**A-B** Confocal images from a time-lapse of a tip cell from a transgenic *Tg(kdrl:mCherry-CAAX)<sup>S916</sup>* embryo shown in magenta. **B-B'''** Inverted contrast of mCherry-CAAX from **A** shows CAAX dots which elongate along the apical membrane. Pink pseudo-color indicates the vascular lumen. **C-E** Confocal images of the tip cell of a double transgenic *Tg(fli:EGFP-Rab7a)<sup>ubs48</sup>; Tg(kdrl:mCherry-CAAX)<sup>S916</sup>* embryo at 32hpf. **D** Inverted contrast image of the EGFP-Rab7 channel. **E** Inverted contrast image showing the membrane marker mCherry-CAAX in ECs. Arrows point to co-localisation of Rab7 and CAAX at dots. **F** Distribution of Pearson Correlation Coefficient (PCC) of EGFP-Rab7a ROIs in correlation to mCherry-CAAX, showing a correlation between EGFP and mCherry signal (n=8 tip cells, N>3 different embryos). **F** A tip cell from a transgenic *Tg(kdrl:mCherry-CAAX)<sup>S916</sup>* embryo at 30hpf, transiently expressing *fli:EGFP-Rab7a*. **F'-F'''** Stills from the ROI from **D** showing EGFP-Rab7 and mCherry-CAAX dots that move along the expanding apical membrane. **G-G'''** EGFP-Rab7a signal alone. **H-H'''** mCherry-CAAX signal alone. Arrows point to the EGFP-Rab7a and mCherry-CAAX dots.

## 4.1.3.2 Rab7a colocalizes with Lamp2 in endothelial cells

To further confirm the nature of the mCherry-CAAX/GFP-Rab7a labelled structures as late endosomal/lysosomal, we made use of a BAC transgenic zebrafish line expressing a Lamp2-RFP fusion protein (Rodríguez-Fraticelli *et al.*, 2015). Lamp2 is a component of late endosomal/lysosomal compartments and is expressed in many different tissues in early zebrafish embryos, including the vasculature (see Fig 11 A and C). Transient expression of EGFP-Rab7a in the vasculature of an embryo expressing Lamp2-RFP showed indeed that Lamp2-RFP formed dot-like and doughnut-like structures in ECs, and that these structures were co-localized with EGFP-Rab7a (Fig 11 A-C and higher magnification in Fig 11 A'-C', respectively). Strikingly, we observed that Lamp2-RFP positive structures elongated along the apical membrane, similar to what we have seen previously for mCherry-CAAX dots (Fig 11 D-F; see also Fig 10 A-B). We therefore conclude that mCherry-CAAX positive structures represent late endosomal/lysosomal compartments, and that these compartments might contribute to the growing apical membrane during transcellular lumen formation.

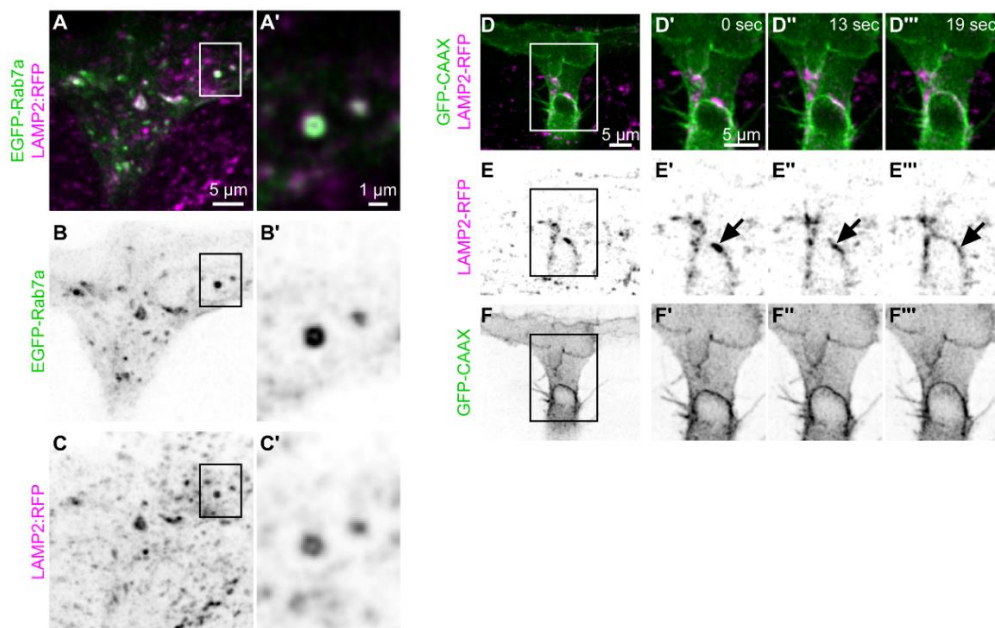


**Figure 11 EGFP-Rab7a and Lamp2-RFP colocalize at dots**

**A-B** Confocal images of a tip cell from a transgenic *TgBAC(Lamp2-RFP)<sup>pd1117</sup>* embryo at 30hpf, transiently expressing *fli:GFP-Rab7a*. **A** Z-projection of the tip cell. **A'** Single z-slice of the ROI in **A**. Two vesicles are depicted with signal positive for GFP-Rab7a and Lamp2-RFP. The largest vesicle shows a reduced signal in the centre for both GFP-Rab7a and Lamp2-RFP, resembling late endosomal/lysosomal structures. **B-B'** EGFP-Rab7a signal alone in endothelial cells. **C-C'** Lamp2-RFP signal alone. **D** Schematic representation of the blood vessel (tip EC) undergoing transcellular lumen formation. Rab7, Lamp2 and CAAX co-localise at dots which migrate along the expanding apical membrane. **D** Tip cell of a double transgenic *Tg(kdrl:GFP-CAAX)<sup>s916</sup>; TgBAC(Lamp2-RFP)<sup>pd1117</sup>* embryo at 34hpf. **D'-D'''** Timelapse from the ROI in **E** showing Lamp2-RFP dot-like structure elongating along the apical, invaginating membrane. **E-E'''** Lamp2 signal alone. **F-F'''** mCherry-CAAX signal alone. Arrows point to the EGFP-Rab7 and mCherry-CAAX dot-like structures

#### 4.1.3.3 Identification and description of *rab7* genes in zebrafish

As a first step to generate mutants for the *rab7* genes in zebrafish, we analysed and characterised all *rab7* genes encoded in the zebrafish (*Danio rerio*) genome. Two genes encoding Rab7 proteins have been described in zebrafish; *rab7a* and *rab7b* (Hall *et al.*, 2017). A third gene (*zgc:100918*) has been proposed to encode a Rab7-like protein (Bayés *et al.*, 2017). The amino acid sequences encoded by these three paralogues are 88% identical, with *zgc:100918* seemingly being a “hybrid” between *rab7a* and *rab7b*, showing 91% and 92% similarity to the other two genes, respectively (Fig 18A). A phylogenetic analysis of the amino acid sequences encoded by the three *rab7* genes revealed that *zgc:100918* groups closer to zebrafish *rab7b* than to zebrafish *rab7a* (Fig 12A). This duplication seems to be common in the cyprinid family, as genes named according to the zebrafish *zgc:100918* can also be found in other members of this family. These genes (third allele) cluster together and the entire cluster groups closer to the *rab7b* cluster of other cyprinids (Fig 12B). Investigation of the region around *zgc:100918* on chromosome 10 (Chr. 10) shows that genes in that region are annotated copies of genes within the region around *rab7b* on chromosome 8 (Chr. 8). For example, *bmp1a* and *fgfr1a* are on Chr. 8 while their paralogous genes *bmp1b* and *fgfr1b* are on Chr. 10 (Fig 12C). These data show that *zgc:100918* lies within a region of Chr. 10, which is similar to a region on Chr. 8, and it therefore represents a copy of *rab7b* that should be renamed *rab7bb*. The original *rab7b* should be renamed *rab7ba*. According to two published transcriptomics databases (<https://www.ebi.ac.uk/gxa/experiments/E-ERAD-475>) (Lawson *et al.*, 2020), *rab7bb* is expressed at similar levels as *rab7a* (Fig 12D), but at much higher levels than *rab7ba*. That was observed for both endothelial and non-endothelial cells. (Fig 12D). Additionally, *rab7a* and *rab7bb* showed quite strong expression at the RNA level at the one cell stage, indicating maternal deposition of *rab7a* and *rab7bb*, but not of *rab7ba* (Fig 12E). Taken together, these data strongly suggest that the initially proposed *rab7*-like gene *zgc:100918* represents a copy of *rab7b*, and since its expression pattern is similar to *rab7a*, it has to be included in a genetic analysis of *rab7* in zebrafish.

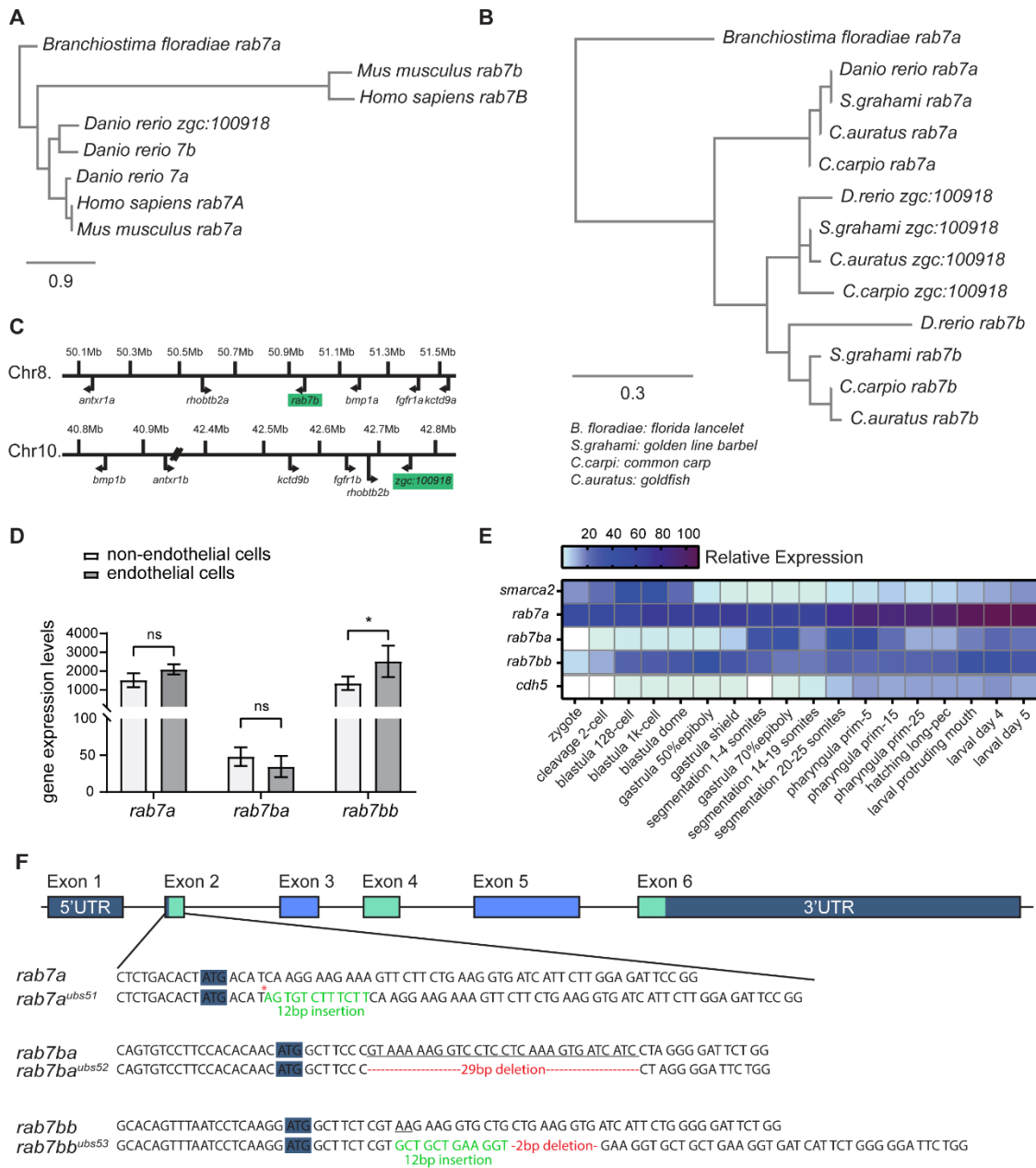


**Figure 12 Description of all rab7 isoforms in zebrafish**

A Phylogenetic tree constructed from the protein sequence derived from amphioxus (outgroup), human, mouse and zebrafish *rab7* genes, scale: 0.9 amino acid substitutions. B Phylogenetic tree constructed from the protein sequences of *rab7a*, *rab7b* and *zgc:100918* genes from zebrafish, other cyprinid family members and amphioxus (outgroup), scale: 0.3 amino acid substitutions. C Representation of the chromosomal region around the genes *rab7b* on chromosome 8 and *zgc:100918* on chromosome 10. Indicated are the genes that are already annotated copies of each other. D Analysis of the expression of *rab7* genes in endothelial and non-endothelial cells from zebrafish transcriptomics data (Lawson, Li et al. 2020). E Heatmap of expression of *rab7* genes, a maternally contributed gene (*smarca2*) and an endothelial-specific gene (*cdh5*) during zebrafish development, based on data from an EMBL expression atlas (Papatheodorou et al. 2020 see Material and Methods). F Schematic representation of the gene structure of *rab7* genes in zebrafish. 5' and 3' UTRs and ATG (start codon) are highlighted in dark blue, alternating coding exons are represented in light green and light blue. Sequence of the exons 2 of *rab7a*, *rab7ba* and *rab7bb*. Below each gene sequence appears the respective sequence of mutant alleles *ubs51*, *ubs52* and *ubs53*. Deleted base pairs are underlined at the wild-type sequence, inserted base pairs are represented in light green and deletions are shown in red in mutant alleles. Red asterisk shows premature stop codon in the sequence of exon2.

#### 4.1.3.4 Characterization of *rab7* protein levels in corresponding *rab7* mutants

To investigate the role of *rab7* in vascular lumen formation, mutant alleles for all three *rab7* loci were generated using the CRISPR/Cas9 system. gRNAs were designed for each of the three *rab7* genes within the first coding exon (exon2) and as close as possible to the start codon to minimize the potential to generate a residual functional protein. For *rab7a*, a 12 bp insertion leading to a stop codon after the second amino acid (aa) was isolated; this allele will be referred to as *rab7a<sup>ubs51</sup>* (Fig 12F; Fig 18D). For *rab7ba*, a 29 bp deletion leading to an out-of-frame protein after aa 4 and a stop codon in Exon3 was isolated; this allele will be referred to as *rab7ba<sup>ubs52</sup>* (Fig 12F; Fig 18D'). Finally, for *rab7bb*, a 12 bp insertion accompanied by a 2 bp deletion leading to an out-of-frame protein after aa 4 and a stop codon in exon 3 of the gene was isolated; this allele will be referred to as *rab7bb<sup>ubs53</sup>* (Fig 12F; Fig 18D''). Usage of unpredicted downstream alternative start codons in these mutants would lead to shortened Rab7 proteins lacking an important prenylation site (PS), which is encoded within the first 25 bp of the *rab7* genes (Fig 13A; Fig 18A); without this site, the C-terminal XCXC domain cannot be prenylated and the protein cannot be inserted into the membrane (Steele-Mortimer *et al.*, 1994).

To test whether these mutant alleles were indeed true null mutations (lacking specific Rab7 isoforms), targeted LC-MS proteomics analyses of homozygous in-crosses from each mutant allele were performed with pools of 24-hour old embryos. Since homozygous mutants of all three *rab7* mutant alleles were viable and fertile, we then analysed the respective maternal-zygotic mutants for maternal contribution from each respective allele. Different peptides were used for the MS analyses, which were either common to all three proteins (PanRab7) or two of the three isoforms (Rab7a/Rab7ba), or specific for a given protein (see Fig. 13A and Methods). Care was taken to compare different protein isolates with the same peptide(s), rather than measuring the levels of different peptides using a single protein preparation. For a detailed description of the methods and the approaches taken, see the Method section.

In wild-type embryos, we found that the most abundant Rab7 protein was Rab7a (roughly 60% of the total amount of Rab7), while Rab7bb represented 30%. The least abundant isoform was Rab7ba, which represented roughly 10% (Fig 13B). The low levels of Rab7ba did not allow us to use the specific peptides in the mutant analyses (see below).

Our MS analyses using mutant embryos showed that *rab7a<sup>ubs51</sup>* and *rab7bb<sup>ubs</sup>* most likely represented null mutants, since no residual proteins or shortened fragments thereof were detected in the corresponding mutants (Fig 13C and Fig 13D, respectively). To measure potential residual protein levels of Rab7ba in *rab7ba<sup>ubs52</sup>*, a pan Rab7a-Rab7ba reference peptide was used (Fig 13A), because the reference peptides specific for Rab7ba (Fig 13A) were only detected at very low levels in the wild-

type, but often remained under the detection threshold in the different mutants (see Method section for further details and explanations). Nonetheless, based on these analyses (Fig 18B), we conclude that *rab7ba*<sup>ubs52</sup> also represents a null allele.

The targeted LC-MS data further revealed that there is no obvious compensation; the levels of the remaining, wildtype Rab7 isoforms were not elevated in any of the *rab7* mutants we analysed; Rab7a was not elevated in *rab7ba*<sup>ubs52</sup> nor in *rab7bb*<sup>ubs53</sup>, while Rab7bb was not increased in *rab7a*<sup>ubs51</sup> and in *rab7ba*<sup>ubs52</sup> (see Fig 13B,C). Again, we came to the same conclusion with respect to Rab7ba using a more indirect quantification approach, namely that its levels are not significantly increased in the absence of either of the two other isoforms (see Method section).

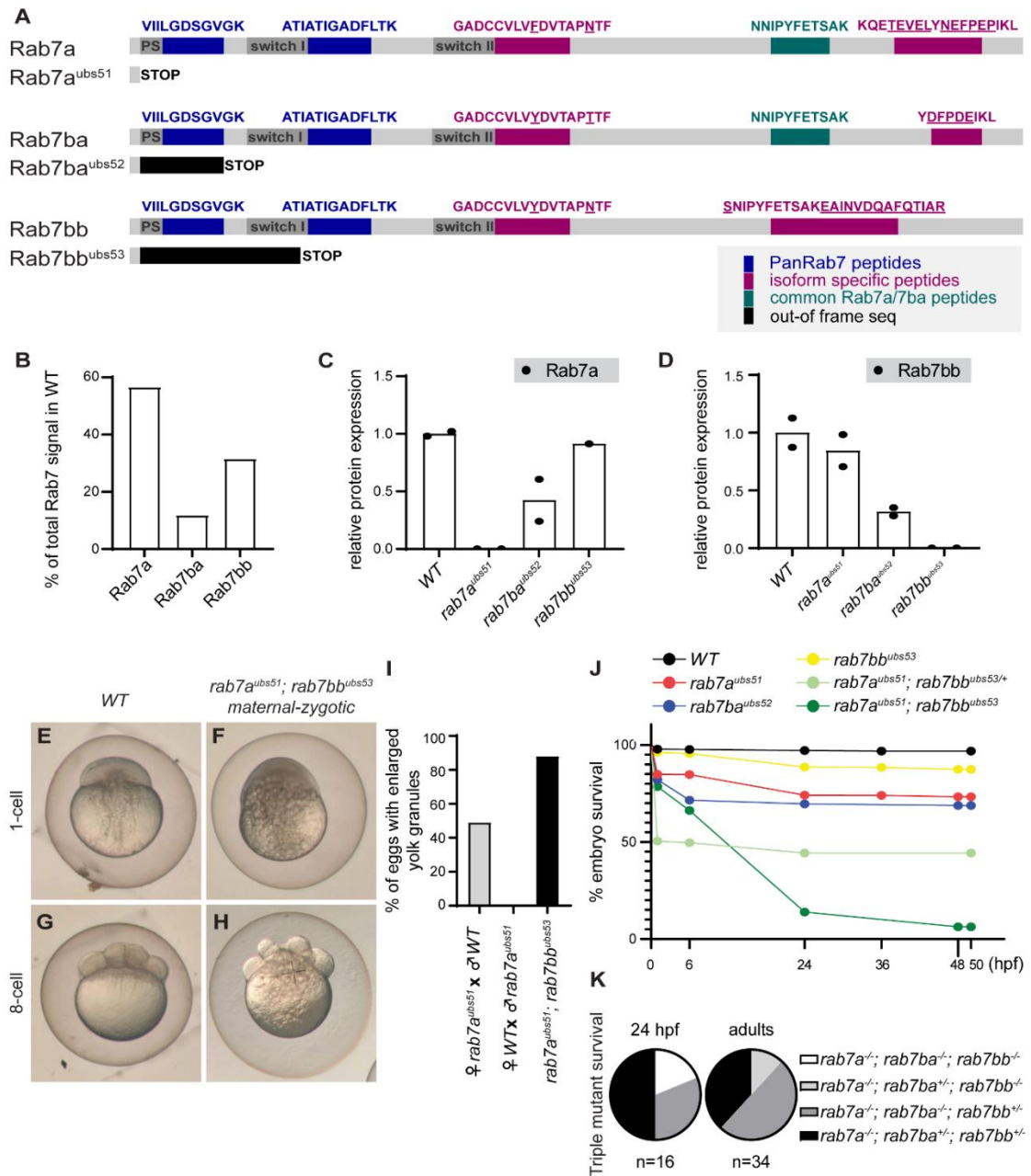


**Figure 13** Characterisation of *rab7* mutant isoforms

**A** All three *rab7* amino acid sequences and their predicted mutant sequences. Peptides used for the Mass Spectrometry experiments are shown on top of each sequence. Peptides that recognise all three isoforms are shown in blue (PanRab7), isoform-specific peptides are shown in magenta and the common peptide for Rab7a and Rab7ba is shown in green. **B** Graph showing the contribution in % of the individual Rab7 isoforms to total Rab7 protein in wild-type (n= 2 pools of 20 embryos). **C and D** Individual value scatter plots of relative protein expression of the three different Rab7 isoforms. Levels were measured in two different pooled samples of wild-type, *rab7a mat-zyg*, *rab7ba mat-zyg* and *rab7bb mat-zyg* homozygous embryos. Values were then normalized to total amount of protein measured per sample and to the amount of wild-type sample (n= 2 pools of 20 embryos). **G-J** Bright field images of wild-type or maternal-zygotic *rab7a; rab7bb* double homozygous mutant embryos at 1-cell stage and 8-cell stage. **K** Bar graph showing the percentage of embryos with enlarged yolk granules in different *rab7* mutant crosses (n= 289-1515 embryos, N=3 different single crosses per condition). **L** Survival plot of clutches from different mutant crosses. Percentage of surviving embryos from wild-type and *rab7a*, *rab7ba* and *rab7bb* homozygous incrosses, as well as incrosses from *rab7a* homozygous, *rab7bb* heterozygous adults and *rab7a; rab7bb* double homozygous parents (n=499-1438 embryos N= 2-7 crosses per condition.). **M** Triple mutant survival from a cross of a *rab7a<sup>-/-</sup>; rab7ba<sup>-/-</sup>; rab7bb<sup>-/-</sup>* mother and a *rab7a<sup>-/-</sup>; rab7ba<sup>-/-</sup>; rab7bb<sup>-/-</sup>* father (n=16 embryos at 24hpf, 34 adults after 3 months).

#### 4.1.3.5 Viability of *rab7* mutant alleles

Since *rab7* is expected to play an important role in cell survival in general, we investigated the viability of the generated null mutant alleles. Single mutants of *rab7a*, *rab7ba* and *rab7bb* resulting from heterozygous in-crosses were viable and fertile (Fig 18 E-F). Adults arising from these crosses showed normal mendelian distribution after 3 months (Fig 18G). Given the transcriptomics data, we argued that maternally deposited mRNAs or protein could rescue certain defects in homozygous embryos coming from heterozygous crosses. Using maternal-zygotic mutants (thus removing all maternally deposited mRNA and protein), we found a higher mortality in all *rab7* single mutants (Fig 13J). Survival rate drops from 97% in wild-type embryos to 84% in *rab7bb* homozygous mutants, to 59% for *rab7a* and to 76% in *rab7ba* homozygous mutants.

To find out whether there was some degree of redundancy in function between the three *rab7* alleles, maternal-zygotic double mutants were analysed. While *rab7a; rab7ba* double homozygous fish did not show any change in viability compared to their single mutant variants, *rab7a; rab7bb* double homozygous mutants showed a drastic decrease in viability. The survival of offspring from in-crosses of *rab7a*<sup>-/-</sup>; *rab7bb*<sup>+/-</sup> fish was reduced to 40%. In double homozygous in-crosses, survival was reduced to 8% within the first 24 hours (Fig 13J). These results shows that *rab7bb* shares some redundant function with *rab7a* and that the lowly-expressed *rab7ba* plays indeed a less important role for zebrafish embryo survival.

Despite the high lethality of *rab7a; rab7bb* double maternal-zygotic mutant embryos, roughly 10% of the embryos did survive. To test whether this might be due to residual *rab7ba* protein, we crossed fish that result in triple homozygous mutant progeny. We crossed a *rab7a*<sup>-/-</sup>; *rab7ba*<sup>-/-</sup>; *rab7bb*<sup>+/-</sup> female to a *rab7a*<sup>+/-</sup>; *rab7ba*<sup>+/-</sup>; *rab7bb*<sup>-/-</sup> male and screened the clutch for triple homozygous embryos using a four-primer multiplex PCR assay (for further details, see Methods). Out of 16 embryos, 3 were triple homozygous (Fig 13K), which is in accordance with the expected mendelian rate of 1/8. However, when screening 3 months old siblings of the same cross, 0/34 adult fish were triple homozygous. These data demonstrate that zebrafish which lack all Rab7 proteins are not viable.

#### 4.1.3.6 Increase of yolk granule number in *rab7* maternal-zygotic homozygous mutants

Aside from embryo survival, loss of Rab7 may have severe defects in early development. A very early phenomenon linked to *rab7* function is the endocytic traffic pathway in the embryonic yolk. Loss of Rab7 or its GEF leads to a failure of yolk proteins to reach yolk granules in *C. elegans* (Poteryaev et al., 2007). In zebrafish, 1-cell-stage embryos of single *rab7a* or double *rab7a; rab7bb* mutants showed an increase in the size of yolk granules (Fig 13 E-I). This phenotype reflects a similar phenotype



described in *C. elegans* (Poteryaev et al., 2007) and appears to be due to maternal contribution, since in progeny coming from *rab7a* homozygous mothers that were crossed to wild-type males, 49% of the embryos showed this phenotype. In contrast, 0% of embryos coming from wild-type mothers, crossed to *rab7a* homozygous males, showed any defects linked to yolk granules. The effect became even stronger in progeny from *rab7a; rab7bb* double homozygous adults. In this scenario, 88% of embryos showed an increase in yolk granules (Fig 13I). Coincidentally, the frequency of occurrence of this phenotype was similar to the percentage of embryos that did not survive in these crosses. In fact, the majority of the 10% surviving embryos in these double homozygous in-crosses did not show this yolk phenotype; however, in rare cases, even embryos with yolk granules survived more than 24hpf. Occasionally, these embryos also showed defects in cell spacing in the blastodisc. In Fig 13H, the usually well-spaced organization of the cells (Fig 13F) was lost in eggs with yolk granules (Fig 13H).

#### 4.1.3.7 Lumen formation in *rab7* single and double mutants is only slightly impaired

During blood vessel anastomosis, transcellular lumen formation occurs upon the formation of tip cell contacts and can be followed using the membrane marker *Tg(kdrl:mcherry-CAAX)* and a driver line forcing expression in the endothelial cells. The apical lumen front can be observed in trunk blood vessels roughly from 30 hpf onwards, expanding from the dorsal aorta dorsally through the newly forming vessels. Once the newly formed vascular loops have opened up to allow blood flow, blood pressure increases, and the lumen diameter expands (Fig 14A). To investigate whether Rab7 plays a role in lumen formation in zebrafish as suggested by studies in other systems (Caviglia et al., 2016, 2017), *Tg(kdrl:mcherry-CAAX)* embryos were analysed by confocal live imaging in order to follow initial lumen formation, lumen fusion and lumen maintenance in *rab7* mutant fish. Lumen formation was observed in embryos homozygous mutant for each of the three *rab7* loss-of-function alleles and in embryos homozygous for the two *rab7* double mutants analysed (*rab7a; rab7ba* and *rab7a; rab7bb*) (Fig 14 B-E); all blood vessels analysed formed a lumen during anastomosis and subsequently maintained it until the end of data acquisition. To quantify lumen maintenance, the diameter of the lumen was measured perpendicular to the vessel orientation at three different positions (Fig 14F). Lumen diameter was slightly reduced in *rab7ba* homozygous mutants, and in *rab7a; rab7ba* double homozygous mutants (Fig 14G). Keeping in mind the strong maternal contribution of *rab7a* and *rab7bb*, we wanted to analyse whether this contribution plays a role during anastomosis and

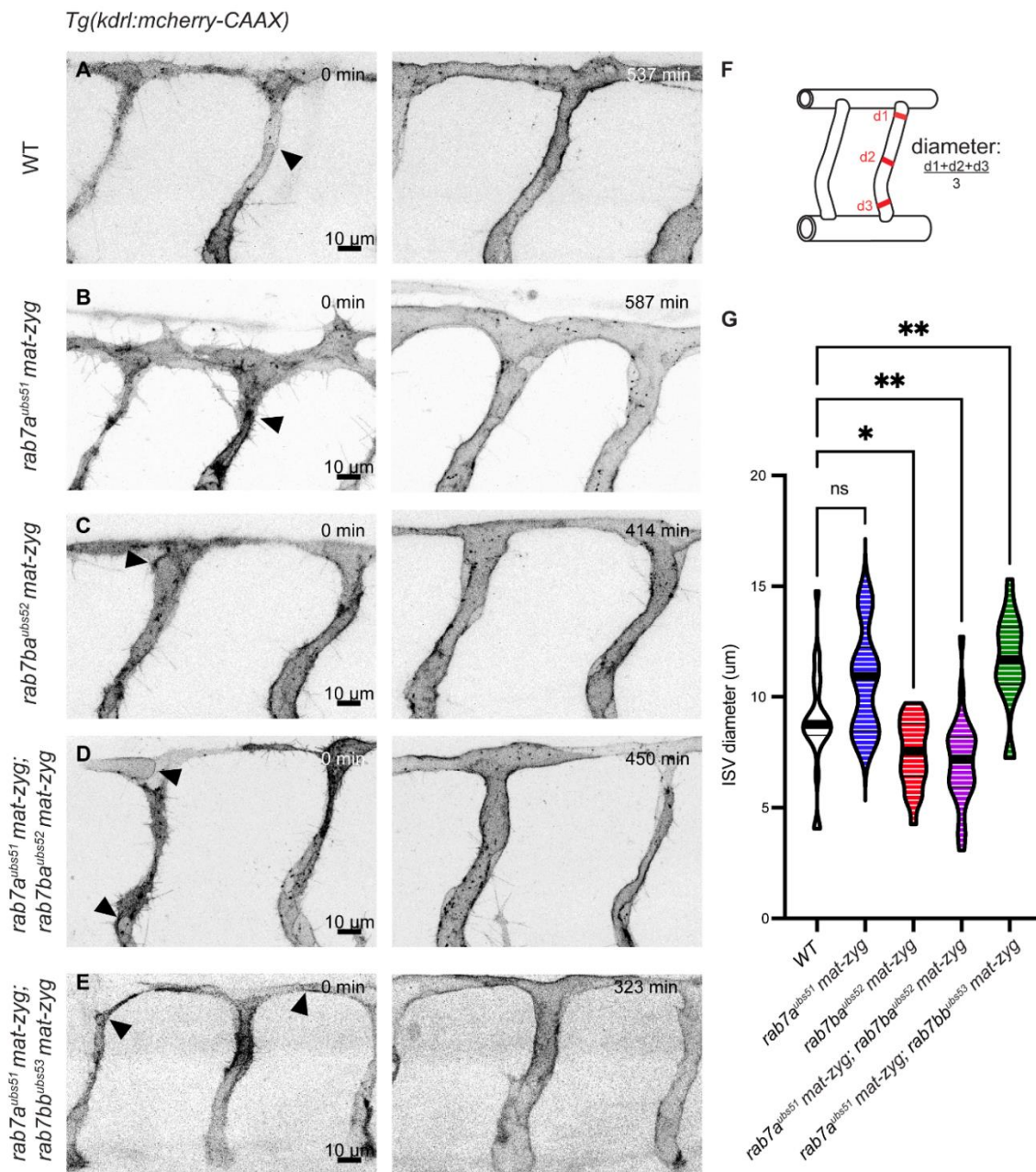


**Figure 14** Vascular lumen defects in *rab7* mutants

**A-E** Confocal still pictures from time-lapse movies from transgenic *Tg(kdrl:EGFP-CAAX)<sup>S916</sup>* embryos at 34-44 hpf showing blood vessel lumenization in wild-type (**A**), maternal zygotic homozygous mutant for *rab7a* (**B**), *rab7ba* (**C**), maternal-zygotic double homozygous mutant for *rab7a; rab7ba* (**D**) and *rab7a;rab7bb* (**E**). Black arrowheads show invaginating luminal front. The final image represents the fully lumenized state of the blood vessels around 44 hpf. **F** Schematic representation of how lumen diameter was measured. The diameter of the vessel was measured perpendicular to vessel axis at 3 positions. The membrane marker *Tg(kdrl:mcherry-CAAX)<sup>S916</sup>* was used as reference to how far the lumen expanded. **G** Violin plot showing lumen diameter in *rab7* mutants. Median is indicated by thick black line (wild-type: N= 8 fish, n= 24 blood vessels; *rab7a*: N= 4, n= 10 (maternal-zygotic homozygous); *rab7ba*: N= 8, n= 22 (maternal-zygotic); *rab7a; rab7ba*: N= 10, n= 31 (maternal-zygotic); *rab7a; rab7bb*: N=7, n= 19 (maternal-zygotic)).

analysed embryos from homozygous in-crosses. These embryos showed a significantly reduced diameter in maternal-zygotic homozygous *rab7ba* mutants and maternal-zygotic homozygous *rab7a; rab7ba* double mutants. The lumen diameter was increased when comparing embryos that were zygotic homozygous mutants for *rab7a*, to maternal-zygotic homozygous mutants for *rab7a* or to double maternal-zygotic homozygous mutant for *rab7a; rab7bb*. Similar to the lethality studies, this indicates again that *rab7a* and *rab7bb* share some redundant function.

#### 4.1.3.8 *rab7* single and double mutants are capable of transcellular lumen formation and fusion

Since Rab7a appears to associate with the apical membrane during transcellular lumen formation (Fig. 10-11), we then investigated the loss of Rab7 in transcellular lumen formation. To do so, we examined the process of anastomosis and focused only on blood vessels that connect and expand their lumen via this process. To differentiate between the two different lumen formation mechanisms (cord hollowing vs transcellular lumen), we imaged the process in *Tg(fli:Pecam1-EGFP)* embryos, which allows us to follow cell-cell junctions and thus identify individual endothelial cells. In transcellular lumen formation, the lumen forms before junctional rearrangements take place and the newly forming luminal connection is surrounded by a single cell only, visualized by a clearly defined junctional ring and the absence of junctions along the endothelial cell body (see Fig 15A). Henceforth, the lumen expands inside a single cell. If the lumen fusion observed in Fig 15A would have been brought about by cellular rearrangements only (cord hollowing), the visualization of a live junctional marker would have revealed junctions running along the entire vessel.

Time-lapse live imaging of *rab7* mutants expressing both the *Tg(fli:Pecam1-EGFP)* and the *Tg(kdrl:mcherry-CAAX)* marker in endothelial cells showed that transcellular lumen formation was indeed observed in *rab7a* and *rab7ba* single maternal-zygotic homozygous and *rab7a; rab7ba* double maternal-zygotic homozygous embryos (Fig 15 B-D; higher magnification of membrane fusion in Fig 15 B'-D'). In these movies, the apical luminal fronts were observed as they grew towards each other and fused upon contact, thereby forming one continuous lumen in a stretch of vessel characterized by the absence of continuous junctions, indicating that this lumen had fused within a single endothelial cell.

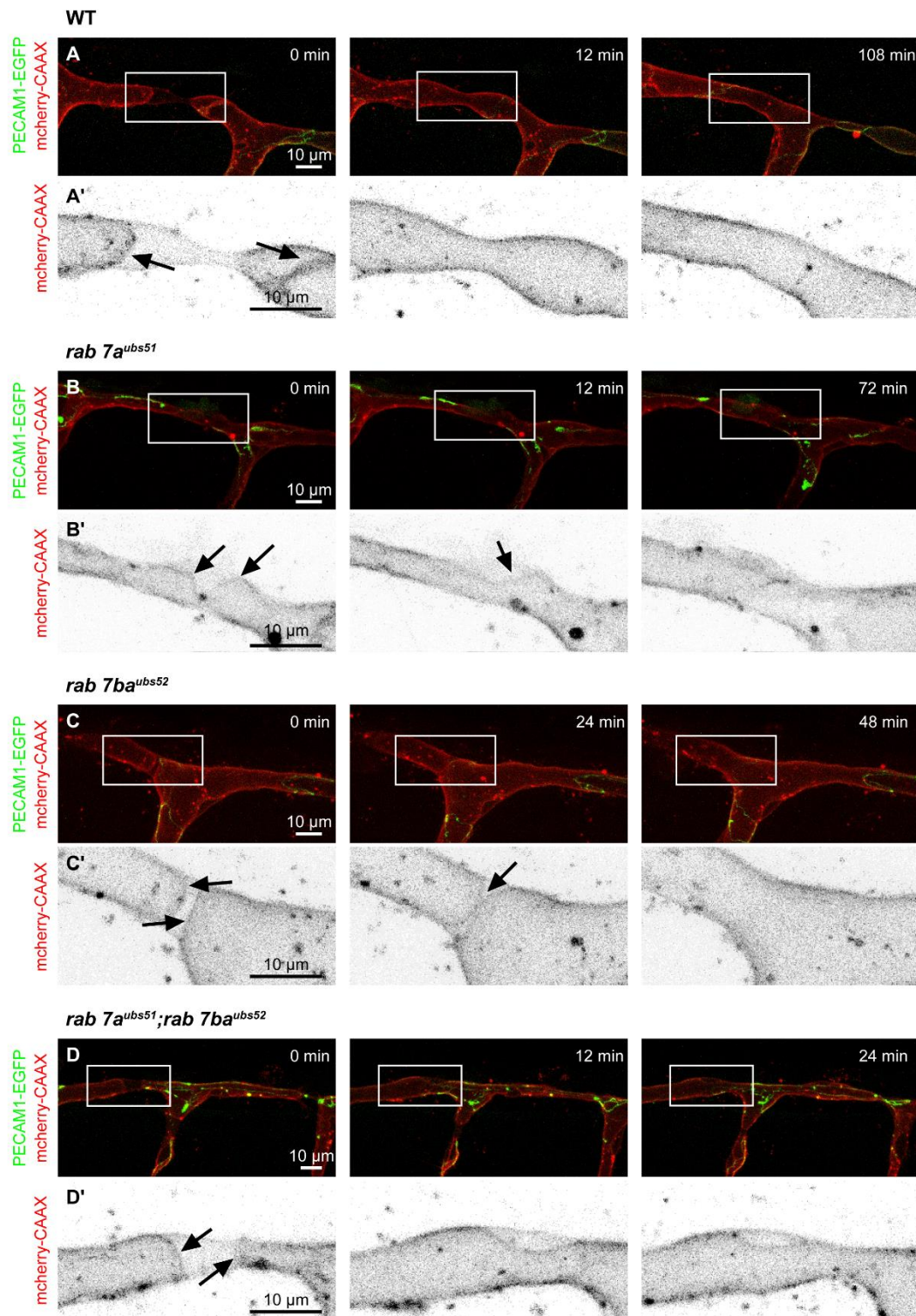


**Figure 15 Lumen fusion in *rab7* mutants**

**A-D** Stills from high resolution confocal imaging of lumen fusion in the DLAV (anterior to the left) of double transgenic *Tg(kdrl:mcherry-CAAX)<sup>s916</sup>; Tg(fli:Pecam1-EGFP)<sup>ncv27</sup>* wild-type (**A**), maternal-zygotic homozygous *rab7a* double (**B**), maternal-zygotic homozygous *rab7ba* (**C**) and maternal-zygotic double homozygous *rab7a<sup>ubs51</sup>; rab7ba<sup>us521</sup>* (**D**) embryos. **A'-D'** Isolated mcherry-CAAX signal labelling the apical membrane of ROIs from A-D. Arrows indicate the invaginating luminal front.

#### 4.1.3.9 *rab7* single and double mutants show differences in late endosomal/lysosomal vesicle size but not vesicle number

A major function of Rab7 is to control fusion of the vesicles in the last step of endosomal trafficking. These late endosomes eventually fuse with lysosomes such that cargo can be degraded. This fusion is orchestrated by Rab7 with the help of its effectors. To investigate whether the trafficking of late endosomes to lysosomes is affected in various *rab7* mutant combinations, the size and number of vesicles positive for the late endosomal/lysosomal marker Lamp2 were measured. The measurement was taken in a defined area around the dorsal-most end of a non-lumenized blood vessel, and all Lamp2-RFP positive vesicles were measured manually (Fig 16 A-C). These measurements showed that vesicle size was significantly reduced in *rab7ba<sup>ubs52</sup>* homozygous embryos and in *rab7a<sup>ubs51</sup>; rab7ba<sup>ubs52</sup>* double homozygous embryos compared to controls (Fig 16 A-C). In *rab7a<sup>ubs51</sup>*, vesicle size was not altered. Lamp1 is sorted into late endosomes and lysosomes from the TGN (Cook *et al.*, 2004) and it has been postulated that *rab7b* has a different function from *rab7a* and plays a role in the shuttling from the TGN to late endosomes (Progida *et al.*, 2010). This might indicate that the observed effect is mostly due to improper trafficking of Lamp2-RFP to late endosomes/lysosomes with the help of Rab7b, and that the effect of Rab7a cannot be studied using the assays we chose. Therefore, a small screen was performed using splice-morpholinos (MOs) against all three isoforms of the zebrafish *rab7* genes, blocking splicing of exon2 (Fig 16 G-J). Strikingly, injection of splice-MO in *TgBAC(Lamp2-RFP)* embryos reveals that in embryos injected with MO against *rab7ba*, the Lamp2-RFP signal was lost in the entire embryo compared to standard-MO injected siblings, or to uninjected control embryos. Measurements of vesicles in embryos injected with splice-MO against either *rab7a* or *rab7bb* showed a strong and significant increase of vesicle size compared to standard-MO injected embryos (Fig 16 G, I and J). Together, these results indicate that loss of *rab7ba* might play a role in proper localization of Lamp2-RFP. Our findings also indicate that vesicle size in embryos mutant for the two functionally redundant *rab7a* and *rab7bb* is expected to be increased, in line with the MO data, and that, in order to use the Lamp2-RFP signal as a marker, Rab7ba needs to be present.

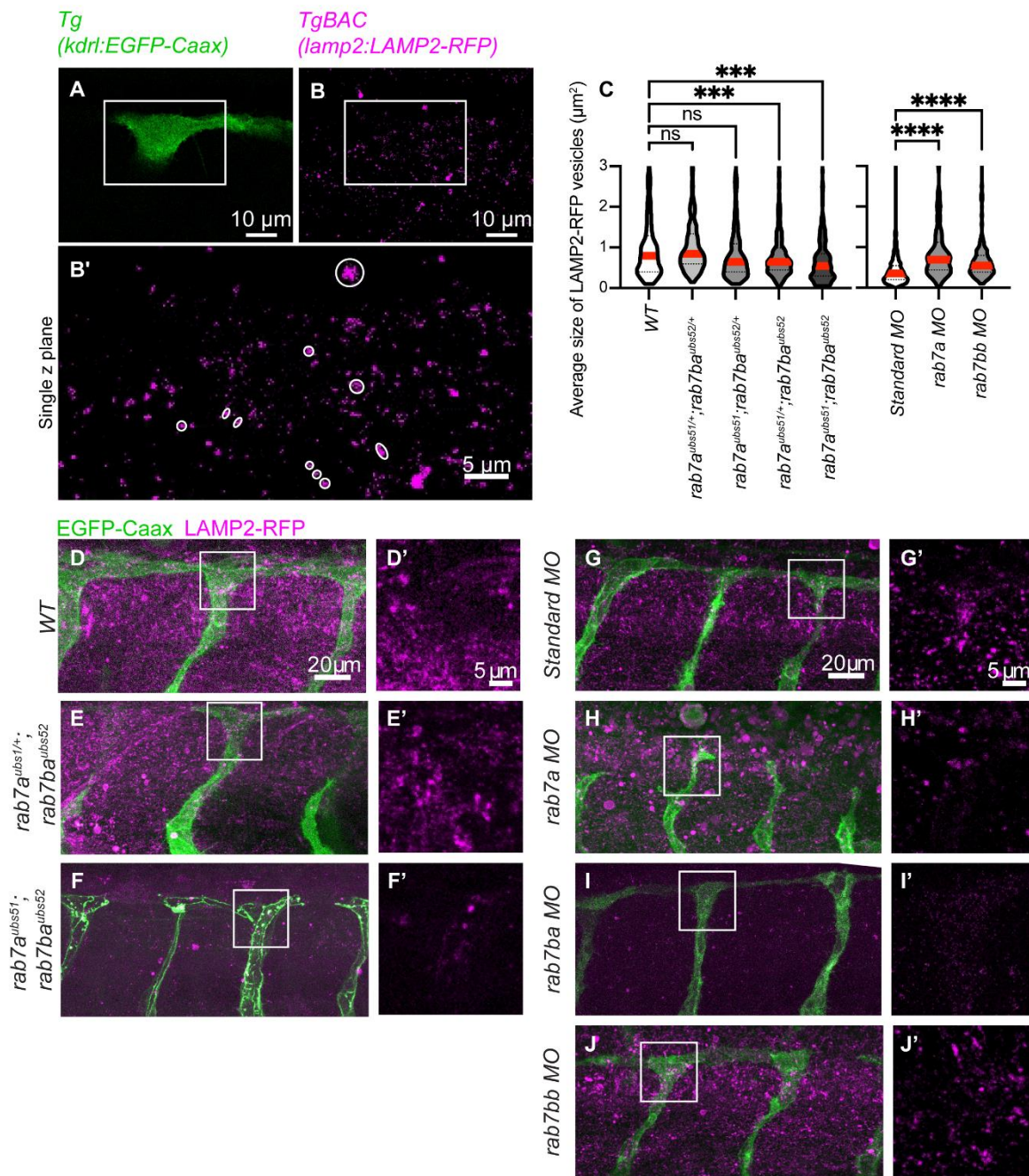


**Figure 16 Vesicle analysis in *rab7* loss-of-function**

**A-B'** Representation of measurement of vesicle size. Single z-stack of a non-lumenized tip-cell is chosen using the endothelial marker *kdrl:EGFP-CAAX*. **B'** In a zoom-in window of the ROI in B, every Lamp2-RFP positive signal is measured (using as upper cut off 2 pixels). **G** Violin plots of measured vesicle sizes in *rab7* mutants (wild-type N= 5, n= 283, *rab7a*;*rab7ba* heterozygous N= 4, n= 347, *rab7a* homozygous *rab7ba* heterozygous N= 5, n=356, *rab7a* heterozygous; *rab7ba* homozygous N= 7, n= 539, *rab7a*;*rab7ba* homozygous N= 6, n= 260,  $p^{***}<0.001$ , red line indicates the median) and in *rab7* morphants (standard-MO N= 8, n= 930, *rab7a*-MO N= 6, n= 129, *rab7bb*-MO N= 6, n=259,  $p^{****}<0.0001$ , red line indicates the median). **D-J'** Confocal images expressing an endothelial marker and the late endosome marker Lamp2 (double transgenic embryos *Tg(kdrl:EGFP-CAAX);TgBAC(Lamp2-RFP)<sup>pd1117</sup>* or *Tg(fli:Pecam1-EGFP)<sup>ncv27</sup>;TgBAC(Lamp2-RFP)<sup>pd1117</sup>*. **D'-J'** Zoom-in areas indicated in D-J showing isolated Lamp2-RFP signal. **D-F** Images from wild-type or *rab7* mutant embryos. **G-J** Images from embryos injected with a standard morpholino or *rab7* morpholinos.

#### 4.1.4 Discussion

##### 4.1.4.1 The role of *rab7bb*

Many genes are duplicated in the zebrafish genome when compared to genomes of mammals. This is also the case for *rab7*, for which an additional copy is present in the zebrafish genome when compared to mammals. We find that *rab7ba* and *rab7bb* are more closely related to each other than to the third copy, *rab7a*, and lie in chromosomal regions that share many genes. We also find that the previously unstudied *rab7* gene, *rab7bb*, is expressed in zebrafish at a similar level as *rab7a*. Using targeted mass spectrometry, we show that, at the protein level, Rab7a is the most abundant of the three Rab7 proteins, with almost double the levels of Rab7bb and four to five times the levels of Rab7ba. This is in line with previously acquired transcriptomics data (Lawson et al., 2020). We also show that combined loss of *rab7a* and *rab7bb* increases the severity of all observed phenotypes in single *rab7a* mutants (yolk granules, survival of embryos and increase in lumen diameter). This is not the case in *rab7a*; *rab7ba* double mutants. This shows that *rab7bb* alone is sufficient to supplement for *rab7a* function and has thus overlapping functions with *rab7a*; no such redundancy is seen with *rab7ba*. This might also be due to the much lower levels of Rab7ba; further analyses would be required to definitely answer this issue.

##### 4.1.4.2 Targeted mass spectrometry of *rab7* mutants

To validate our generated *rab7* mutant lines we used a targeted mass spectrometry approach. Reference peptides have been designed that are either specific for a single proteoform, or appear in two or three of the Rab7 proteins. Analysis of maternal-zygotic single homozygous embryos revealed that none of the generated mutant alleles express any levels of wild-type Rab7. The used reference peptides would also detect any protein expressed from additional, downstream Methionine and show that there is also no shortened fragment of Rab7 produced in the respective mutant. Additionally, we do not see any upregulation of any remaining *rab7* gene in any of the mutants. This shows that wild-type levels of the complementary *rab7* genes is sufficient to rescue zebrafish embryos. Rab7ba levels were too low to detect Rab7ba with the single proteoform specific reference peptide, therefore, a pan Rab7a-Rab7ba reference peptide in combination with the results of the Rab7a specific peptide was used to determine the levels of Rab7ba.

##### 4.1.4.3 Targeted mass spectrometry of *rab7* mutants

To validate our *rab7* mutant lines, we used a targeted mass spectrometry approach. Reference peptides were designed that are either specific for a single proteoform or are shared between two or three of the different Rab7 proteins. Analysis of maternal-zygotic homozygous mutant embryos of a single *rab7* allele revealed that none of the mutant alleles express significant levels of the equivalent

wild-type Rab7. Additionally, the reference peptides would also detect any protein translated and expressed from alternative/cryptic translation start sites. Hence, our results reveal that there are no shortened fragments of Rab7 produced in the respective mutants. Together, these observations strongly indicate that the three mutant alleles we generated represent null alleles. Furthermore, in none of the individual mutants did we find upregulation of any of the other two wild-type Rab7 isoforms at the protein level. This demonstrates that wild-type levels of the other *rab7* genes are sufficient to rescue zebrafish embryos to adulthood.

#### 4.1.4.4 *rab7* maternal contribution and survival

The analyses of the mutant *rab7* lines we generated revealed that the total loss of Rab7 is lethal, similar to what has been reported in other organisms (*Kawamura et al., 2012; Poteryaev et al., 2007*). While zebrafish lacking all three copies of *rab7* were identified at 24hpf, they die before reaching adulthood. However, our results also show that the lowest expressed gene, *rab7ba*, is sufficient for 10% of double mutant embryos of the other two alleles (*rab7a; rab7bb*) to survive. We find that the two *rab7* alleles, *rab7a* and *rab7bb*, which were predicted by transcriptomics data to be expressed before maternal-to-zygotic transition, are indeed required for early embryo development. 1-cell stage zebrafish embryos lacking maternal contribution of *rab7a* show a phenotype with enlarged yolk granules, caused most likely by a defect in the deposition and fusion of yolk granules with lysosomes, as has previously been described in *C. elegans* (*Poteryaev et al., 2007*). This phenotype is more severe when both *rab7a* and *rab7bb* are lost. For *rab7a*, we demonstrate that this phenotype is linked to maternal contribution.

#### 4.1.4.5 Rab7 in vesicular trafficking and vascular lumen formation and the different role of Rab7ba

Rab7 co-localises with the membrane marker CAAX and the late endosomal/lysosomal marker Lamp2 at dots, which co-migrate along the expanding apical surface during transcellular lumen formation. Although other members of the endocytic pathway (Rab5c: early endosome; Rab11a: recycling endosome) are present at dots or in proximity to the apical membrane, they did not co-localise with the marker CAAX. Our data suggest that the presence of the late endocytic pathway at apical surfaces might be linked to lumen formation and expansion, similar to what has been proposed for the trachea system in *Drosophila* (*Caviglia et al., 2016, 2017*).

Further analysis of the late endosomes/lysosomes using the Lamp2 marker in *rab7* mutants, revealed that in the absence of Rab7ba, endosomal/lysosomal size is reduced. This is independent of whether Rab7a is present or not. Strikingly, the Lamp2-RFP signal is lost in *rab7ba* morphants. It has been previously shown that *rab7a* and *rab7b* exert different functions in vesicular trafficking and *rab7b*



was proposed to shuttle newly synthesized hydrolases and lysosomal membrane proteins such as Lamp1 to the late endosome/lysosome from the TGN (Cook *et al.*, 2004; Progida *et al.*, 2010). Our results indicate that in zebrafish, this function is mediated by Rab7ba. We have not been able to analyse the expression of Lamp1 in wildtype or any of the *rab7* mutants, due to the lack of the required tools, such as specific antibodies or transgenic reporter lines. Our data indicate that all Rab7 isoform share some functions but apparently carry out independent functions.

To investigate the potential role of different *rab7* alleles in apical membrane fusion and lumen formation in the zebrafish vasculature, we performed *in vivo* live imaging using markers labelling endothelial membranes (*Tg(kdrl:mcherry-CAAX)*). Vascular development was unaltered in all mutants and mutant combinations analysed, and all blood vessels formed normally and were perfused. However, when we measured lumen diameter in the different mutants, we observed two trends: 1) the lumen was increased in *rab7a* and *rab7a; rab7bb* single and double mutants, respectively, and 2) the lumen was decreased in *rab7ba* and *rab7a; rab7ba* double mutants, respectively, meaning that Rab7a and Rab7ba exert different effects on lumen properties. Lumen diameter can be a readout for junctional stability, cell rearrangement and/or blood pressure (Red-Horse and Siekmann, 2019). We did not further investigate how the observed phenotypes were related to Rab7 function.

To further address the role of Rab7 in transcellular lumen formation, we used the apical marker (*Tg(kdrl:mcherry-CAAX)*) together with the endothelial junction marker *Tg(fli:Pecam1-GFP)*. We found that in *rab7a*, *rab7ba* single and *rab7a; rab7ba* double homozygous mutants, transcellular lumen formation and lumen fusion takes place in a manner comparable to wild type embryos.

To determine whether the complete absence of Rab7 results in more prominent defects in sprouting angiogenesis and vascular lumen formation, in particular during apical membrane fusion, additional approaches will be required. A conditionally inactivatable allele of *rab7* could be expressed in a triple mutant embryo to rescue lethality; inactivation of this allele in the vasculature, either by genetic means or by protein degradation tools (other ref; Harmansa and Affolter, 2018) should allow to unravel a potential role of Rab7 in lumen formation *in vivo*. The generation of the required tools, and the validation and analyses of such novel approaches, is beyond the scope of the work described here.

## 4.1.5 Material and Methods

### 4.1.5.1 Zebrafish husbandry

Zebrafish were maintained in standard housing conditions according to FELASA guidelines (Aleström *et al.*, 2020). Experiments were performed in accordance with federal guidelines and were approved by the Kantonales Veterinäramt of Kanton Basel-Stadt (1027H, 1014HE2, 1014G). The following

zebrafish transgenic lines were used: *Tg(kdrl:mCherry-CAAX)<sup>S916</sup>* (Hogan et al., 2009); *Tg(fli1a:EGFP)<sup>Y1</sup>* (Lawson and Weinstein, 2002); *Tg(kdrl:EGFP-CAAX)<sup>ubs47</sup>* (this study), *TgBAC(Lamp2-RFP)<sup>pd1117</sup>* (Rodríguez-Fraticelli et al., 2015), *Tg(fli1:EGFP-Rab7a)<sup>ubs48</sup>* (this study), *Tg(fli1a:Pecam1a-EGFP)<sup>ncv27</sup>* (Ando et al., 2016), *rab7a<sup>ubs51</sup>* (this study), *rab7ba<sup>ubs52</sup>* (this study), *rab7bb<sup>ubs53</sup>* (this study).

#### 4.1.5.2 Constructs

Constructs were cloned using the Multisite Gateway Three-Fragment Vector Construction System (Thermo Fisher Scientific) and destination vectors (ie. pDestTol2CG2) from the Tol2Kit (Kwan et al., 2007).

##### ***fli1:EGFP-rab7a***

For generation of the *fli1: EGFP-rab7a* vector, a pDestTol2CG2-heart-gfp with the independent marker *cmlc2:EGFP*, a *fli1* P-5' entry clone (Addgene, Lawson Lab), an EGFP p-middle entry (Addgene, Kwan, Chien lab) and *rab7a* p-3' entry clone (Clark et al., 2011) were used.

##### ***fli1:EGFP-rab5c***

For generation of the *fli1: EGFP-rab5c* vector, a pDestTol2CG2-heart-gfp with the independent marker *cmlc2:EGFP*, a *fli1* P-5' entry clone (Addgene, Lawson Lab), an EGFP p-middle entry (Addgene, Kwan, Chien lab) and *rab5c* p-3' entry clone (Clark et al., 2011) were used.

##### ***fli1:EGFP-rab11a***

For generation of the *fli1: EGFP-rab5c* vector, a pDestTol2CG2-heart-gfp with the independent marker *cmlc2:EGFP*, a *fli1* P-5' entry clone (Addgene, Lawson Lab), an EGFP p-middle entry (Addgene, Kwan, Chien lab) and *rab11a* p-3' entry clone (Clark et al., 2011) were used.

##### ***kdrl:EGFP-CAAX***

For generation of the *kdrl:EGFP-CAAX* vector, a pDestTol2CG2-eye-bfp with the independent marker *beta-crystalline:BFP* a *kdrl* P-5' entry clone (Addgene, Santoro Lab), an EGFP-CAAX p-middle entry (Addgene, Kristen Kwan, Chien lab) and a poly-A p-3' entry clone (Addgene, Kristen Kwan, Chien lab) were used.

#### 4.1.5.3 Transgenesis

*fli1:EGFP-rab7a* and *kdrl:EGFP-CAAX* plasmids were injected into one-cell stage embryos together with *tol2* mRNA (30 pg mRNA and 20-40 pg DNA/embryo) as previously described (Kawakami et al., 2000). Upon selection of G0 founders, the F1 generations were maintained as stable transgenic lines (*Tg(fli1:EGFP-Rab7a)<sup>ubs48</sup>*, *Tg(kdrl:EGFP-CAAX)<sup>ubs47</sup>*).

#### 4.1.5.4 gRNA synthesis

DNA oligonucleotides encoding gRNAs with invariant adapter sequence were used for each *rab7* gene and were designed using the CHOPCHOP online tool (<https://chopchop.cbu.uib.no>). For gRNA synthesis, each of the gene specific primers (specific sequence in red; *rab7a* TAATACGACTCACTATAGG**GCTCTGACACTATGACATCA**GTTTTAGAGCTAGAAATAGCAAG, *rab7ba* TAATACGACTCACTATAGG**TTTGAGGAGGACCTTTTAC**GTTTTAGAGCTAGAAATAGCAAG or *rab7bb* TAATACGACTCACTATAGG**AAGGATGGCTTCTCGTAAGA**GTTTTAGAGCTAGAAATAGCAAG) was mixed with the constant oligonucleotide (AAAAGCACCGACTCGGTGCCACTTTTTCAAGTTGATAACGGACTAGCCTTATTTAACTTGCTATTCTAGCTCTAAAAC), containing a complementary adapter and a Cas9 recruiting sequence. The resulting DNA was purified by Gel and PCR clean-up Kit (Macherey Nagel) and 0.2 µg of DNA was used for RNA *in vitro* transcription by T7 Megascript Kit (Ambion) according to the manufacturer's protocol.

#### 4.1.5.5 Cas9 protein production

Addgene plasmid pET-28b-Cas9-His was used for Cas9 protein production as previously described (Gagnon *et al.*, 2014). Briefly, the Cas9 protein was expressed in BL21 Rosetta Escherichia coli strain (Novagen) in magic medium at 37 °C for 12 h followed by 24 h at 18 °C. Cells were harvested by centrifugation at 6000rpm for 15 min and stored at 4 °C. The cell pellet was resuspended in 20 mM Tris-HCl buffer (pH 8) containing 0.5 M NaCl and 30 mM imidazole, then ultrasonicated and centrifugated at 140000 rpm at 4 °C for 15 min. The supernatant was loaded on Protino NI-NTA agarose beads equilibrated by the same buffer and incubated for 60min. After 4x washes, protein was eluted with 20mM Tris-HCl buffer (pH 8), containing 0.5 M Imidazole and 0.5 M NaCl, on a column in 1ml stepwise elution. Protein purity was confirmed by SDS-polyacrylamide gel electrophoresis and dialyzed overnight against 20 mM Tris-HCl buffer (pH 8) containing 200 mM KCl and 10mM MgCl<sub>2</sub> and stored at -80 °C.

#### 4.1.5.6 Cas9 protein and gRNA injections

Zebrafish embryos were collected and injected as previously described (Rosen *et al.*, 2009) at one-cell stage using a FemtoJet Injector (Eppendorf) or PV820 injector (WPI) and borosilicate glass needles (outer diameter 1mm, inner diameter 0.5mm, BRAND). For targeted mutagenesis, eggs were injected at one-cell stage with a mixture of gRNA and Cas-9 protein at a 1:1 ratio. Injection mix composition was calculated using the website ([https://lmwebr.shinyapps.io/CRISPR\\_Cas9\\_mix\\_calc/](https://lmwebr.shinyapps.io/CRISPR_Cas9_mix_calc/)) from (Burger *et al.*, 2016). Mutagenesis efficiency was approximately 5% for *rab7a* and approximately 20% for *rab7ba* and *rab7bb*. Germline transmission rate was 30% (3/10) for *rab7a*, 40% (4/10) for *rab7ba* and 50% (3/6) for *rab7bb*.

#### 4.1.5.7 Genotyping

For each generated allele, a multiplex four primer PCR was established. The following primers were used for *rab7a*: outer forward primer GGAAGTCTGTGTGTTAACAGAAGCCGG, outer reverse primer CCACGCCCTCTTACTGTTAGTTTGC, mutant specific primer GACATAGTGCTTTCTTCAAGG, wt specific primer CAGAAGAAGTTTCTTCTTGATGTC. For *rab7ba*: outer forward primer GTGTAAACAGCCACAAGCC, outer reverse primer CACTGATAGCGTCTATGC, mutant specific primer CCAGAATCCCCTAGGGGAAGCC, wt specific primer CCTCCTCAAAGTGATCATCCTAGG. For *rab7bb*: outer forward primer GTTAGACCCGAAGTGCATTTTCG, outer reverse primer GAAACCCACATGAACACGG, mutant specific primer GGCTTCTCGTGCTGCTGAAGG, wt specific primer GCAGCACCTTCTTACGAGAAGC. Each PCR results in 3 different bands. A larger non-specific band (outer) and two smaller diagnostic bands (for wildtype or mutant allele). For *rab7a* these are: 645bp (outer), 390bp (wildtype allele), 268bp (mutant allele). For *rab7ba*: 492bp (outer), 223bp (wildtype allele), 297bp (mutant allele). For *rab7bb*: 380bp (outer), 246bp (wildtype allele), 161bp (mutant allele).

#### 4.1.5.8 Morpholino Injections

One- to two-cell stage embryos were injected with 4 ng of antisense morpholino oligonucleotide (Gene Tools) targeting the splice donor site of Exon2 of the respective *rab7* gene (*rab7a*: 5'-GTTGATTGCGAGAACTCACCCGGA-3'; *rab7ba*: 5'-ATGCTGAACAAAACACTTACCCAGA-3'; *rab7bb*: 5'-AAAGCCATCACTTACCCAGAATCCC-3'). All MOs were validated via an RT-PCR assay, in which the absence of Exon2 were validated.

#### 4.1.5.9 Image acquisition

Live embryos were selected via their fluorescence signal, anesthetized in E3 with 1x tricaine (0.08%, pH 7, Sigma) and mounted in glass bottom Petri dishes (0.17 mm, MatTek) in 0.7% low-melting-point agarose (Sigma) containing 1x tricaine and 0.003% 1-phenyl-2-thiourea (PTU; Sigma-Aldrich) as previously described (Kotini et al., 2022). For live imaging of lumen invagination, an Olympus SpinD (CSU-W1) spinning disc microscope equipped with a dual camera system and a 60x (NA= 1.5) oil objective was used. Z-stacks were made with a step size of 0.2  $\mu$ m and frames were acquired every 2-30 sec. For live imaging of vascular development, a Leica SP5 confocal microscopes equipped with a 40x(NA=1.1) water immersion objective was used. Z-stacks were made with a step size of 0.35-0.5 $\mu$ m and frames were acquired every 12-25 min.

#### 4.1.5.10 Quantification of vessel diameter

Measurements were done using ImageJ. Blood vessels were measured at three different points along the trunk blood vessels. Measurements were taken perpendicular to the vessel axis at each respective point. At the end an average of all three measurements was plotted.

#### 4.1.5.11 Quantification of Lamp2-RFP vesicle size

Vesicle size was analysed manually using ImageJ. An area of interest of 200-200 pixels (1985 $\mu\text{m}^2$ ) was selected around the T-shaped tip cell of developing sprouts. Within this area, ROIs were drawn around every Lamp2-RFP positive dot, with an upper cut-off size of 3 pixels. Every single vesicle was plotted individually. As a reference point, the last time frame before the cell was lumenized was used.

#### 4.1.5.12 Targeted MS of rab7 proteoforms

##### 4.1.5.12.1 Sample preparation

Sample preparation was performed using the s-trap protocol (Protifi, NY, US). Here, 10-20 embryos were deyolked using forceps in 1X E3 and immediately stored in an empty Eppendorf tube on ice. Embryos were sonicated using glass beads in Bioruptor in 20 $\mu\text{l}$  lysis-buffer (5% SDS, 0.1M triethylammonium bicarbonate (TEAB), 10mM tris (2-carboxyethyl) phosphine, pH 8.5). 20 cycles with 30 seconds on and 30 seconds off were used. Samples were then incubated at 95°C and 300 RPM for 10 min. 1 $\mu\text{l}$  of iodoacetamide was added and the samples were incubated in the dark at 25°C for 30min. Not more than 50 $\mu\text{g}$  of sample was loaded onto the S-trap column after addition of phosphoric acid to a final concentration of 1.2% and 330 $\mu\text{l}$  S-trap buffer (90% Methanol and 10% 1M TEAB, pH 8.5). After a spin down at 4000g for 1min, the column was washed 3 times with S-trap buffer. Afterward the sample was digested using 20 $\mu\text{l}$  of digestion buffer and 0.75 $\mu\text{g}$  of trypsin. After 1h of incubation at 47°C, the generated peptides were collected. For this, 40 $\mu\text{l}$  of S-trap buffer, 40 $\mu\text{l}$  of 0.2%formic acid and 35 $\mu\text{l}$  of 50% acetonitrile acid were added stepwise to the column followed by centrifugation at 4000g for 1 min in between. Peptides were dried for 1h in a speed vac. Peptides were dissolved in LC buffer (0.1% formic acid in water) and the peptide concentration determined using a SpectroStar nanodrop spectrophotometer (BMG Labtech, Germany) and set to 0.5  $\mu\text{g}/\mu\text{L}$ .

##### 4.1.5.12.2 Targeted Liquid Chromatography-Mass Spectrometry (LC-MS) Analysis

Parallel reaction-monitoring (PRM) assays (Gallien *et al.*, 2012; Peterson *et al.*, 2012) were generated from a mixture of proteotypic heavy reference peptides containing 50 fmol/ $\mu\text{L}$  of each (Pan-Rab7 peptides: VIILGDSGVGK, ATIGADFLTK; common Rab7a/Rab7ba peptide: NNIPYFETSAK; Rab7a specific peptides: GADCCVLVFDVTAPNTFK, QETEVLYNEFPEPIK; Rab7ba specific peptide: GADCCVLVYDVTAPNTFK; Rab7bb specific peptides: GADCCVLVYDVTAPNTFK, SNIPYFETSAK, JPT Peptide Technologies GmbH). 2

$\mu\text{L}$  of this standard peptide mix were subjected to LC–MS/MS analysis using a Q Exactive plus Mass Spectrometer fitted with an EASY-nLC 1000 (both Thermo Fisher Scientific) and a custom-made column heater set to  $60^{\circ}\text{C}$ . Peptides were resolved using an EasySpray RP-HPLC column ( $75\mu\text{m} \times 25\text{cm}$ , Thermo Fisher Scientific) and a pre-column setup at a flow rate of  $0.2 \mu\text{L}/\text{min}$ . The mass spectrometer was operated in DDA mode. Each MS1 scan was followed by high-collision-dissociation (HCD) of the precursor masses of the imported isolation list and the 20 most abundant precursor ions with dynamic exclusion for 20 seconds. Total cycle time was approximately 1 s. For MS1,  $3\text{e}6$  ions were accumulated in the Orbitrap cell over a maximum time of 50 ms and scanned at a resolution of 70,000 FWHM (at 200 m/z). MS1 triggered MS2 scans were acquired at a target setting of  $1\text{e}5$  ions, a resolution of 17,500 FWHM (at 200 m/z) and a mass isolation window of 1.4 Th. Singly charged ions and ions with unassigned charge state were excluded from triggering MS2 events. The normalized collision energy was set to 27% and one microscan was acquired for each spectrum.

The acquired raw-files were searched using the MaxQuant software (Version 1.6.2.3) against a *Danio rerio* (Zebrafish) database (downloaded from [www.uniprot.org](http://www.uniprot.org) on 2021/11/02, in total 46,848 entries) using default parameters except protein, peptide and site FDR, which were set to 1 and Lys8 and Arg10. The search results were imported into Skyline (v21.1.0.278) (MacLean, Tomazela et al. 2010) to build a spectral library and assign the most intense transitions to each peptide. An unscheduled mass isolation list containing all peptide ion masses was exported and imported into the Q Exactive Plus operating software for PRM analysis. Here, peptide samples for PRM analysis were resuspended in 0.1% aqueous formic acid, spiked with the heavy reference peptide mix at a concentration of 2 fmol of heavy reference peptides per  $1 \mu\text{g}$  of total endogenous peptide mass and subjected to LC–MS/MS analysis on the same LC-MS system described above using the following settings: The MS2 resolution of the orbitrap was set to 17,500/35,000 FWHM (at 200 m/z) and the fill time to 50/110ms for heavy/light peptides. AGC target was set to  $3\text{e}6$ , the normalized collision energy was set to 27%, ion isolation window was set to 0.4 m/z and the first mass was fixed to 100 m/z. A MS1 scan at 35,000 resolution (FWHM at 200 m/z), AGC target  $3\text{e}6$  and fill time of 50 ms was included in each MS cycle. All raw-files were imported into Skyline software for protein / peptide quantification. To control for sample amount variations during sample preparation, the total ion chromatogram (only comprising precursor ions with two to five charges) of each sample was determined using Progenesis Q1 software (Nonlinear Dynamics (Waters), Version 2.0) and used for normalization. Normalized ratios were further normalized relative to the control condition and the median ratio among peptides corresponding to one protein was reported.

#### 4.1.5.12.3 PRM-MS based Quantification of Rab7 Isoforms

In order to determine how much of the single isoform contributes to the overall abundance of Rab7 protein in zebrafish, measurements with the Pan-Rab7 peptide in *rab7a*; *rab7ba* double homozygous mutants were taken. In this mutant combination, the remaining signal comes exclusively from *rab7bb* expression. Signal intensity was three times weaker than in wild-type and therefore 31% of the signal detected in the wildtype originates from expression of Rab7bb alone. To determine the amount of Rab7a and Rab7ba in the remaining 69%, measurements with the Pan-Rab7a-Rab7ba peptides, detecting the combined Rab7a/Rab7ba signal, were used. Analysis of *rab7a* and *rab7ba* single mutants show that Rab7a is around 5 times more abundant than Rab7ba. This means that the remaining 69% of wildtype Pan-Rab7 signal is split into 57% Rab7a signal and 12% Rab7ba signal.

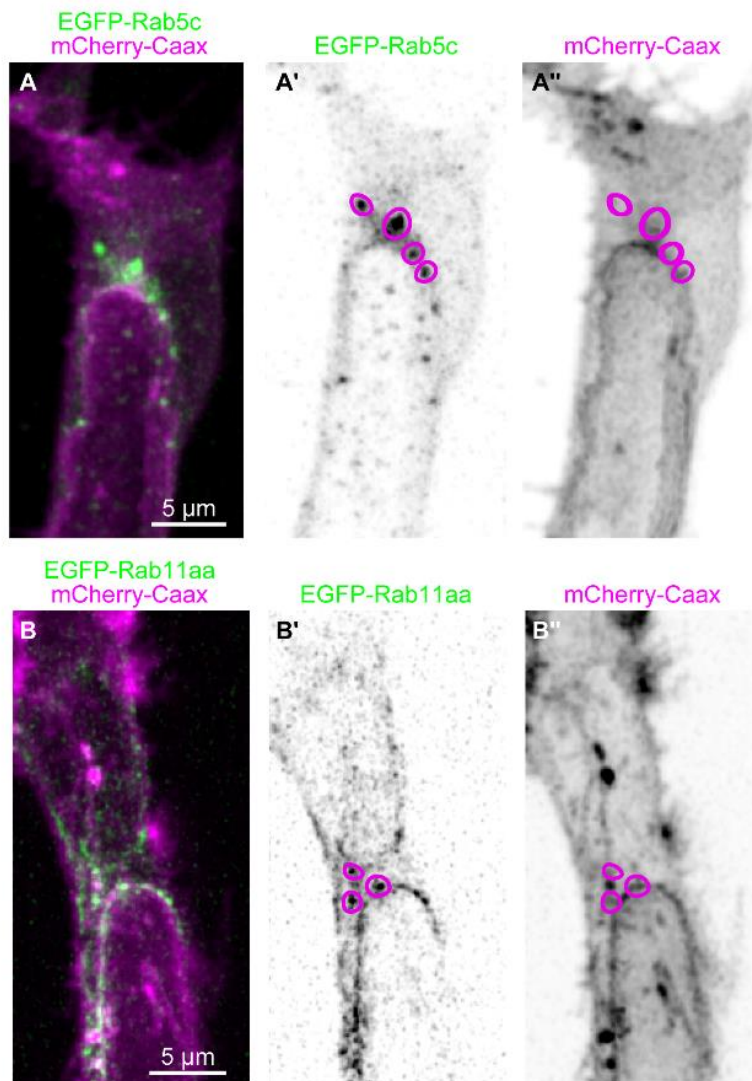
#### 4.1.5.13 Assembly of phylogenetic tree

To assemble a phylogenetic tree of the *rab7* genes, protein sequences were assembled from ensemble genome browser (<https://www.ensembl.org/>). The sequences were then listed in a txt file which was uploaded to [www.ebi.ac.uk](http://www.ebi.ac.uk) (Madeira et al., 2019). Tree data was then visualized using the phylo.io tool (<http://phylo.io>) (Robinson et al., 2016). For the species comparison, amino acids of the following genes were used: *Homo sapiens* (human): *rab7A*: ENSG00000075785, *rab7B*: ENSG00000276600; *Mus musculus* (mouse): *rab7a*: ENSMUSG00000079477, *rab7b*: ENSMUSG00000052688; *Drosophila melanogaster* (fruit fly): *rab7*: FBgn0015795; *Danio rerio* (zebrafish): *rab7a*: ENSDARG00000020497, *rab7b*: ENSDARG00000021287, *zgc:100918*: ENSDARG00000087243; *Cyprinus carpio* (common carp): *rab7a*: ENSCCRG00000027229, *rab7b*: ENSCCRG00000044991, *zgc:100918*: ENSCCRG00000016691; *Sinocyclocheilus graham* (golden line barbel): *rab7a*: ENSSGRG00000034717, *rab7b*: ENSSGRG00000031796, *zgc:100918*: ENSSGRG00000020044; *Carassius auratus* (Goldfish): *rab7a*: ENSCARG00000008208, *rab7b*: ENSCARG00000017207, *zgc:100918*: ENSCARG00000004993.

#### 4.1.5.14 Transcriptomics data analysis

Transcriptomics data were analysed from two available databases. The Lawson and Li dataset (Lawson et al., 2020) presents transcriptomics data regarding endothelial-specific expression of genes. Developmental stage-specific transcriptomics data was analysed by a currently unpublished RNA-seq dataset which was made publicly available <https://www.ebi.ac.uk/gxa/experiments/E-ERAD-475> (thanks to the Busch-Nentwich lab). Data were analysed from both datasets for our genes of interest and visualized using GraphPad Prism.

#### 4.1.6 Supplementary Data



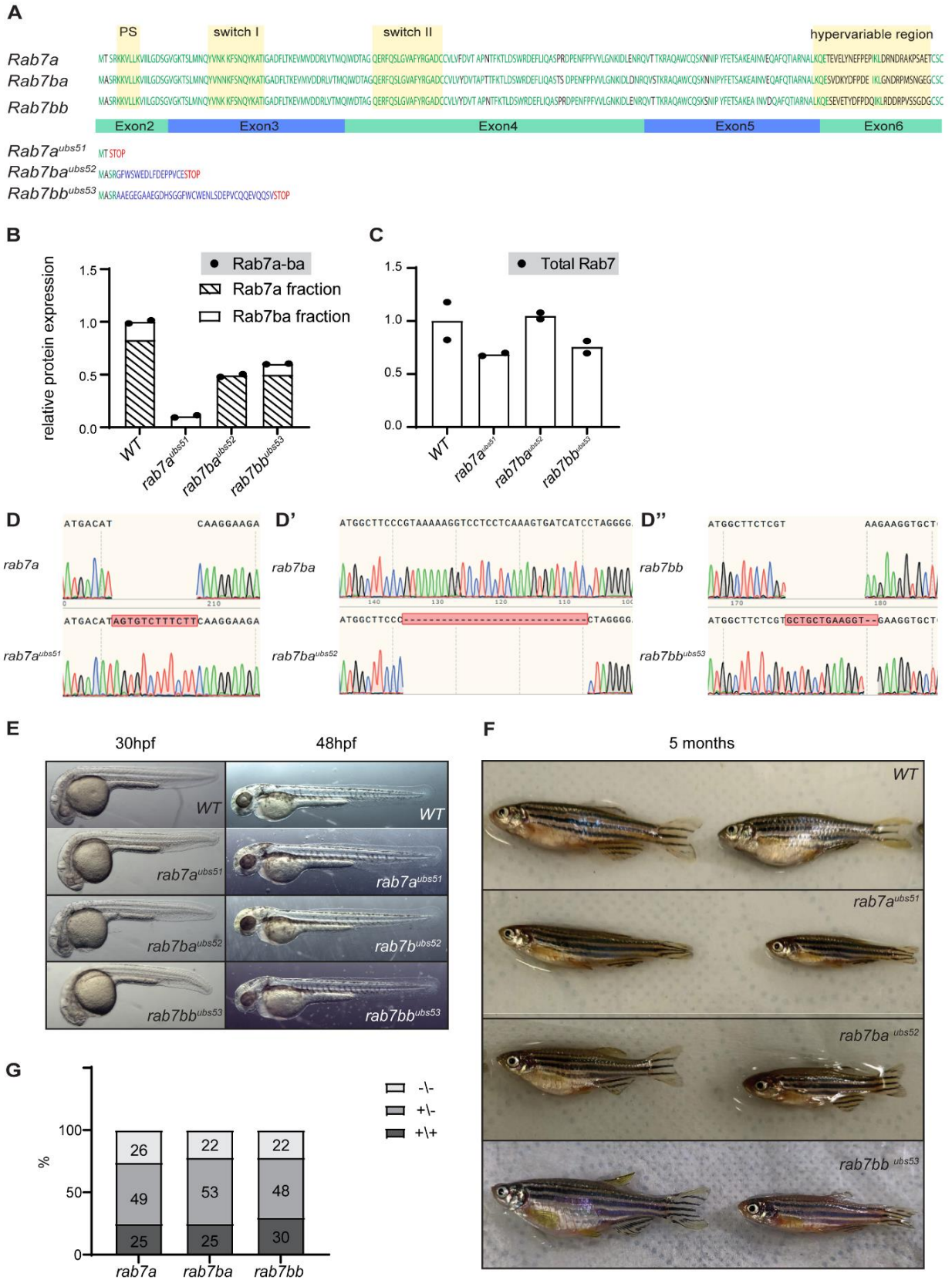
←Figure 17 Rab5c and Rab11a localization in endothelial cells. Related to Figure10

A Confocal images of a tip cell from a 32hpf transgenic *Tg(kdrl:mCherry-CAAX)<sup>S916</sup>* embryo injected with the plasmid *fli:EGFP-Rab5c* (marker of early endosome). The Rab5c signal (EGFP) does not co-localise with CAAX at dots, but Rab5c dots are found close to the apical surface of the expanding lumen. A' Inverted contrast of eGFP-Rab5c from A shows Rab5c dots (pink circles). Note that these regions do overlap with the CAAX signal (A''). A'' Inverted contrast of mCherry-CAAX from A. B Confocal images of a tip cell from a 32hpf transgenic *Tg(kdrl:mCherry-CAAX)<sup>S916</sup>* embryo injected with the plasmid *fli:EGFP-Rab11a* (marker of recycling endosome). The Rab11a signal (EGFP) does not co-localise with CAAX at dots, but Rab11a dots are found in proximity to the apical surface and is also found along the apical membrane of the expanding lumen. A' Inverted contrast of EGFP-Rab11a from B shows Rab11a dots (pink circles). Note that these regions overlap with CAAX signal (B''). B'' Inverted contrast of mCherry-CAAX from B.

→Figure 18 Characterisation of development and survival rates of *rab7* mutants. Related to Figure11.

A All three *rab7* protein sequences and their predicted mutant sequence. Yellow boxes indicate an important prenylation site responsible for mediating post-translational prenylation of the C-terminal XCXC motif and membrane insertion, and the switch domains important for effector binding after GTP-activation and the hypervariable region responsible for proper membrane recognition. Green letters represent aa that are identical in all three Rab7 isoforms, while black letters represent different aa in Rab7 isoforms. In mutant protein sequences, blue letters are aa encoded out of frame and STOP marks the premature terminating codon. B-C Individual value scatter plots of relative protein expression of Rab7ba and the total Rab7 amount. Levels were measured in two different pooled samples of wild-type, *rab7a mat-zyg*, *rab7ba mat-zyg* and *rab7bb mat-zyg* homozygous embryos. Values were then normalized to total amount of protein measured per sample and to the amount of wild-type sample (n= 2 pools of 20 embryos). D-D'' Sequencing results of PCR products of the respective *rab7* loci from 3 months old homozygous fish. E Brightfield images of wild-type, *rab7a*, *rab7ba* and *rab7bb* homozygous mutant embryos at 30 hpf and 48 hpf. F Images of wild-type, *rab7a*, *rab7ba* and *rab7bb* adult fish at 5 months. G Percentage of *rab7a*, *rab7ba* and *rab7bb* mutations found in adult fish from a heterozygous incross of the respective mutant (*rab7a*: N= 3 independent experiments, n= 100 fish; *rab7ba*: N= 3, n= 100; *rab7bb* N= 2, n= 70).





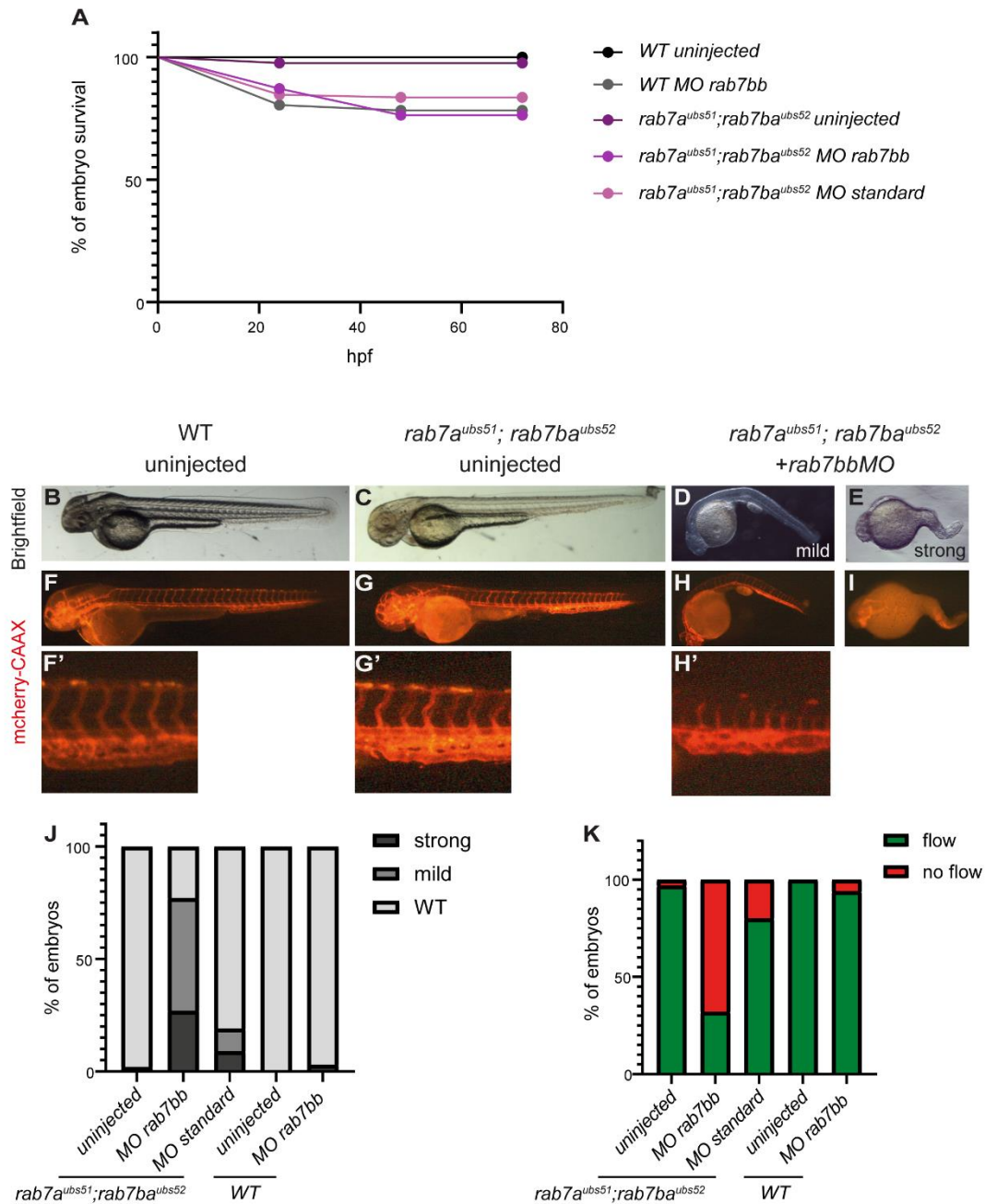


**Figure 19** Characterization of development and survival rate of the triple *rab7* loss-of-function mutants. Related to Figure 12 and 13.

**A** Percentage of surviving embryos from wild-type, wild-type injected with morpholino against *rab7bb* and *rab7a*; *rab7ba* mutant increases uninjected or injected with control morpholino or *rab7bb* morpholino (n=43-183 embryos per condition). **B-E** Embryo morphology **F-I** and vascular development at 48 hpf of wild-type, double mutant and double mutant injected with the *rab7bb* morpholino (triple loss-of function). **F'-H'** Zoom-in of the boxes in **F-H**. **J** Developmental defects shown as % of embryos injected with morpholino or uninjected in double mutant or wildtype background (n=42-105 embryos per condition). **K** Presence of blood flow shown as % of embryos injected with morpholino or uninjected in double mutant or wildtype background (n=42-105 embryos per condition).

## 5 Results: Chapter II

### 5.1 Generation and preliminary screening of *unc13d* mutants

### 5.1.1 Generation of *unc13d* mutants

During tracheal development in *D. melanogaster*, the formation of a lumen across the different metamers requires the fusion of two apical membrane patches in each of the two fusion cells. In the mutant for the *D. melanogaster* gene *staccato* (*stac*), these apical membrane patches do grow to the final site of fusion but actually fail fuse. It has been shown that while Stac protein is rather dispersed throughout the cytoplasm in most tracheal cells, Stac localization in tracheal fusion cells changes to localized punctae. These punctae represent lysosome-related organelles (LROs) since they colocalize with Rab27a, Rab7 and Lamp1. Luschnig and colleagues propose in their model that these LROs are formed especially in fusion cells before lumen contact and that they mediate fusion of the two neighbouring apical membranes upon a calcium trigger.

Similar to *D. melanogaster*, the zebrafish genome has four different genes encoding Unc13 family members: *unc13A*, *unc13b*, *unc13ba* and *unc13d*. Of these four genes, *unc13d* shows the highest level of sequence similarity to *stac* (88% of the sequence aligns with 24% identity for *unc13d*, only 40% of the sequence for *unc13A* and less than 16% for *unc13B* and *unc13ba* align to 24% or less). Among each other, these four genes do not share sequence identity higher than 30%, despite a query coverage of >80%. There is another zebrafish gene with similarity to *stac* called *baiap3*, which shows even stronger similarity than *unc13d* (26% identity), but is expressed mostly in the head, while *unc13d* is strongly expressed in endothelial cells (Table 1) (Fig 20A). Therefore, the latter represents the best candidate to function as the *stac* homologue in the zebrafish vasculature.

Table 1 Zebrafish *unc13* genes and their sequence similarity to *D. melanogaster stac*.

Gene name	Query coverage	Identity of the aligned sequence to <i>stac</i>
<i>unc13d</i>	89%	23.99%
<i>unc13A</i>	39%	24.32%
<i>unc13B</i>	14%	24.85%
<i>unc13ba</i>	17%	23.65%
<i>baiap3</i>	89%	25.68%

In (Caviglia, Brankatschk et al. 2016), Luschnig and colleagues showed that the *stac* gene in *D. melanogaster* encodes three isoforms from three different transcription start sites. A P-element insertion in the first coding exon of the longest transcript showed a stronger phenotype compared to the mutant they used in the experiments of the paper. They chose the other mutant however, because the mutation lies in the second to last exon of the gene and therefore targets all three transcripts. In zebrafish, only one transcript has been described so far. The zebrafish protein spans

across 35 exons with the first exon being untranslated (Fig 20B). We designed gRNAs that lie in the coding region of the first translated exon. Mutants might thus be induced at a similar position to the mutation in *D. melanogaster* showing the strongest phenotype.

Using the CRISPR/Cas9 system an *unc13d* mutant allele was generated that contains a 19bp deletion in the coding region of exon2 (Fig 20B). The mutation efficiency was at least 20% (8 positive pools of 5 embryos out of 8 pools) in injected embryos and germ line transmission efficiency of G0 adults was 60% (6/10). The identified allele leads to an out of frame protein and a premature stop codon in exon 4 of the gene. All the important Ca<sup>2+</sup> binding domains and Munc homology domains (MHD) are lost in this truncated version of the protein (Fig 20C).

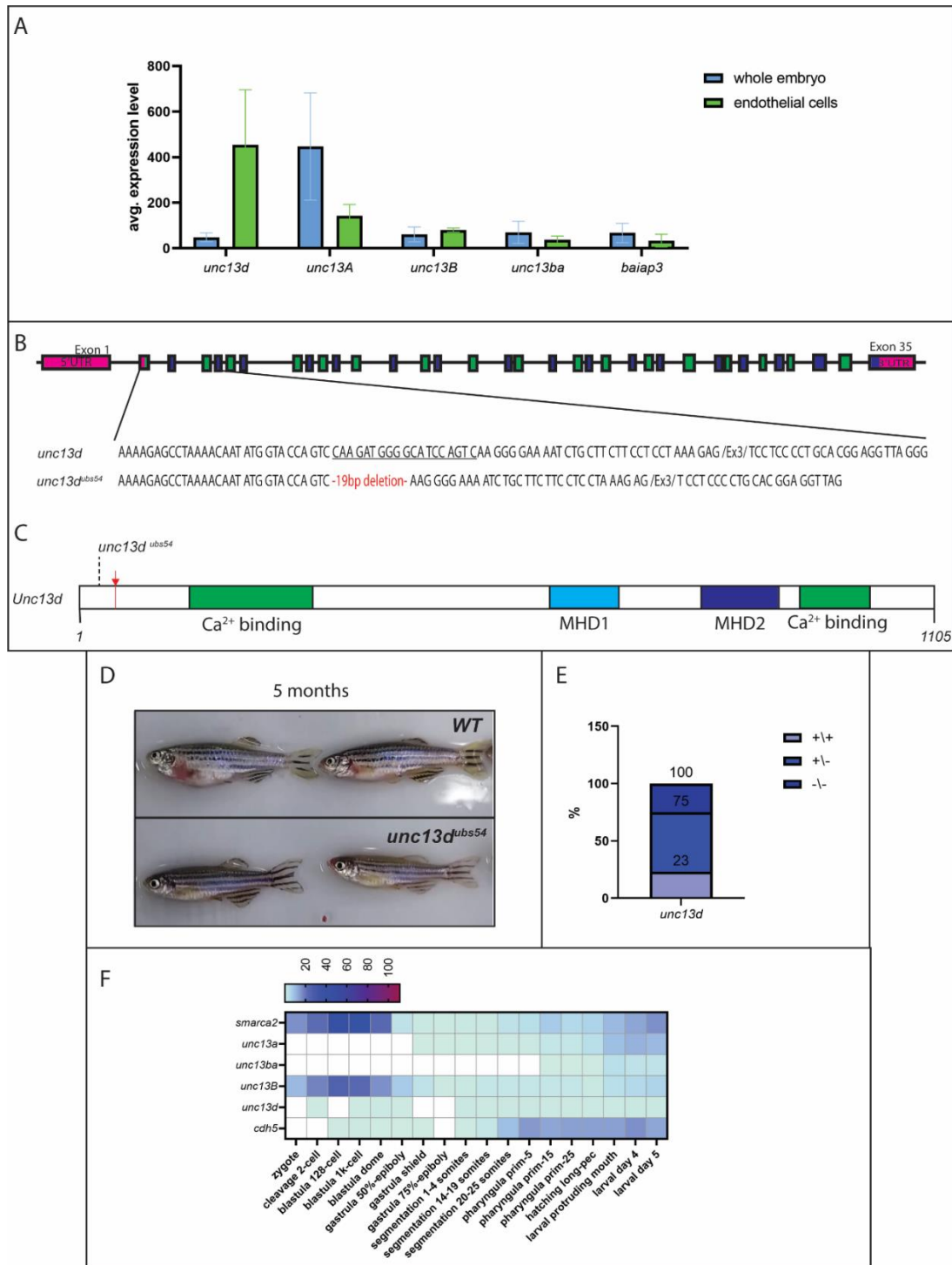


**Figure 20** Expression and characterization of the *unc13d* wildtype and mutant allele in zebrafish

**A** Representation of the transcriptomics data in the database published in (Lawson, Li et al. 2020). Expression levels of *unc13d*, *unc13A*, *unc13B*, *unc13ba* and *baiap3* in cells positive for *kdr1:EGFP* (endothelial cells, green) and *kdr1:EGFP* negative cell (all embryonic cells but endothelial cells, blue). **B** Schematic representation of the gene structure of *unc13d* in zebrafish. UTR is highlighted in pink, alternating coding exons are represented in green and blue. Sequence of the exons 2 and 4 of *unc13d*. Deleted basepairs are underlined in the wild-type sequence. Codon triplets are separated by spaces. Underneath is the sequence of the allele *ubs54*. Deletion is shown in red. **C** Schematic representation of Unc13d. In green are the two calcium binding domains and in blue the two munc-homology domains (MHD). Dashed line indicates place of *unc13d<sup>ubs54</sup>* mutation and red arrow indicates the introduced premature stop codon **D** Images of wild-type and *unc13d* adult fish at the age of 5 months. **E** Distribution of *unc13d* mutations in adults from a heterozygous incross. N= 1 clutch, n= 40 fish. **F** Heat map of expression of *unc13* genes, a known maternally contributed gene *smarca2* and an endothelial specific gene *cdh5*, during zebrafish development. Data extracted from EMBL expression atlas (see Material and Methods).

### 5.1.2 Analysis of survival and vascular development of *unc13d* mutants

Some mutations in the *stac* gene in *D. melanogaster* have been shown to be partially lethal. But the *isolatd* allele for *unc13d* in zebrafish shows no decrease in survival. Heterozygous incrosses show normal mendelian distribution and *unc13d* homozygous fish reach adulthood (Fig 20 D-E). Transcriptomics data shows no maternal contribution of *unc13d* and in fact embryos from homozygous incrosses survive to adulthood (Fig 20 F).

To study whether *unc13d* plays a similarly strong role in lumen fusion during anastomosis, we imaged *Tg(kdrl:mcherry-CAAX)* embryos labelling the apical membrane. In tracheal anastomosis in *D. melanogaster* lumen can still be established in each segment and growing of the two luminal fronts is unaltered. The *stac* phenotype can only be observed in the final step, which is lumen fusion. If *unc13d* in the vasculature plays an identical role, the two luminal fronts will still form and invaginate towards each other but being incapable of fusing and forming a continuous lumen. Lumenization of the entire vasculature could still be possible in case it is established via cord hollowing. To analyse lumenization during vascular development in zebrafish embryos, transgenic *Tg(kdrl:mcherr-CAAX)* embryos were imaged. In *uncd13* homozygous embryos all recorded ISVs were lumenized at 48hpf (Fig 21 B). During anastomosis lumen can be invaginating from the DA and progress through the ISV and form a fully inflated lumen at 48 hpf. To image transcellular lumen formation and lumen fusion, higher magnification (63X) confocal imaging was used. In these images two apical luminal fronts can be seen growing towards each other and when coming into close enough proximity fuse to form one continuous lumen. This process could be observed in *unc13d* heterozygous and homozygous mutant embryos (Fig 21 C-E). Therefore, we can conclude that *unc13d*, by itself, does not fulfil the same crucial role in apical lumen fusion in zebrafish vascular anastomosis, as it does in tracheal anastomosis in *D. melanogaster*.

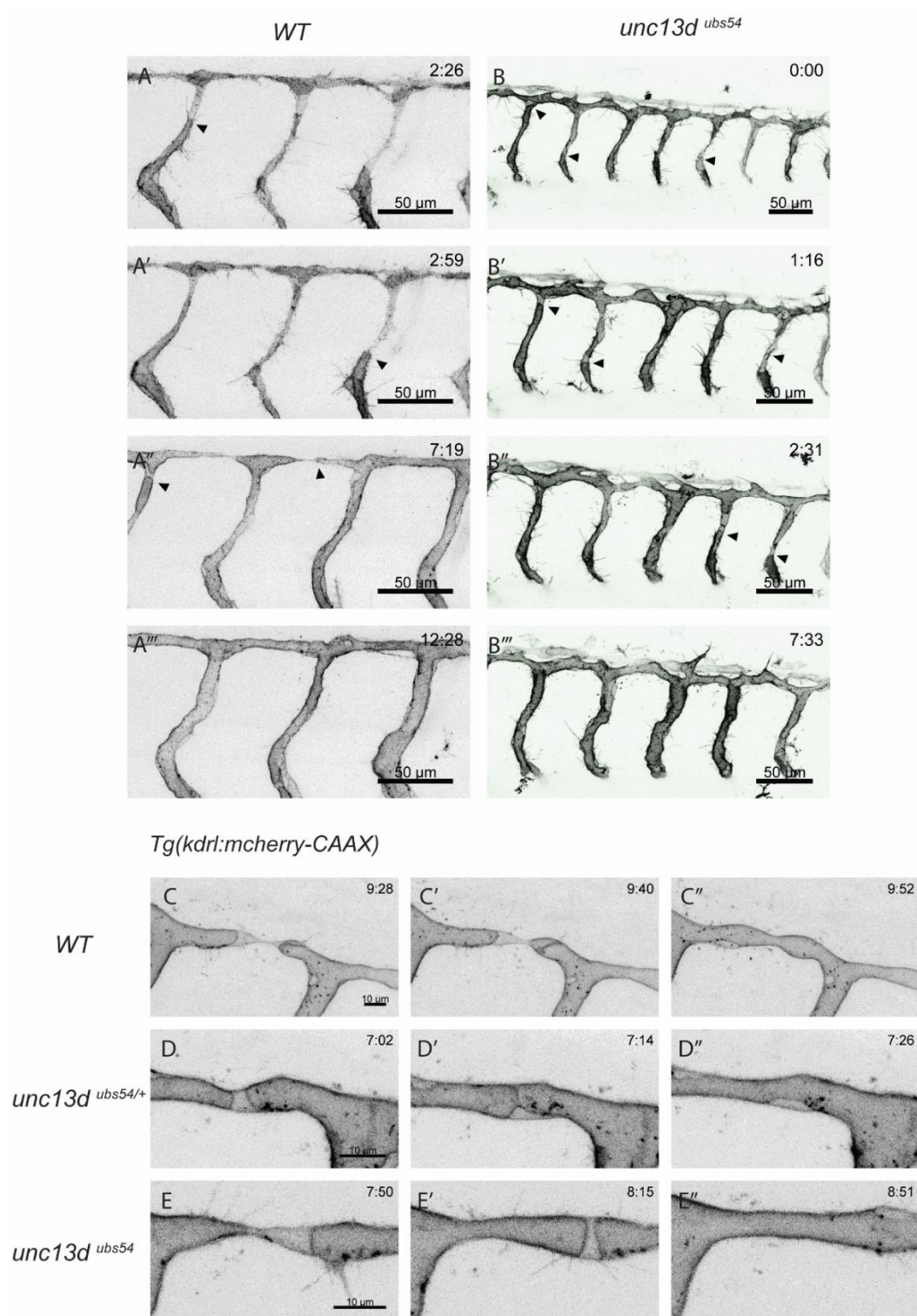


**Figure 21** Transcellular lumen fusion in the *unc13d* mutant

**A-B** Confocal still pictures from time-lapse movies (from 34-48 hpf) showing lateral views (anterior to the left) of ISV lumenization in transgenic *Tg(kdrl:EGFP-CAAX)* embryos. Wild-type embryos and embryos maternal zygotic homozygous mutant for *unc13d*. Black arrowheads show invaginating luminal front. The final image represents the fully lumenized state of the ISVs around 46-48 hpf. **C-E** Still images from high resolution confocal imaging showing lumen fusion in the DLAV of transgenic *Tg(kdrl:mcherry-CAAX)* embryos. Images show two luminal fronts growing and eventually fusing in wild-type, *unc13* heterozygous and *unc13d* homozygous embryos.



## 6 Material and Methods

### 6.1 Materials

#### 6.1.1 Buffer, Media and Solutions

Table 2 Buffers, media and solutions

<b>Solutions</b>	<b>Composition</b>
Alkaline lysis buffer	100mM Tris HCl pH 9.5 50mM MgCl <sub>2</sub> 100mM NaCl 0.1% Tween-20
DNA loading buffer (10x)	30% (v/v) glycerol 20% (w/v) Orange G in ddH <sub>2</sub> O
Methylene blue solution	1% Methylene Blue (Sigma) ddH <sub>2</sub> O
E3 (50x)	250mM NaCl 8.5mM CaCl <sub>2</sub> 16.5mM MgSO <sub>4</sub> Adjusted to pH7.0-7.4
egg water (methylene blue + E3)	1:2000 Methylene blue solution (0.0005%) 1x E3
LB	1% (w/v) tryptone 0.5% (w/v) yeast extract 1% (w/v) NaCl ddH <sub>2</sub> O (autoclaved)
LB w/o salt	1% (w/v) tryptone 0.5% (w/v) yeast extract ddH <sub>2</sub> O (autoclaved)

Tricaine (25x)	0.4% (w/v) Tricaine ddH <sub>2</sub> O adjusted to pH7.0
Mounting agarose	0.7% low melting agarose in E3 1x PTU 1x Tricaine
Protease from <i>Streptomyces griseus</i> (Pronase)	SIGMA
Magic medium	Fischer Scientific
Wash Buffer	20mM Tris; 30mM Imidazole; 500mM NaCl; adjusted to pH 8
Elution Buffer	20mM Tris 500mM Imidazole 500mM NaCl adjusted to pH 8
Dialysis Buffer	20mM Tris 200mM KCl 10mM MgCl <sub>2</sub> adjusted to pH 8
10X SDS-PAGE running buffer	30g Tris 144g Glycine 10g SDS pellets Up to 1l ddH <sub>2</sub> O
Coomassie staining solution	450ml Methanol 450ml ddH <sub>2</sub> O 100ml Glacial acetic acid 1g Coomassie R-250
Coomassie destaining solution	450ml Methanol 550ml ddH <sub>2</sub> O 10ml Glacial acetic acid

5X SDS loading buffer	1 g SDS pellets 200mM Tris/HCl pH 6.8 0.05g Bromophenol blue 2.5ml Glycerol (pure) H <sub>2</sub> O up to 10ml
Lysis Buffer	5% SDS 10mM TCEP 100mM TEAB in ddH <sub>2</sub> O
S-Trap Buffer	90% Methanol 100mM TEAB adjusted to pH 7.1
Digestion Buffer	50mM TEAB in ddH <sub>2</sub> O adjusted to pH 8

### 6.1.2 Antibiotics & Bacteria

Table 3 Antibiotics

Antibiotic	Stock concentration	Working concentration
Ampicilin	100mg/ml	100µg/ml
Kanamycin	50mg/ml	50µg/ml

Table 4 Bacterial strains

Strain	Supplier
<i>Top10</i>	Invitrogen
<i>E. Coli Rosetta</i>	SIGMA

### 6.1.3 Basic Material

#### 6.1.3.1 Pipettes and tips

Table 5 Pipettes and pipette tips

Material	Manufacturer
Pipetman 2µl, 20µl, 200µl and 1000µl	Gilson
2µl tips	Treff Lab
20µl-200µl tips	Greiner bio-one
1000µl tips	Greiner bio-one

#### 6.1.3.2 Tubes and columns

Table 6 Tubes and columns

Material	Manufacturer
1.5ml fast lock tubes	Sarstedt
2ml fast lock tubes	Sarstedt
5ml fast lock tubes	Eppendorf
15ml safe lock tubes	Falcon
50ml safe lock tubes	Falcon
DNA-binding column	Macherey-Nagel
S-Trap micro column	Protifi

#### 6.1.3.3 Machines

Table 7 Machines

Machine	Manufacturer
NanoDrop	Thermo Fischer Scientific
Centrifuge 5424	Eppendorf
Centrifuge 5417R	Eppendorf
Centrifuge 5804R	Eppendorf
Centrifuge RC 5C plus with rotors SLA3000 and SS34	Sorvall
Sonicator Sonifier 250	Branson
T3000 Thermocycler	Biometra
T1 Thermocycler	Biometra
Bioruptor	Diagenode

### 6.1.3.4 Software

Table 8 Software

<b>Software</b>	<b>Developer</b>
ApE A plasmid editor	Freeware
SnapGene	SnapGene
Fiji	Freeware
Omero	Open source network
Graphpad Prism	Graphpad
Filemaker Pro	Claris International
Illustrator	Adobe

### 6.1.4 Injection & Mounting Material

Table 9 Material for injection and mounting

<b>Material</b>	<b>Manufacturer</b>
Pipette pump, pipettor, 10ML	Bel-Art H-B Instrument SP Scienceware
Glass bottom Microwell dishes P35G-1.5-10-C	MatTek
Injector PV820 WDI	World Precision instruments
Petri Dish, 94x16 heavy version	Greiner Bio-One
Borosilicate glass needles (1mm outer diameter, 0.5mm inner diameter, 10cm length)	Sutter Instruments
Flaming/Brown micropipette puller Model -P97	Sutter Instruments
Molds	Custom made by the Biozentrum Workshop

### 6.1.5 Fish lines

Table 10 Fishlines

Genotype	Allele Designation	Description	Reference
<i>rab7a</i> <sup>ubs51</sup>	ubs51	mutant	This study
<i>rab7ba</i> <sup>ubs52</sup>	ubs52	mutant	This study
<i>rab7bb</i> <sup>ubs53</sup>	ubs53	mutant	This study
<i>unc13d</i> <sup>ubs54</sup>	ubs54	mutant	This study
<i>Tg(kdrl:EGFP-hrasCAAX)</i>	ubs48	transgene	Etienne Schmelzer 2019
<i>Tg(kdrl:mCherry-CAAX)</i> <sup>S916</sup>	S916	transgene	(Hogan, Herpers et al. 2009)
<i>Tg(fli1a:EGFP-Rab9b)</i>	ubs46	transgene	Etienne Schmelzer 2019
<i>TgBAC(lamp2: LAMP2-RFP)</i> <sup>pd1117</sup>	pd1117	BAC-transgene	(Rodríguez-Fraticelli, Bagwell et al. 2015)
<i>Tg(fli:PECAM-GFP)</i> <sup>ncv27Tg</sup>	ncv27Tg	transgene	Ando et al 2016 (Ando, Fukuhara et al. 2016)

### 6.1.6 Plasmids

Table 6 contains a complete list of plasmids generated or acquired during the thesis. All plasmids were purified by NucleoSpin® Plasmid purification kit (Machery-Nagel) or NucleoBond® Xtra Midi Plus Plasmid purification kit (Machery-Nagel), with >150ng/μl.

Table 11 List of plasmids used and generated

Plasmid	Comments	Labels
fli-mKate2-Rab5c	endothelial specific mKate2-Rab5c fusion protein	early endosomes
fli-mKate2-Rab7a	endothelial specific mKate2-Rab7a fusion protein	late endosomes
fli-EGFP-Rab32a	endothelial specific EGFP-Rab32a fusion protein	lysosomes
fli-EGFP-Rab32b	endothelial specific EGFP-Rab32b fusion protein	lysosomes
fli-EGFP-Rab38	endothelial specific EGFP-Rab38 fusion protein	lysosomes
kdrl-irfp670-CAAX	endothelial specific iRFP670-CAAX fusion protein	apical membrane

## 6.1.7 Primers

Table 12 Primers for genotyping, gRNA synthesis and RT-PCR

Name	Sequence	Used in
rab7a fwd	GGG AAG TCT GTG TGT TTA ACA GAA GCC GG	Genotyping PCR
rab7a rev	CCA CGC CCC TCT TAC TGT TAG TTT GC	Genotyping PCR
rab7a mut rev	GAC ATA GTG TCT TTC TTC AAG G	Genotyping PCR
rab7a wt fwd	CAG AAG AAC TTT CTT CCT TGA TGT C	Genotyping PCR
rab7b fwd	GTG TAA ACA GCC ACA AGC C	Genotyping PCR
rab7b rev	CAC ACT GAT AGC GTC TAT GC	Genotyping PCR
rab7b wt fwd	CCT CCT CAA AGT GAT CAT CCT AGG	Genotyping PCR
rab7b mut rev	CCA GAA TCC CCT AGG GGA AGC C	Genotyping PCR
rab7l fwd	GTT AGA CCC GAA CTG CAT TTC G	Genotyping PCR
rab7l rev	GAA ACC CAC ATG AAC ACG G	Genotyping PCR
rab7l mut rev	GGC TTC TCG TGC TGC TGA AGG	Genotyping PCR
rab7l wt fwd	GCA GCA CCT TCT TAC GAG AAG C	Genotyping PCR
Beta actin fwd	CCA CGA GAC CAC CTT CAA CT	RT-qPCR
Beta actin rev	CTT CTG CAT CCT GTC AGC AA	RT-qPCR
rab7a fwd Exon1	CAT CAG GCT CGT GTA AGG G	RT-qPCR
rab7a fwd Exon2	GGA AGA AAG TTC TTC TGA AGG	RT-qPCR
rab7a rev Exon3	GTG ACA AGC CGG TCG TCA ACC	RT-qPCR
rab7b fwd Exon1	GAT TCG GAC AGC TGC GAC GG	RT-qPCR
rab7b fwd Exon2	CCT CAA AGT GAT CAT CCT AGG	RT-qPCR
rab7b rev Exon3	GAA AGT CTG CAC CAA TGG TGG	RT-qPCR
rab7l fwd Exon1	GGA ATT TGT TGA GCC GAA GCC GG	RT-qPCR
rab7l fwd Exon2	GCT GAA GGT GAT CAT TCT GG	RT-qPCR
rab7l rev Exon3	GAA AGT CTG CGC CGA TGG TGG	RT-qPCR
Rab7a_tar3	TAATACGACTCACTATAGG <b>GCTCTGACACTATGA</b> <b>CATCA</b> GTTTTAGAGCTAGAAATAGCAAG	gRNA synthesis
Rab7b_tar2	TAATACGACTCACTATAGG <b>TTTGAGGAGGACCTT</b> <b>TTTAC</b> GTTTTAGAGCTAGAAATAGCAAG	gRNA synthesis
Rab7l_tar1	TAATACGACTCACTATAGG <b>AAGGATGGCTTCTCG</b> <b>TAAGA</b> GTTTTAGAGCTAGAAATAGCAAG	gRNA synthesis
Constant_oligo	AAAAGCACCGACTCGGTGCCACTTTTTCAAGTTGATAACGG ACTAGCCTTATTTAACTTGCTATTCTAGCTCTAAAC	gRNA synthesis

### 6.1.8 Morpholinos

Table 13 Morpholinos

Name	Sequence	inhibits splicing of
Rab7a E2I2	GTTGATTGCGAGAACTCACCCGGA	<i>rab7a</i> exon2
Rab7a I1E2	CAGAGCTGAAGGAAGAGGAAGCACA	<i>rab7a</i> exon2
Rab7b E2I2	ATGCTGAACAAAACACTTACCCAGA	<i>rab7ba</i> exon2
Rab7b I1E2	AGGACACTGCTAAGAAGAAAAGGAT	<i>rab7ba</i> exon2
Rab7c E2I2	AAAGCCATCACTTACCCAGAATCCC	<i>rab7bb</i> exon2
Rab7c I1E2	ACTGTGCCTGAAAGAATACAAGTAT	<i>rab7bb</i> exon2
Standard control MO	CCTCTTACCTCAGTTACAATTTATA	

### 6.1.9 Reference Peptides for MS

Table 14 Reference peptides for targeted mass spectrometry

Sequence	Targeted <i>rab7</i>	Detection in wild-type	Used for analysis
VIIIGDSGVGK	pan-rab7	++	Yes
ATIGADFLTK	pan-rab7	+	Yes
LVTMQIWDTAGQER	pan-rab7	+	No
DEFLIQASPR	rab7a-bb	-	No
NNIPYFETSAK	rab7a-ba	++	Yes
EAINVEQAFQTIAR	rab7a-ba	++	No
GADCCVLVFDVTAPNTFK	rab7a	(+)	Yes
QETEVLYNEFPEPIK	rab7a	-	No
GADCCVLVYDVTAPNTFK	rab7ba	(-)	Yes
DEFLIQASTDPENFPFVVLGNK	rab7ba		No
YDFPDEIK	rab7ba	-	No
LGNDRPMSNGEGCSCMASPR	rab7ba		No
GADCCVLVYDVTAPNTFK	rab7bb	(+)	Yes
SNIPYFETSAK	rab7bb	++	Yes
EAINVDQAFQTIAR	rab7bb	++	No
QESEVETYDFPDQIK	rab7bb	-	No
DDRPVSSGDGCSCMASR	rab7bb		No



## 6.1.10 Microscopes and binoculars

Table 15 Microscopes and binoculars

Microscope	Manufacturer	Information	Objectives	NA
Binocular Stemi SV 11	Zeiss	binocular		
M205 FA stereo binocular	Leica	fluorescence binocular		
SP5-II-Matrix	Leica	Point Scanning Confocal Microscopes	HC PL Fluotar 10x (air)	0.3
			HCX IRAPO L 25x (water)	0.95
			HCX PLAN APO CS 40x (water)	1.1
SpinSR (CSU-W1)	Olympus	Spinning disk confocal microscope	UPL X APO 4x (air)	0.16
			UPL X APO 10x (air)	0.4
			UPL S APO 30x (silicone)	1.05
			UPL APO 60x (water)	1.2
			UPL APO 60x (oil)	1.5
			UPL APO 100x (oil)	1.5
SpinD (CSU-W1)	Olympus	Spinning disk confocal microscope	UPL X APO 4x (air)	0.16
			UPL X APO 10x (air)	0.4
			UPL S APO 30x (silicone)	1.05
			UPL APO 60x (oil)	1.5
			UPL APO 100x (oil)	1.5

## 6.2 Methods

### 6.2.1 Molecular biology protocols

#### 6.2.1.1 gRNA synthesis

DNA oligonucleotides encoding gRNAs with invariant adapter sequence were used for each *rab7* gene. For gRNA synthesis each of the gene specific primers was mixed with the constant oligonucleotide, containing a complementary adapter and a Cas9 recruiting sequence: both 10  $\mu$ M, and a double-stranded product was Phusion High fidelity Polymerase (Thermosfisher). The resulting DNA was purified by Gel and PCR clean-up Kit (Macherey Nagel). 0.2  $\mu$ g of DNA was used for RNA in vitro transcription by T7 Megascript Kit (Ambion) according to the manufacturer's protocol gRNA was purified via ethanol purification and concentration was determined using Nanodrop (DeNovix)

#### 6.2.1.2 Cas9 protein production

Addgene plasmid pET-28b-Cas9-His ((*Gagnon, Valen et al. 2014*)). The protein was expressed in BL21 Rosetta Escherichia coli strain (Novagen) in magic medium at 37 °C for 12 h followed by 24 h at 18 °C. Cells were harvested by centrifugation at 6000rpm for 15 min and stored at 4 °C.

The cell pellet was resuspended in 20 mM Tris-HCl buffer (pH 8) containing, 0.5 M NaCl, 30 mM imidazole, then ultrasonicated and centrifugated at 140000 rpm at 4 °C for 15 min. The supernatant was loaded on Protino NI-NTA agarose beads equilibrated by the same buffer and incubated for 60min. After 4x wash protein was eluded with 20mM Tris-HCl buffer (pH 8), containing 0.5 M Imidazole and 0.5 M on a column in 1ml stepwise elution. Protein purity was confirmed by SDS-polyacrylamide gel electrophoresis and dialyzed overnight against 20 mM Tris-HCl buffer (pH 8) containing 200 mM KCl and 10mM MgCl<sub>2</sub> and stored at -80 °C.

#### 6.2.1.3 Electrocompetent cells

LB without salt was inoculated with Top10 (Invitrogen) bacteria. The culture was incubated overnight at 37°C and shook at 200rpm. In the morning the culture was diluted 1:100 in 1L of LB without salt and further incubated at 37°C at 200rpm in two 3LErlenmeyer flasks until the optical density OD<sub>600</sub> of the culture reached 0.6-0.8 (around 3-4 hours). The flasks were cooled down in an ice slurry and pelleted in a precooled (4°C) centrifuge at 3300 rpm for 10 minutes. The pellet was resuspended in 5ml 10% sterile and cooled glycerol. The suspension was further redistributed to 2ml Eppendorf tubes and pelleted at 8000 rpm for 5min in a cooled benchtop centrifuge. The pellet was resuspended in 1ml 10% glycerol and 50 $\mu$ l aliquots were made. The aliquots were frozen in liquid nitrogen and stored at -80°C.

#### 6.2.1.4 Transformation of electrocompetent cells

Construct was dialysed nitrocellulose membrane (MF™ Membrane Filters, type 0.025µm VSWP). 1-2µl of Construct or Plasmid was mixed with electrocompetent cells and loaded into a Gene Pulser/Micro Pulser 1mm Cuvette (Bio-Rad). The bacteria were electroporated at 1.8kV with a MicroPulser(Bio-Rad). Transformed bacteria were immediately resuspended in LB containing no antibiotics and incubated for one hour at 37°C with 200rpm. Bacteria were plated on LB plates with the appropriate antibiotics and incubated overnight at 37°C.

#### 6.2.1.5 Plasmid purification

##### 6.2.1.5.1 Cloning – Midi Preps

For cloning, plasmids were retransformed, single colonies were picked and used to inoculate 100ml of LB containing the appropriate antibiotic and incubated overnight at 37°C with 200rpm. The Plasmids were purified using NucleoBond® Xtra Midi Plus Plasmid purification kit (Machery-Nagel).

##### 6.2.1.5.2 Zebrafish embryo injections – Midi Preps EF

Plasmids, destined to be injected directly into one-cell staged eggs, were purified with NucleoBond® Xtra Midi Plus EF plasmid purification kit (Machery-Nagel).

#### 6.2.1.6 Sequencing

PCR reaction were purified either after gel extraction or directly, by using NucleoSpin® Gel and PCR Clean-up (Macherey-Nagel) – prior to sequencing. The sequencing was performed by Microsynth, Switzerland using the Economy Bar Service. The reactions were assembled according to the guidelines of Microsynth (<https://srvweb.microsynth.ch/>)

#### 6.2.1.7 Cloning

All constructs were cloned using the Multisite Gateway® Three-Fragment Vector Construction Kit. It allows simultaneous cloning of multiple DNA fragments in a defined order and orientation. It is based on the site-specific recombination system of the bacteriophage lambda. The modular construction system of the Multisite Gateway® System facilitates a rapid and highly efficient assembly of diverse expression clones.

#### 6.2.1.8 LR-reaction

The LR recombination reaction allows to clone multiple entry clones (attL4-5'-Promoter – attR1 + attL1-Fluorophor or gene of interest -attL2 + attR2-3' gene of interest or polyadenylation-attL3) into a destination Vector pDEST™ R4-R3 Vector II. A schematic of the LR cloning is shown in Figure 8.

In order to generate an expression clone, multiple entry clones are mixed with the destination vector. The modular construction system of the MultiSite Gateway® system allowed fast and efficient construction of the expression vectors in Table 15. These vectors were generated with the LR recombination reaction, which recombines multiple entry clones with a Destination Vector (see Figure 8). The 5' entry clone (p5E) contains the promoter (see Table 16: p5' Entry Clones) for the final expression vector. The pMe middle entry clone introduces the fluorophore (e.g. iRFP670) for N-terminal tagged proteins (e.g. Rabs) or a protein-fluorophore fusion (e.g. pME-Lamp2-EGPF) (see Table 17: pMe Middle entry clones). The 3' entry clone (p3E) contains generally the protein of Interest (e.g Rab7) or a SV40 late polyA signal (See Table 18: p3' Entry clones). The Destination vector (pDest) contains tol2 sites for Tol2 transposase mediated integration into the genome. Methods 30 Additionally the used destination vectors contained a transgenesis marker (e.g.  $\beta$ crystalline:GFP; The embryos express GFP in their eyes) (See Table 19: Destination Vectors). The transgenesis marker facilitates screening of the F1 generation for potential founders.

## 6.2.2 Zebrafish protocols

Zebrafish embryos were raised and maintained according to the standard conditions described in "The Zebrafish Book" (Westerfield, 2000). Embryos were staged by hpf at the corresponding standard temperature of 28.5°C

### 6.2.2.1 Dechoriation

Embryos were dechorionated before imaging manually with forceps or chemically with Pronase/Protease from *Streptomyces griseus* (Sigma). Chemical dechoriation was performed either with  $\approx 28\text{ng}/\mu\text{l}$  for around 15minutes or  $\approx 16\text{ng}/\mu\text{l}$  for 60 minutes. The reaction was stopped by washing the embryos two times with 1x E3.

### 6.2.2.2 Pigmentation inhibition

In order to improve image acquisition, the pigmentation of the zebrafish embryo was inhibited by incubation in 1x 1-phenyl 2-thiourea (PTU) and 1xE3 at around 24hpf.

### 6.2.2.3 Anesthetization

Adult zebrafish and embryos were anesthetized in 1x E3 containing 1x tricaine (3-amino benzoic acidethylester).

### 6.2.2.4 Genotyping

#### 6.2.2.4.1 Fin clips

Adult zebrafish were anesthetized and placed on a sterile 1L tank lid. The caudal fin was spread with a sterile pipette tip. A sterile razor blade is pressed vertically at the distal part of the caudal fin to cut

a small piece of the fin. The pipette tip is moved along the razor blade, isolating the cut piece of the fin from the razorblade. The isolated piece is transferred to a PCR tube.

#### 6.2.2.4.2 Genomic DNA extraction

The genomic DNA was extracted using alkaline lysis as described in (Meeker, Hutchinson et al. 2007). Fin sample, single embryos or pools of embryos were digested in /incubated with 100µl of 50mM NaOH at a temperature of 95°C for 20minutes. After 10minutes of incubation the tube was quickly flicked. The PCR-tubes were cooled down and the reaction was neutralized by addition of 10µl of 1M Tris HCl pH8. The DNA extract was spun down to pellet cell debris and an aliquot of 1-2µl was used for further PCR reactions.

#### 6.2.2.5 PCR reaction and program

For each generated allele a multiplex four primer PCR was established. For each gene two primers up- and downstream of exon2, one primer binding the wild-type sequence in the mutated region and one primer binding the mutated sequence were designed. The outer primers amplify the entire exon2 regardless of the mutation. The two inner primers are specific for either the wild-type or mutant sequence and are inverse to each other. The outer primers were chosen to be asymmetric to exon2 and result in two differently sized fragments in combination with one of the two allele specific primers. This setup leads in heterozygous fish to three bands. A long band representing binding of the two outer primers and two differently sized shorter bands representing binding of the upstream outer primer with one of the allele specific primers and the downstream outer primer with the other allele specific primer. This allows distinction between wild-type, heterozygous and homozygous genomic DNA within one PCR-reaction.

Table 16 PCR reaction mix for genotyping

Component	20µl reaction
ddH <sub>2</sub> O	16.4µl
Titanium taq buffer <sub>(10X)</sub>	2µl
dNTPs <sub>(10mM)</sub>	0.4µl
Forward primer <sub>(100µM)</sub>	0.08µl
Reverse primer <sub>(100µM)</sub>	0.08µl
Wild-type specific primer <sub>(100µM)</sub>	0.08µl
Mutant specific primer <sub>(100µM)</sub>	0.08µl
Titanium Taq polymerase <sub>(50X)</sub>	0.08µl
genomic DNA	0.8 - 1µl

6.2.2.5.1 *rab7a<sup>ubs51</sup>*Table 17 PCR-program for genotyping of *rab7a<sup>ubs51</sup>*

Step	Temperature	Incubation time
Pre-warming	98°C	hold
Initial denaturation	98°C	1:00
35 cycles	98°C	0:30
	65°C	0:30
	68°C	0:10
Final extension	68°C	3:00
Hold	8°C	hold

6.2.2.5.2 *rab7ba<sup>ubs52</sup>*Table 18 PCR-program for genotyping of *rab7ba<sup>ubs52</sup>*

Step	Temperature	Incubation time
Pre-warming	98°C	hold
Initial denaturation	98°C	1:00
30 cycles	98°C	0:30
	65°C	0:30
	68°C	0:10
Final extension	68°C	3:00
Hold	8°C	hold

6.2.2.5.3 *rab7bb<sup>ubs53</sup>*Table 19 PCR-program for genotyping of *rab7bb<sup>ubs53</sup>*

Step	Temperature	Incubation time
Pre-warming	98°C	hold
Initial denaturation	98°C	1:00
33 cycles	98°C	0:30
	68°C	0:30
	68°C	0:25
Final extension	68°C	3:00
Hold	8°C	hold

6.2.2.5.4 *unc13d<sup>ubs54</sup>*Table 20 PCR-programm for genotyping of *unc13d<sup>ubs54</sup>*

Step	Temperature	Incubation time
Pre-warming	98°C	hold
Initial denaturation	98°C	1:00
30 cycles	98°C	0:30
	67°C	0:30
	68°C	0:30
Final extension	68°C	3:00
Hold	8°C	hold

## 6.2.3 Injections

Zebrafish embryos were collected and injected at the one cell stage. Borosilicate glass needles were pulled from capillaries (outer diameter: 1mm, inner diameter 0.5mm BRAND) with the needle puller (Sutter instruments). One cell stage embryos were mounted on squared 1% agarose molds in an E3 filled petridish. The injection needle was broken at the tip with forceps and loaded with the injection mix. The loaded needle was mounted on the FemtoJet Injector (Eppendorf) or PV820 injector (WPI) and the pressure was adjusted to the volume of approximately 5nl. After the injection the embryos were transferred to blue egg water.

## 6.2.3.1 Cas9 protein and gRNA injections

For targeted mutagenesis, eggs were injected at one cell stage with a mixture of gRNA and Cas-9 protein in a 1:1 ratio. Injection mix composition Injection mix was calculated using the website ([https://lmwebr.shinyapps.io/CRISPR\\_Cas9\\_mix\\_calc/](https://lmwebr.shinyapps.io/CRISPR_Cas9_mix_calc/)) from ((Burger, Lindsay et al. 2016)), which calculates a 1:1 ratio for gRNA and Cas-9 protein. Cas9-Protein (6.67mg/ml) 0.8µl, gRNA (1000ng/µl) 0.8µl, Nuclease Free Water 2.4 µl.

## 6.2.3.2 Morpholino Injections

One to two cell-stage embryos were injected with 4 ng of antisense morpholino oligonucleotide targeting the splice donor site of Exon2 of the respective *rab7* gene (*rab7a*: 5'-GTTGATTGCGAGAACTCACCCGGA-3'; *rab7ba*: 5'-ATGCTGAACAAAACACTTACCCAGA-3'; *rab7bb*: 5'-AAAGCCATCACTTACCCAGAATCCC-3').

## 6.2.4 General experimental setup for Image acquisition

Adult zebrafish were set up for mating in mating cages. The eggs were collected directly after mating with a sieve and cleaned with E3. After one to two hours, only fertilized eggs were selected and distributed into petri dishes with blue egg water. Six hours later the plates were controlled for dead embryos. All healthy embryos were transferred to a plate with fresh blue egg water. At around 24hpf the embryos are transferred to E3 with 1x PTU. In order to analyse lumen invagination and lumen fusion the embryos were either incubated at 32°C and imaged around 33-35hpf or incubated at 25°C and imaged around 46-60hpf.

### 6.2.4.1 Mounting

Embryos were dechorionated, selected for bright expression and anesthetized in 1xE3 containing 1x tricaine. 0.7% low melting agarose (Sigma) was melted, supplemented with 1x Tricaine and 1x 1-phenyl-2-thiourea (PTU; Sigma-Aldrich) and kept at 58°C. Glass bottom dish (0.17 mm, MatTek) was covered with 90µl of mounting agarose and the agarose was allowed to cool down shortly before addition of the anesthetized embryos, in order to avoid a strong heat shock. The embryos were further aligned with an eyelash mounted on a piercing tool. After solidification of the low melting agarose, E3 supplemented with 1x PTU and 1x Tricaine was added.

### 6.2.4.2 Point scanning Confocal imaging

For live imaging the incubation chamber was set to 28.5°C one hour before imaging. The laser intensities were set according to/adjusted to the strength of the fluorescent signal. The z-step size was set between 0.2 to 8µm for stacks acquired with the 10x and 20x objective. For stacks acquired with the 40x objective the z-step size was set between 0.2 to 0.5µm. The point scanner was set to 400Hz or 700Hz with various zooms and bidirectional scanning. The line average was generally set to three.

### 6.2.4.3 Quantification of vessel diameter

Measurements were done using ImageJ. In Z-stack time lapse movies the last recorded frame was used after overnight image acquisition was always stopped at the same time. Vessels which were seen to have a collapsed lumen due to secondary sprouting were ignored. All other vessels were measured at three different points along the ISV. Measurement was taken perpendicular to the vessel axis at the respective point. At the end an average of all three measurements was plotted.



#### 6.2.4.4 Quantification of Lamp2-RFP vesicle size

Vesicle size was determined by hand using ImageJ. A region of interest (ROI) was selected around the T-shaped tip cell of developing sprouts. The last time frame before the cell was lumenized was used. The selected Area had always a size of 200-200 pixels (1985 $\mu\text{m}^2$ ). Within this area ROIs were drawn around every Lamp2-RFP positive dot, that remained bigger than 3 pixels after contrast adjustment to eliminate background. Single pixels were neglected independent of their signal strength. Every single measured vesicle was plotted.

#### 6.2.5 Targeted MS of *rab7* proteoforms

##### 6.2.5.1.1 Sample preparation

10-20 embryos were deyolked using forceps in 1X E3 and immediately stored in an empty Eppendorf tube on ice. Embryos were sonicated using glass beads in Bioruptor in 20 $\mu\text{l}$  lysis-buffer. 20 cycles with 30 seconds on and 30 seconds off were used. Samples were then incubated at 95°C and 300 RPM for 10 min. 1 $\mu\text{l}$  of iodoacetamide is added and the sample is incubated in the dark at 25°C for 30min. Not more than 50 $\mu\text{g}$  of sample is being loaded onto the S-trap column after addition of phosphoric acid to a final concentration of 1.2% and 330 $\mu\text{l}$  S-trap buffer. After a spin down at 4000g for 1min the column is washed 3 times with S-trap buffer. Afterward the sample was digested using 20 $\mu\text{l}$  of digestion buffer and 0.75 $\mu\text{g}$  of trypsin. After 1h of incubation at 47°C peptide was collected. To collect 40 $\mu\text{l}$  of S-trap buffer, 40 $\mu\text{l}$  of 0.2%formic acid and 35 $\mu\text{l}$  of 50% acetonitrile acid was added stepwise to the column and always spun down at 4000g in between. Peptides were dried for 1h in vacuum chamber. Peptides were dissolved in LC buffer (0.1% formic acid in water) and the peptide concentration determined using a SpectroStar nano Spectrophotometer (BMG Labtech, Germany) and set to 0.5  $\mu\text{g}/\mu\text{L}$ .

##### 6.2.5.1.2 Analysis

Parallel reaction-monitoring (PRM) assays ((Peterson, Russell et al. 2012), (Gallien, Duriez et al. 2012)) were generated from a mixture containing 50 fmol/ $\mu\text{L}$  of each proteotypic heavy reference peptide (Table 14, JPT Peptide Technologies GmbH). 2  $\mu\text{L}$  of this standard peptide mix were subjected to LC-MS/MS analysis using a Q Exactive plus Mass Spectrometer fitted with an EASY-nLC 1000 (both Thermo Fisher Scientific) and a custom-made column heater set to 60°C. Peptides were resolved using a EasySpray RP-HPLC column (75 $\mu\text{m}$   $\times$  25cm, Thermo Fisher Scientific) and a pre-column setup at a flow rate of 0.2  $\mu\text{L}/\text{min}$ . The mass spectrometer was operated in DDA mode. Each MS1 scan was followed by high-collision-dissociation (HCD) of the precursor masses of the imported isolation list and the 20 most abundant precursor ions with dynamic exclusion for 20 seconds. Total cycle time was approximately 1 s. For MS1, 3e6 ions were accumulated in the Orbitrap cell over a maximum time of 50 ms and scanned at a resolution of 70,000 FWHM (at 200 m/z). MS1 triggered MS2 scans

were acquired at a target setting of 1e5 ions, a resolution of 17,500 FWHM (at 200 m/z) and a mass isolation window of 1.4 Th. Singly charged ions and ions with unassigned charge state were excluded from triggering MS2 events. The normalized collision energy was set to 27% and one microscan was acquired for each spectrum.

The acquired raw-files were searched using the MaxQuant software (Version 1.6.2.3) against a *Danio rerio* (Zebrafish) database (downloaded from [www.uniprot.org](http://www.uniprot.org) on 2021/11/02, in total 46,848 entries) using default parameters except protein, peptide and site FDR were set to 1 and Lys8 and Arg10 were added as variable modifications. The search results were imported into Skyline (v21.1.0.278) ((MacLean, Tomazela et al. 2010)) to build a spectral library and assign the most intense transitions to each peptide. An unscheduled mass isolation list containing all peptide ion masses was exported and imported into the Q Exactive Plus operating software for PRM analysis. Here, peptide samples for PRM analysis were resuspended in 0.1% aqueous formic acid, spiked with the heavy reference peptide mix at a concentration of 2 fmol of heavy reference peptides per 1 µg of total endogenous peptide mass and subjected to LC–MS/MS analysis on the same LC-MS system described above using the following settings: The MS2 resolution of the orbitrap was set to 17,500/35,000 FWHM (at 200 m/z) and the fill time to 50/110ms for heavy/light peptides. AGC target was set to 3e6, the normalized collision energy was set to 27%, ion isolation window was set to 0.4 m/z and the first mass was fixed to 100 m/z. A MS1 scan at 35,000 resolution (FWHM at 200 m/z), AGC target 3e6 and fill time of 50 ms was included in each MS cycle. All raw-files were imported into Skyline for protein / peptide quantification. To control for sample amount variations during sample preparation, the total ion chromatogram (only comprising precursor ions with two to five charges) of each sample was determined using Progenesis QI software (Nonlinear Dynamics (Waters), Version 2.0) and used for normalization. Normalized ratios were further normalized relative to the control condition and the median ratio among peptides corresponding to one protein was reported

### 6.2.6 Assembly of phylogenetic tree

To assemble a phylogenetic tree of the *rab7* genes, protein sequences were assembled from ensemble genome browser ([ensembl.org](http://ensembl.org)). The sequences were then listed in a txt file which was uploaded to [www.ebi.ac.uk](http://www.ebi.ac.uk) ((Madeira, Park et al. 2019)). Tree data was then visualized using [phylo.io](http://phylo.io) ((Robinson, Dylus et al. 2016)) and adjusted using Adobe Illustrator. Amino acids of the following genes were used: *Homo sapiens* (human): *rab7A*: ENSG00000075785, *rab7B*: ENSG00000276600; *Mus musculus* (mouse): *rab7a*: ENSMUSG00000079477, *rab7b*: ENSMUSG00000052688; *Drosophila melanogaster* (fruit fly): *rab7*: FBgn0015795; *Danio rerio* (zebrafish): *rab7a*: ENSDARG00000020497, *rab7b*: ENSDARG00000021287, *zgc:100918*: ENSDARG00000087243; *Cyprinus carpio* (common carp): *rab7a*: ENSCCRG00000027229, *rab7b*: ENSCCRG00000044991, *zgc:100918*: ENSCCRG00000016691;

*Sinocyclocheilus graham* (golden line barbel): *rab7a*: ENSSGRG00000034717, *rab7b*: ENSSGRG00000031796, *zgc:100918*: ENSSGRG00000020044; *Carassius auratus* (Goldfish): *rab7a*: ENSCARG00000008208, *rab7b*: ENSCARG00000017207, *zgc:100918*: ENSCARG00000004993.

### 6.2.7 Transcriptomics data

Transcriptomics data was collected from two available databases. (Lawson, Li et al. 2020) presents transcriptomics data regarding endothelial specific expression of genes. Developmental stage specific transcriptomics data was made available on <https://www.ebi.ac.uk/gxa/experiments/E-ERAD-475> and is currently unpublished, but we would like to thank the Busch-Nentwich lab for providing RNA-seq data. In both cases data was then visualized using Prism (Graphpad).

## 7 Discussion

In this study we used CRISPR/Cas9 induced mutagenesis to establish four new mutant zebrafish lines, *rab7a<sup>ubs51</sup>*, *rab7ba<sup>ubs52</sup>*, *rab7bb<sup>ubs53</sup>* and *unc13d<sup>ubs54</sup>*. These mutants were used to investigate the role of *rab7* for general survival of zebrafish and established that there is a third, expressed and functional paralogue of *rab7*, *rab7bb*. We could also show that despite being a copy of *rab7ba*, the function of *rab7bb* is redundant to the function of *rab7a* and that *rab7ba* seems to fulfil a different role compared to its two paralogues. We did initial studies to see to which degree the late endocytic pathway plays a role in vascular lumen extension and fusion. Additionally, the analysis of the *D. melanogaster stac* homologue in zebrafish, *unc13d*, revealed that the lumen fusion mechanism in fish, unlike in *D. melanogaster*, is not exclusively dependent on *unc13d*. Together these data show, that if lumen formation in vascular anastomosis uses similar mechanisms as tracheal anastomosis, the underlying mechanisms are controlled by a more complex network of proteins, or need to be studied in an inducible manner in a multiple mutant background.

### 7.1 Identification and description of a novel *rab7* gene

Previously it was reported that there are two *rab7* paralogues in zebrafish. An additional gene that showed *rab7*-like sequences was identified. An analysis of available transcriptomics databases revealed that this gene was expressed in the entire organism. Expression levels of the so far unstudied gene are equally high as the well-studied *rab7a*, and therefore much higher than *rab7ba*. This indicates, that despite *rab7bb* being the last annotated copy of the three, that its function is more important than the function of *rab7ba*. In a phylogenetic study, based on the protein sequence of *rab* genes from many species, it has been reported that there is a gene resembling *rab7* sequences, that was called *rab7c* (Mackiewicz and Wyroba 2009). In their study they were additionally able to find a *rab7c* gene in *Xenopus tropicalis*. However, the gene they identified as *rab7c* is not the same gene we analysed. Their zebrafish gene only shows around 50% identity to the three *rab7* genes analysed in this study, and the *rab7c* gene in *Xenopus tropicalis* has since been renamed *rab29*. Therefore, we can conclude, that this is not another *rab7* copy to study and that the third annotated copy in zebrafish is so far the only case of a studied additional *rab7* gene. It is difficult to speculate, whether one might expect another copy of *rab7* to be annotated in the future in zebrafish. Many genes found in other vertebrates have an additional copy in zebrafish and this was also true for *rab7b*, therefore, it might be possible that a copy of *rab7a* will be found eventually. In our search within the sequenced genome of the zebrafish, we did not find any other known gene or protein that shows *rab7* similarities. Furthermore, the fact that the initially generated double mutant (*rab7a<sup>ubs51</sup>*; *rab7ba<sup>ubs52</sup>*) did not show any strong phenotypes while the *rab7a<sup>ubs51</sup>*; *rab7bb<sup>ubs53</sup>* double mutant shows such a strong lethality, makes it rather unlikely that we would expect a fourth *rab7* gene.

## 7.2 Generation of *rab7* mutant alleles

Generation of the mutant alleles worked very efficiently in all three *rab7* genes. Even though the screening of pools cannot precisely determine the efficiency of the mutagenesis, the fact that for *rab7ba* and *rab7bb* all the analysed pools were positive, hints towards an efficiency that is much higher than 20%. For *rab7a* efficiency was slightly lower, which could be due to a less efficient gRNA binding, a higher number of unpredicted, potentially lethal, off-targets or it might be due to *rab7a* being more crucial for embryonic survival. The last two could both lead to a higher mortality in embryos with a high dose of injection mix or very efficient gene editing, which would result in less mutated embryos in the overall population. Additionally screening for *rab7a* mutagenesis was performed via sequencing, due to a lack of a fitting restriction enzyme. The restriction assay is more sensitive since smaller percentages of uncut product can be visualized on an agarose gel, while they are being lost in the background of sequencing reactions. In general, mutagenesis was very efficient, which was also resembled in the low number of adult G0 fish that needed to be screened. For all genes, within ten adult fish, several mutant alleles could be identified, with at least two leading to a premature stop codon. Due to time constraints only one of the alleles was crossed to markers and other mutant *rab7* alleles. Early attempts to create a complete deletion, using two gRNAs before the first and after the last exon, were unsuccessful. In both cases, gRNAs after the last exon didn't seem to cut. It remains unclear why it wasn't possible to find working gRNAs in these regions.

The generated alleles could be validated by a proteomics approach. In collaboration with the proteomics facility of the Biozentrum, we could detect all Rab7 isoforms in wild-type embryos. This data reflects what was shown in the two available transcriptomics databases: Rab7a and Rab7bb are strongly expressed, while Rab7ba is expressed at much lower levels. Analysis of maternal-zygotic homozygous embryos for each of the *rab7* genes also revealed, that the isolated mutant alleles were null mutants. There could no residual protein be detected anymore. The used reference peptides all reflect AA sequences that would be expected to be found if protein synthesis, would start at the next downstream start codon. However, the analysis doesn't indicate that there would be any shortened fragment of the protein produced. Expression of Rab7ba was too low to be detected by assays with a Rab7ba specific reference peptide in any of the analysed mutants. Therefore, a pan Rab7a-Rab7ba probe was used, and measuring of Rab7ba levels requires comparison of different samples. Only signal coming from the same reference peptide can be compared directly. But signal strength of the pan Rab7a-Rab7ab reference peptide was consistent. This allowed to conclude that Rab7bb was indeed absent in *rab7bb<sup>ubs52</sup>* mutants. This proteomics analysis revealed that there is no compensation between *rab7* genes. None of the three isoforms was upregulated in any of the analysed samples compared to the wild-type. Therefore, we conclude, that wild-type levels of *rab7a*

or *rab7bb* alone are sufficient for embryo survival. These proteins are functionally redundant and only loss of both resembles a lack of *rab7a* as was shown in other organisms.

### 7.3 Viability of *rab7* mutant alleles

It was reported that lack of Rab7 function is lethal for mice, *D.melanogaster* and *C. elegans* (Kawamura, Sun-Wada et al. 2012). We could show that in zebrafish loss of a single *rab7* gene, is not lethal. In *C. elegans* and *D. melanogaster* there is only one *rab7* gene reported and it is therefore not surprising that the loss of *rab7* leads to a stronger effect. In mice however, two different *rab7* genes are known, *rab7a* and *rab7b*. The results in (Kawamura, Sun-Wada et al. 2012) indicate that the function of Rab7a and Rab7b are distinct and that loss of *rab7a* is enough to cause embryonic lethality. Our results indicate that this might be similar in zebrafish. Our results show that loss of *rab7a* isn't lethal, probably because there is functional redundancy between *rab7a* and *rab7bb*. If both genes are knocked out however, we do see a strong increase in lethality, despite Rab7ba present. However, in zebrafish Rab7ba can partially rescue the embryo since roughly 10% of of *rab7a*; *rab7bb* double homozygous embryos survive. In crosses that result in triple homozygous embryos, we could only show that these embryos survive at least up to 24hpf. This indicates further that a triple homozygous knockout is lethal and implicates that the surviving fraction from double homozygous *rab7a<sup>ubs51</sup>*; *rab7bb<sup>ubs53</sup>* incrosses are rescued by Rab7ba. It would be interesting to see, whether lethality of these embryos is due to developmental defects or whether cells triple mutant for *rab7* are incapable to maintain cellular homeostasis. Transplantation experiments, where cells from triple homozygous embryos are injected into wild-type embryos, could show whether these cells survive or not. If they do, such systems could also be used to gain first insights into more tissue specific role of *rab7*.

### 7.4 Maternal contribution of *rab7*

It is known that in *D. melanogaster* maternal deposition of *rab7* is important for embryonic development. And also the early lethality in mouse embryos indicates that *rab7* is maternally contributed (Kawamura, Sun-Wada et al. 2012, Best and Leptin 2020). For zebrafish data provided in a transcriptomic atlas suggests, that this is also the case in zebrafish for *rab7a* and *rab7bb*. The transition from maternal to zygotic mRNA translation (MZT) in zebrafish takes place from 3hpf to 5hpf (Laue, Rajshekar et al. 2019). The early lethality of the analysed mutants is therefore likely due to maternal contribution, since zebrafish develop robustly within the first 24hpf unless maternally contributed genes are affected. Additionally, the striking difference between *rab7a<sup>ubs51</sup>*; *rab7bb<sup>ubs53/+</sup>* incrosses and *rab7a<sup>ubs51</sup>*; *rab7bb<sup>ubs53</sup>* double homozygous incrosses shows clearly, that *rab7bb* must be contributed maternally. Additionally, the lumen diameter keeps increasing from *rab7a* zygotic to *rab7a maternal zygotic* embryos, which further shows that what was seen in the transcriptomics data, seems also to be true on the protein level for *rab7a*.

## 7.5 Lumen formation in *rab7* single and double mutants is only slightly impaired.

Previous results in our lab show that the apical membrane marker mcherry-CAAX forms vesicle-like structures in endothelial cells during lumen formation. Especially during trans cellular lumen formation these vesicles can be seen to move to the invaginating membrane, elongate and dissolve. These compartments could be shown to be part of the late endosomal/ lysosomal machinery, due to their colocalization with Rab7, Rab9 and Lamp2. Furthermore, using the Lamp2 marker it could be shown that these vesicles not only dissolve along the growing membrane but integrate after elongation. This shows that vesicles, which according to the literature must originate from Rab7 positive vesicles (Guerra and Bucci 2016), play a role in lumenization of the vascular sprouts. We could show that this role for the analysed mutant combinations is not vital for lumen formation in the zebrafish vasculature, since *rab7* single mutants do not show any significant phenotype in lumen formation. All ISVs that were analysed in the mutant embryos were lumenized at 48hpf. The same could be observed in the two analysed *rab7* double mutants; *rab7a<sup>ubs51</sup>*; *rab7ba<sup>ubs52</sup>* and *rab7a<sup>ubs51</sup>*; *rab7bb<sup>ubs53</sup>*. To fully analyse the role of *rab7* in lumen formation a full knockout of all three isoforms is needed, but these fish are embryonic lethal. These experiments require a system in a full *rab7* knockout background with a rescue construct or an endogenous knock-in. A rescue construct needs to be expressed globally and could then be knocked-down tissue specifically. Endogenous knock-ins in zebrafish remain a challenging task. There is still no efficient method available to generate in frame protein fusions endogenously in zebrafish. The ideal experiment would allow to knock-down *rab7a* or *rab7bb* specifically in endothelial cells in a double mutant background and follow lumen formation in endothelial cells, that lack all Rab7. To achieve such a system, using protein binders that were shown in our group to specifically knock-down proteins of interest in an inducible or tissue specific manner and combining these techniques with our questions would be the dream experiment.

As a more quantitative approach to see eventual subtle changes in lumen morphology, we analysed the resulting diameter of ISVs at 48hpf. What we could see were two trends: 1) a continuous increase in diameter for mutants of the functionally redundant genes *rab7a* and *rab7bb*. and 2) a decrease in lumen diameter in *rab7ba* mutants.

Lumen diameter keeps increasing from *rab7a* zygotic homozygous mutant over *rab7a* maternal-zygotic homozygous mutants to a statistically significant increase in maternal-zygotic double homozygous *rab7a*; *rab7bb* mutants. On the other hand, the decrease in *rab7ba* mutants shows a similar pattern. A decrease can already be seen in zygotic homozygous *rab7ba* mutants, which becomes statistically significant in *rab7ba* maternal-zygotic mutants and is even stronger reduced in maternal-zygotic *rab7a*; *rab7ba* double homozygous mutants. This indicates two things: 1) despite

the low expression of *rab7ba* it is not functionally irrelevant and 2) the loss of *rab7ba* seems to dominate the loss of *rab7a*. It remains difficult however, to make functional assumptions from these measurements. Lumen diameter is affected by a wide range of things, one of the most prominent is the blood pressure. Without blood pressure, vascular lumen collapses. This was shown in (Lenard, Ellertsdottir et al. 2013) and it is plausible that *rab7* has an effect in many aspects related to blood pressure. It can play a role in heart development or leads to a less efficient metabolism due to the lack of lysosomal degradation (Kinchen and Ravichandran 2010), synthesis of new blood cells or due to its high expression in neurons, to neuro muscular (Deinhardt, Salinas et al. 2006) or just neuronal deficiencies (Kawauchi, Sekine et al. 2010). Especially in *rab7ba* mutants heart oedemas were quite common after imaging, but these usually resolved again before 3dpf. Lastly it is shown that lysosomal fusion to membranes is a mean of wound healing (Andrews, Corrotte et al. 2015), this mechanism might be needed in the rapid expansion of the luminal surface and maintains proper stability of the apical membrane. The lack of *rab7* might lead to a less stable luminal surface which is stronger affected to the increase in blood pressure. All together this assay was a way to look for potential subtle phenotypes and show a consistent trend over several measurements. They cannot, however, provide any functional insight to how these differences occur.

## 7.6 *rab7* single and double mutants are capable of lumen fusion

In (Caviglia, Brankatschk et al. 2016) a model is presented in which lysosome related organelles are required for apical membrane fusion in *D. melanogaster* tracheal anastomosis. It was shown that apical membrane growth doesn't require *rab7* but is more heavily dependent on *rab11*. However, the *stac*, *rab39* positive LROs, which are required for lumen fusion, colocalize with *rab7*. Vascular lumen in zebrafish has also been shown to develop via two distinct processes, and while lumen fusion is required in transcellular lumen formation. It is not clear yet, whether lumen fusion is required for lumen formation in cord hollowing. The big difference between the two is the timing cellular rearrangements. While they take place in transcellular lumen formation after the lumen has been established, in cord hollowing rearrangements take place before the lumen opens (Herwig, Blum et al. 2011). It does so by opening the formed luminal patches established in the early stage of anastomosis. We could show that the resulting lumen in *rab7a* and *rab7ba* single mutants and *rab7a*; *rab7ba* double homozygous mutants does not exclusively form via cord hollowing. But that transcellular lumen formation and lumen fusion of invaginating apical membrane takes place. These experiments couldn't be done in *rab7a*; *rab7bb* double homozygous mutants, but movies taken of these embryos, but lacking junctional markers hint strongly that they are capable of transcellular lumen fusion as well. These experiments hint towards that the role of *rab7* in lumen fusion is not as important in zebrafish, as it was proposed to be in *D. melanogaster*. To indefinitely answer this



question by studying a full *rab7* knockout, a conditional full *rab7* knockout system is needed, as previously discussed.

### 7.7 *rab7* single and double mutants show difference in vesicle size but not number.

Previously published measurements of late endosomes and lysosomes show that they range in diameter from 350-400nm (Araujo, Liebscher et al. 2020). This would result in an area of roughly  $0.5\mu\text{m}^2$  at the thickest part of the vesicle. This is similar to the size of the majority of the measured vesicles. The median is slightly higher than what is proposed, but this might be due to the lack of resolution leading to some clusters of vesicles that couldn't be differentiated and were measured as one. Predicting how vesicle size should be affected due to the lack of *rab7* is difficult. While in some studies depletion of *rab7* leads to an increase in vesicle size ((Poteryaev, Fares et al. 2007, Kuchitsu and Fukuda 2018)), in some studies however, the opposite was reported (Kawamura, Sun-Wada et al. 2012). Additionally, some studies show LE and lysosome enlargement when Rab7 is overexpressed (Jimenez-Orgaz, Kvainickas et al. 2018), which we could also see in transgenics injections of EGFP-Rab7a, but on the other hand vesicle size also increased in transient expression of Rab7-DN constructs. These results are inconsistent and seem to be dependent in what cell-types these observations were made and also on which part of endo-lysosomal targeting they were focusing. We could see that Lamp2-positive vesicles increased in size in fish injected with MO against *rab7a* or *rab7bb*. This hints again that these two genes are functionally redundant. The lack of Lamp2-RFP signal in embryos injected with MO against *rab7ba* and the fact that it is shown that Lamp1 is sorted to late endosomes via the TGN(Cook, Row et al. 2004), possibly by distinct Rab7b function (Progida, Cogli et al. 2010) might show that this function in zebrafish is mediated by *rab7ba*. This is further reflected in the result of the mutant analysis. There signal is not completely lost but strongly reduced and size of vesicles is decreased in *rab7ba* heterozygous, homozygous and *rab7a; rab7ba* double homozygous mutants. To study how Lamp2-RFP signal changes in *rab7a; rab7bb* double homozygous mutants it seems vital that Rab7ba is present. Analysing these vesicles should show, taking the the morpholino data into account, that there is an increase in size for Lamp2-RFP positive vesicles.

### 7.8 Conclusion and outlook on the role of Rab7 in the zebrafish vasculature

Together this study of *rab7* mutants shows that the previously proposed third copy of *rab7*, *rab7bb*, is encoding a functional Rab7, which shows Rab7a activity and can compensate for the loss of *rab7a* without need of further upregulation. This shows that these two genes are functionally redundant and together seem to fulfil the function that in other systems is mediated by Rab7a. Additionally there is further evidence that Rab7ba has the suggested Rab7a-distinct function of routing newly synthesized lysosomal markers and proteases from the TGN to the lysosome, but it seems to be

capable to some degree of rescuing the complete loss of *rab7a* and *rab7bb*. All mutants could be analysed using targeted MS proteomics which show that all Rab7-protein in each of the three *rab7* mutants is absent. This shows for mutants generated in the future, that there is an easy way to investigate the consequences of genetic mutations on the protein level with no need of antibodies. We could show that in principle a single 24-hour old embryo yields enough protein for analysis.

Embryos mutant for *rab7* that could be analysed in this study do not show big defects in vascular lumen formation. The question remains however, how lumen formation is affected by the loss of the late endocytic pathway. To analyse the role of *rab7*, conditional knockouts are necessary, because complete Rab7 loss is lethal. This could be achieved by a loxP construct, which can be generated endogenously or introduced with a rescue construct. Ideally, we could generate an endogenous fluorescently tagged knock-in in a *rab7* locus, that rescues the triple mutant. We could then use established protein binder approaches to knock-down Rab7 endothelial specific to study its role in vascular lumen formation without disturbing early development.

Furthermore it would be interesting to see how vesicle size is affected when the two functional redundant *rab7* genes, *rab7a* and *rab7bb*, are absent in Lamp2-RFP positive fish. Would we indeed as hinted in the morpholino study see an increase in vesicle size. It would be interesting to study in which step endocytosis is altered in reference to the two similar *rab7* genes, *rab7a* and *rab7bb* and what role *rab7ba* might play in lysosomal function.

Finally, the mutants presented in this study could further be useful to analyse oogenesis in zebrafish since the bubbly yolk phenotype, which shows similarities with the *C. elegans* SAND1 mutant that prohibits the formation of late endosomes by blocking Rab7 recruiting. It was shown in *C. elegans* and *D. melanogaster* that there is need for *rab7* in deposition of yolk proteins during oogenesis (Poteryaev, Fares et al. 2007, Liu, Sanghavi et al. 2015).

## 7.9 Generation and analysis of *unc13d<sup>dubs54</sup>*

Sequence alignment of the amino acid sequence of the five proteins in the *unc13* family show that two genes could be the zebrafish homologue of the *D.melanogaster* gene *stac*. These two genes, *unc13d* and *baiap3*, show clearly distinct expression patterns with *unc13d* being very strongly upregulated in endothelial cells. The *D. melanogaster* homologue *stac* was shown to play a crucial role in lumen fusion in the trachea, and since we were interested in lumen fusion in the vasculature, the endothelial specific candidate, *unc13d*, was the best candidate to mediate the same function in the zebrafish. Generation of the mutant was designed to reflect the mutation that leads to the strongest phenotype in *D. melanogaster*. The generated mutant was verified by sequencing of the locus, but an analysis on the protein level was not done. Analysis of vascular development in *unc13d<sup>dubs54</sup>* mutants, showed that lumen can form and that lumen fusion in transcellular lumen formation is possible. These results show that *unc13d* is not exclusively required for lumen fusion.

There are four *unc13* genes in zebrafish and with *baiap3*, an additional gene that shares the strongest sequence similarity to *unc13d*. It is therefore possible that the loss of function of *unc13d* is compensated by any of the other *unc13* proteins or *baiap3*. It also remains to be proven that the generated *unc13d*<sup>Jubs54</sup> allele, is a true null mutation that leads to an unfunctional protein. However, the analysed mutant in (Caviglia, Brankatschk et al. 2016), is a short truncation of the C-terminus, where all known important domains are still intact. This shows that already small changes could be enough to lead to an ineffective protein, which would not have been predicted based on the predicted domains. Overall loss of *unc13d* did not lead to the striking phenotype shown in *D. melanogaster* and a more careful and broader approach is needed to dissect the function of *unc13d*, and all its family members, in vascular lumen fusion.

Contributions to publications || Junction-based lamellipodia drive endothelial cell rearrangements in vivo via a VE-cadherin-F-actin based oscillatory cell-cell interaction.

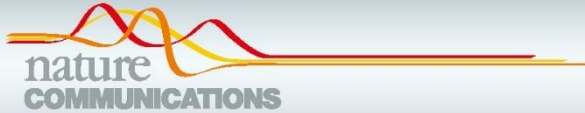
## 8 Contributions to publications

### 8.1 Junction-based lamellipodia drive endothelial cell rearrangements in vivo via a VE-cadherin-F-actin based oscillatory cell-cell interaction.

Paatero I, Sauteur L, Lee M, Lagendijk AK, **Heutschi D**, Wiesner C, Guzmán C, Bieli D, Hogan BM, Affolter M, Belting HG.

[Nat Commun. 2018; PMID: 30171187](#)

I generated the *cdh5<sup>ubs25</sup>* mutant using the CRISPR/Cas9 system. Additionally, I did preliminary screening to confirm that this truncated mutant shows a phenotype, similar to the *cdh5* complete knock-out and established a genotyping protocol. The mutant line was then used by Minkyong Lee, to look further into the role of *cdh5* in linking endothelial cell junctions to the actin cytoskeleton.



ARTICLE

DOI: 10.1038/s41467-018-05851-9

OPEN

# Junction-based lamellipodia drive endothelial cell rearrangements in vivo via a VE-cadherin-F-actin based oscillatory cell-cell interaction

Ilkka Paatero<sup>1,2</sup>, Loïc Sauter<sup>1</sup>, Minkyong Lee<sup>1</sup>, Anne K. Lagendijk<sup>3</sup>, Daniel Heutschi<sup>1</sup>, Cora Wiesner<sup>1</sup>, Camilo Guzmán<sup>3</sup>, Dimitri Bieli<sup>1</sup>, Benjamin M. Hogan<sup>3</sup>, Markus Affolter<sup>1</sup> & Heinz-Georg Belting<sup>1</sup>

Angiogenesis and vascular remodeling are driven by extensive endothelial cell movements. Here, we present in vivo evidence that endothelial cell movements are associated with oscillating lamellipodia-like structures, which emerge from cell junctions in the direction of cell movements. High-resolution time-lapse imaging of these junction-based lamellipodia (JBL) shows dynamic and distinct deployment of junctional proteins, such as F-actin, VE-cadherin and ZO1, during JBL oscillations. Upon initiation, F-actin and VE-cadherin are broadly distributed within JBL, whereas ZO1 remains at cell junctions. Subsequently, a new junction is formed at the front of the JBL, which then merges with the proximal junction. Rac1 inhibition interferes with JBL oscillations and disrupts cell elongation—similar to a truncation in *ve-cadherin* preventing VE-cad/F-actin interaction. Taken together, our observations suggest an oscillating ratchet-like mechanism, which is used by endothelial cells to move over each other and thus provides the physical means for cell rearrangements.

<sup>1</sup>Department of Cell Biology, Biozentrum, University of Basel, Basel 4056, Switzerland. <sup>2</sup>Turku Centre for Biotechnology, University of Turku and Åbo Akademi University, Turku 20520, Finland. <sup>3</sup>Division of Genomics of Development and Disease, Institute for Molecular Bioscience, The University of Queensland, St Lucia, QLD 4072, Australia. These authors contributed equally: Loïc Sauter, Minkyong Lee. Correspondence and requests for materials should be addressed to M.A. (email: markus.affolter@unibas.ch) or to H.-G.B. (email: heinz-georg.belting@unibas.ch)

Organ morphogenesis is driven by a wealth of tightly orchestrated cellular behaviors, which ensure proper organ assembly and function. The cardiovascular system is one of the most ramified vertebrate organs and is characterized by an extraordinary plasticity. It forms during early embryonic development, and it expands and remodels to adapt to the needs of the growing embryo. In adult life, this plasticity allows flexible responses, for example, during inflammation and wound healing<sup>1,2</sup>.

At the cellular level, blood vessel morphogenesis and remodeling are accomplished by endothelial cell behaviors including cell migration, cell rearrangement and cell shape changes<sup>3–5</sup>. This repertoire of dynamic behaviors allows endothelial cells to rapidly respond to different contextual cues, for example during angiogenic sprouting, anastomosis, diapedesis or regeneration. In particular, it has been shown that endothelial cells are very motile, not only during sprouting, but also within established vessels, where they migrate against the blood flow<sup>6,7</sup>.

Endothelial cell migration has been extensively studied in different *in vivo* and *in vitro* systems mainly focusing on angiogenic tip cell behavior and the interaction of endothelial cells with the extracellular matrix (ECM)<sup>8,9</sup>. However, endothelial cells can also shuffle positions within an angiogenic sprout<sup>10</sup>, and these cellular rearrangements require the junctional adhesion protein VE-cadherin/CDH5<sup>11–13</sup>. Moreover, *in vivo* analyses in avian and fish embryos have shown that endothelial cells can migrate within patent blood vessels emphasizing that regulation of endothelial cell adhesion and motility is critical during vascular remodeling processes<sup>6,7,14,15</sup>.

Although many aspects of sprouting angiogenesis and vascular remodeling rely on endothelial cell interactions<sup>3</sup>, the exact role of endothelial cell junctions (and in particular that of VE-cad) in these processes is not well understood. Indeed, rather than supporting an active function for VE-cad in dynamic cell behaviors, most studies point to a restrictive or permissive role, consistent with the maintenance of endothelial integrity<sup>16–18</sup>. On the other hand, the observation that loss of VE-cad function can inhibit cell rearrangements suggests an active contribution to this process<sup>12,13</sup>.

To decipher the cellular and molecular mechanisms, which enable cells to move within the endothelium, we have focused on the process of anastomosis during the formation of the dorsal longitudinal anastomotic vessel (DLAV) in the zebrafish embryo by high-resolution time-lapse microscopy. This process occurs in a relatively stereotypical manner and involves a convergence movement of endothelial cells, which is illustrated by extensive cell junction elongation<sup>19</sup>. Ultimately, this process alters tube architecture and converts unicellular vessels to multicellular vessels<sup>20</sup>. By *in vivo* time-lapse imaging of several junctional components and pharmacological interference with F-actin dynamics, we are able to describe a actin-based mechanism, which allows endothelial cells to move along each other while maintaining junctional integrity. In particular, we describe a rearrangement mechanism, which is initiated by junction-based lamellipodia (JBL) leading to the formation of distal, VE-cad based attachment sites, which in turn serve as an anchor point for junction elongation. We propose that the oscillating behavior of JBL, which depends on F-actin polymerization as well as contractility, provides a general mechanism of endothelial cell movement during blood vessel formation and vascular remodeling.

## Results

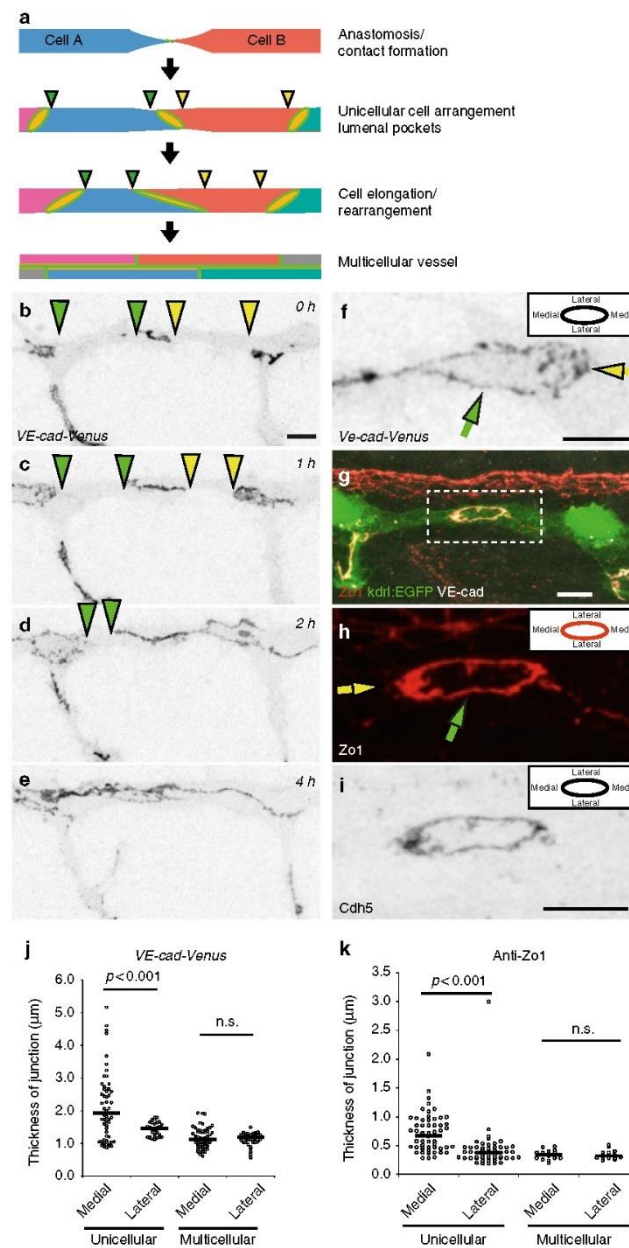
**Changes of vessel architecture during blood vessel formation.** Blood vessel formation is associated with prominent cell shape changes and cell rearrangements. The DLAV presents a well-defined *in vivo* model to analyze how a wide repertoire of

endothelial cell activities leads to the formation of a new blood vessel, starting with establishment of an interendothelial contact point, followed by the formation of a continuous luminal surface and the transformation from a unicellular to a multicellular tubular architecture. Unicellular and multicellular tubes are easily discerned by junctional patterns, whereas unicellular tubes display isolated rings separated by segments without any junction, multicellular tubes have a continuous network of multiple junctions along their longitudinal axis (Fig. 1a). To gain more insight into this transformation process, we used a reporter line expressing a full-length VE-cadherin fluorescent protein fusion (VE-cad-Venus)<sup>21</sup> (Fig. 1b–e, Supplementary Movie 1) and performed *in vivo* time-lapse experiments between 27 and 40 h post fertilization (hpf). These experiments showed that most DLAVs were initially unicellular tubes, and that the majority (69%,  $n = 26$  (8 embryos)) of DLAV segments were transformed to a multicellular configuration before 40 hpf (Fig. 1b–e, Supplementary Fig. 1a). The transformation from the initial tip cell contact to a multicellular vessel, with a continuous cell–cell junction network, took several hours (median 190 min, segments  $n = 14$  (8 embryos), Supplementary Fig. 1b), with high variability between individual segments. During this time window, the endothelial cell–cell junctions expanded extensively from initial spot-like structures to elongated junctions covering the entire DLAV segment. However, movement of the junctions was also seen in perfused vessels (Supplementary Fig. 1c). The cellular rearrangements are thus occurring both in nascent non-lumenized vessels and also in inflated, perfused vessels.

**The thickness of remodeling junctions is polarized.** When we analyzed ring-shaped junctions in the DLAV of VE-cad-Venus embryos in more detail, we observed that the junctions were not uniform in thickness along their circumference in unicellular vessels. In medial regions, the junctions formed significantly thicker, and more diffuse, pattern than on the lateral sides (Fig. 1f, j), coinciding with the general direction of endothelial cell movements during anastomosis. In contrast, we did not observe such junctional polarity in multicellular vessels (Fig. 1j). We confirmed these observations by immunostainings for the junctional proteins VE-cadherin and ZO1, which showed that in the newly formed junctions in unicellular configuration, the medial junctional domains were consistently thicker than the lateral domains (Fig. 1g–i, k). Again, this polarity of junctional thickness was not seen in vessel areas of more mature multicellular architecture (Fig. 1k).

**Remodeling junctions form junction-based lamellipodia.** To gain insight into the nature of this junctional polarity, we performed live-imaging experiments on Cdh5-Venus expressing transgenic embryos at high temporal resolution. Here, we observed that the polarized junctional thickenings are formed by dynamic lamellipodia-like protrusions (Fig. 2a, b, Supplementary Movie 2). In addition, we used a F-actin visualizing EGFP-UCHD transgenic fish line in a similar setup (Fig. 2c, d, Supplementary Movie 3). Remarkably, F-actin and VE-cadherin, both showed similar oscillatory dynamics with a median duration of 6 min (Fig. 2e). Moreover, the protrusions were oriented along the vessel axis (Fig. 2f), which is consistent with the increased junctional thickness of medial junctional domains.

To test whether this dynamic junctional behavior is restricted to the process of anastomosis or is a more general behavior, we further analyzed the F-actin fluctuations during junctional remodeling in the dorsal aorta. Here, we found that the relative intensity of EGFP-UCHD was increased at the site of forming protrusions (Fig. 3a, b, Supplementary Movie 4), indicating



recruitment of additional F-actin. We further analyzed the dynamic behavior of junctional F-actin using kymographs (Fig. 3c, d) and found that the fluctuations in intensity occurred in rather rhythmic patterns, and at the same junctional site, protrusions were generated repeatedly within regular intervals,

indicative for oscillations in F-actin intensity in the remodeling junction.

The polarized occurrence and directionality of protrusions along the direction of vessel growth suggests that they are involved in endothelial cell movements. To address this, we

**Fig. 1** Polarized thickness in remodeling junctions. **a** Schematic model of cellular rearrangements during formation and maturation of dorsal longitudinal anastomosing vessel (DLAV) in zebrafish. At first, the tip cells (Cell A and B) of two anastomosing endothelial sprouts contact and form a de novo junction. Next, a vessel with unicellular architecture is formed, where junctions are not interconnected but are visible as separate rings. Then, through cellular rearrangement and elongation, the junctions elongate along vessel axis until junctions are interconnected and vessel reaches the final multicellular architecture. The edges of the junctional gaps in the unicellular vessels are marked with green and yellow triangles. **b-e** Still pictures of a time-lapse movie (Supplementary Movie 1) showing EC junctions of *Tg(BAC(cdh5:cdh5-ts))* embryo, which expresses VE-cad-Venus fusion protein, during transition from unicellular to multicellular vessel during DLAV formation, in inverted contrast starting around 28 hpf. The edges of the junctional gaps in the unicellular vessels are marked with green and yellow triangles. **f** Close-up image of VE-cad-Venus embryos. The diffuse thickening of medial domain of the DLAV is marked with a yellow arrow. **g-i** Whole-mount immunofluorescence staining of the DLAV using anti-ZO1, anti-VE-cad (rat) of 28–30 hpf (*Tg(kdr:EGFPs843)*) embryos. **h** The yellow arrow points to the medial junctional domain and the green arrow to the lateral junctional domain. **j** Quantification of junctional thickness measurements.  $n = 44$  unicellular junctions and 48 multicellular junctions from 5 VE-cad-Venus *Tg(BAC(cdh5:cdh5-ts))* embryos. Non-parametric Kruskal-Wallis test was used. **k** Quantification of the junctional thickness measurements from immunostainings of *Tg(kdr:EGFPs843)* embryos.  $n = 58$  unicellular junctions and 17 multicellular junctions from 8 embryos. Non-parametric Kruskal-Wallis test was used. Scale bars 10  $\mu$ m

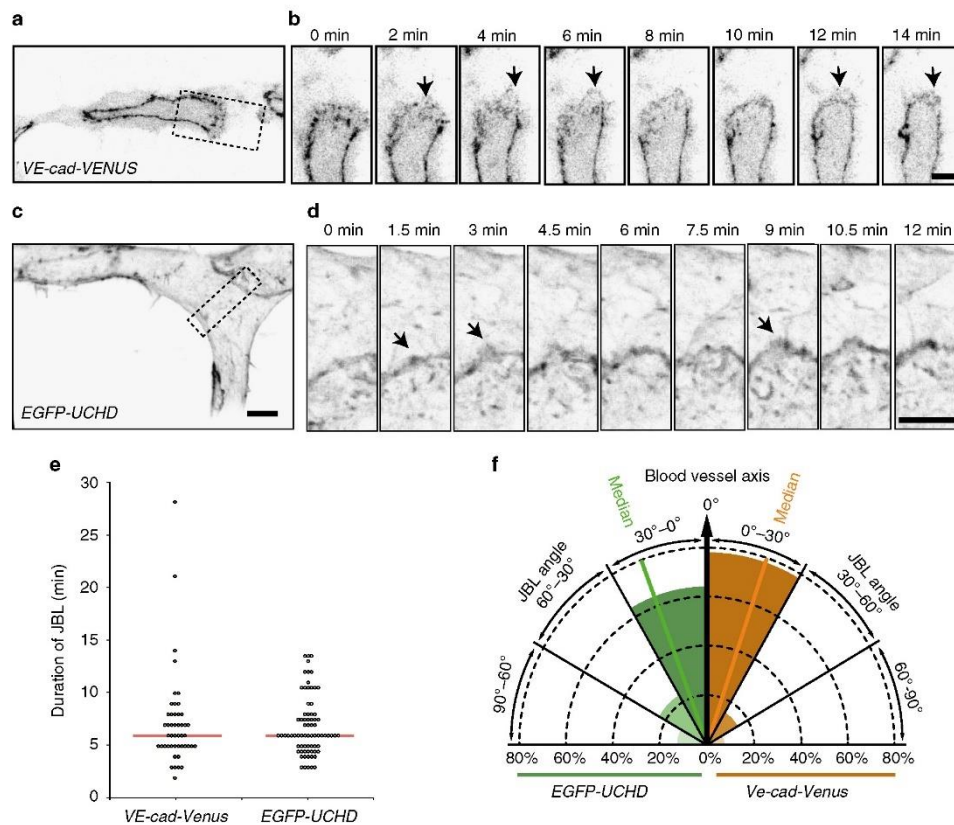


**Fig. 2** Active VE-cad and F-actin behavior of junction-based lamellipodia. **a, b** Still images from a movie (Supplementary Movie 2) of a VE-cad-Venus expressing embryo *Tg(BAC(cdh5:cdh5-ts))*, showing the DLAV at 30 hpf in inverted contrast. **b** A magnification of the inset in **a**. Arrows point to JBL. **c, d** Still images from a movie (Supplementary Movie 3) of a EGFP-UCHD expressing embryo (*Tg(fli:Gal4ff<sup>lts3</sup>, UAS:EGFP-UCHD<sup>lts18</sup>)*) showing the DLAV at 30 hpf in inverted contrast. **d** A magnification of the inset in **c**. Arrows point to JBL. **e** Scatter plot of quantitation of the duration of the JBL with the VE-cad-Venus transgene ( $n = 48$  in 6 embryos) and EGFP-UCHD movies ( $n = 74$  in 6 embryos), red line represents the median. **f** Quantitation of JBL angle in the DLAV in respect to the blood vessel axis ( $0^\circ$ ) using the EGFP-UCHD transgene ( $n = 103$  from 6 embryos) or *Cdh5-Venus* transgene ( $n = 41$  from 5 embryos). Scale bars 5  $\mu$ m



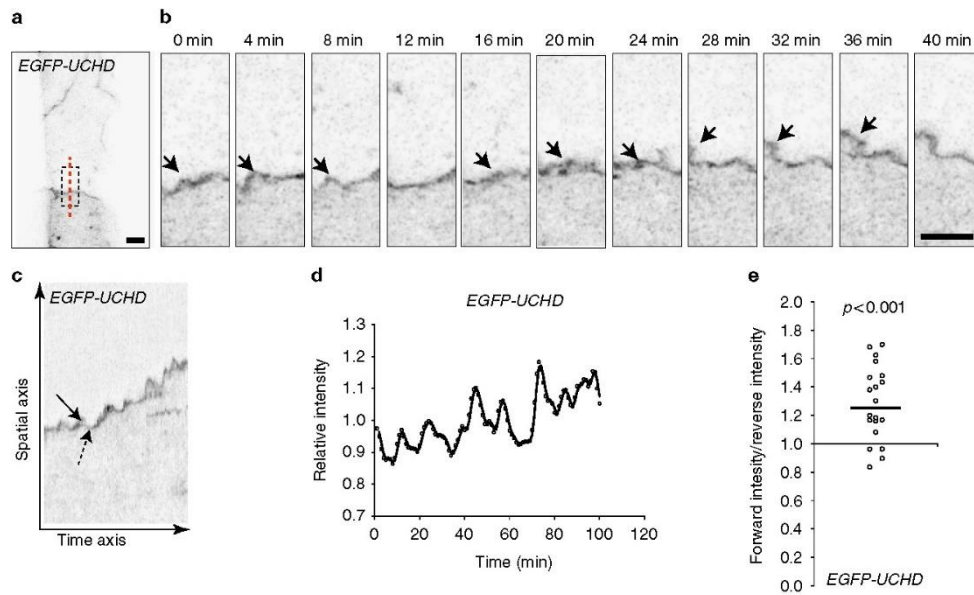


**Fig. 3** Oscillatory F-actin dynamics during remodeling of cell-cell junctions. **a, b** Still images from a movie (Supplementary Movie 4) showing JBL formation in the dorsal aorta of an EGFP-UCHD expressing 2dpf embryo (*Tg(fli:Gal4<sup>UAS</sup>); UAS:EGFP-UCHD<sup>mbst18</sup>*), shown in inverted contrast. **b** A magnification of the inset in **a** and the red dashed line indicates the site for kymograph in **c**. Arrows point to a JBL, seen as a local thickening of the junction. **c** Kymograph across the junction. Solid arrow denotes forward movement and dashed arrow backward movement of the junction. **d** Intensity plotting of a EGFP-UCHD JBL kymograph. **e** Scatter plot of the relative EGFP-UCHD intensity during forward and backward movements ( $n = 20$  events, 4 movies). EGFP-UCHD intensity value in a forward movement was divided with intensity value during subsequent reverse movement. Non-parametric one sample Wilcoxon signed rank test was used as statistical test. Scale bars 5  $\mu$ m

analyzed the potential association between local junctional movements and the occurrence of F-actin protrusions in the dorsal aorta (Fig. 3c, d). Analysis of F-actin intensities showed that higher intensities were associated with local forward movement of junctions than with reverse movement (Fig. 3e).

Taken together, we observe an F-actin-based protrusive endothelial behavior, which occurs during junctional remodeling in vivo. Because of their similarity to ‘classical’ lamellipodia, their oscillating behavior and structural connection with endothelial cell junctions, we call these protrusions junction-based lamellipodia or JBL.

**JBL form at the front end of elongating junctions.** Blood vessel anastomosis is driven by the convergence movement of two tip cells and is associated with an elongation of their mutual cell junction. The formation of JBL at the junctional poles suggested that these dynamic structures may generate tractive forces, which contribute to junction elongation. However, cell junctions demarcate the interface between two cells and our above analyses did not differentiate, whether cells form JBL at their respective junctional front or rear ends or both. To analyze the contributions of individual cells to F-actin protrusions, we generated a transgenic zebrafish line expressing a photoconvertible mCLAV-UCHD fusion protein in endothelial cells. For mosaic analysis, we photoconverted mCLAV-UCHD in single SeA sprouts 2–3 h prior to contact initiation between tip cells from neighboring segments and recorded the behavior of the junctional F-actin later during anastomosis and formation of the DLAV (Fig. 4a). In vivo photoconversion resulted in efficient green-to-red conversion

(Fig. 4b), allowing the analysis of differentially labeled F-actin pools during DLAV formation (Fig. 4c). Photoconverted and non-converted mCLAV-UCHD-labeled endothelial cell junctions and showed matching patterns within the anastomotic junctional ring—except for the poles of the anastomotic ring where F-actin based protrusions were forming. Here, the colocalization of the two markers was suspended and we found elevated levels of either of the two F-actin pools at the front end of the junction with respect to cell movement (green JBL over red cell, or vice versa, 24 out of 28 events,  $p < 0.001$ ). This oriented localization is consistent with an involvement of JBL in the forward movement of tip cells during anastomotic convergence movements.

**F-actin protrusions precede junctional movements.** Since the above observations suggest a step-wise mechanism of cell-cell interaction during JBL function, we set out to explore the spatio-temporal relationship between F-actin dynamics and the dynamics of other junctional components. To this end we generated transgenic fish lines expressing red F-actin (mRuby2-UCHD), which allows a direct comparison with other fluorescently labeled junctional components (e.g., EGFP-ZO1 and VE-cad-Venus) (Fig. 5a, b and c, d, respectively; Supplementary movies 5 and 6). Both VE-cad-Venus and EGFP-ZO1 followed the junctional F-actin front (11 and 9 movies analyzed, respectively); however, a different distribution pattern was observed during JBL formation. VE-cadherin localized diffusely at the front, largely overlapping with the F-actin protrusions (Fig. 5b, 60–120 s.). In contrast, EGFP-ZO1 showed a more defined localization and initially remained associated with the junction at the

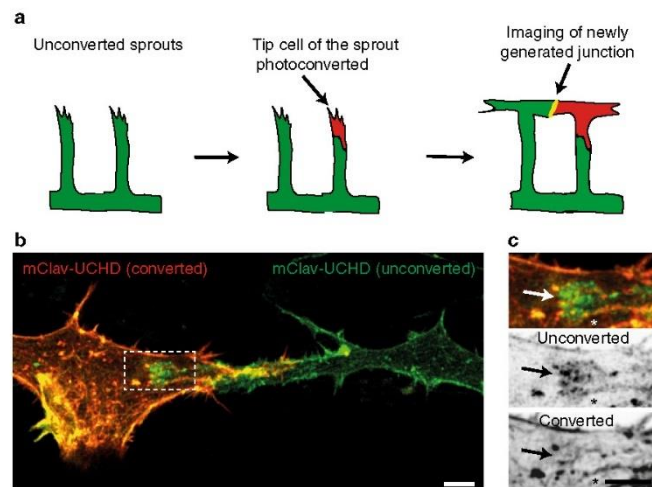


**Fig. 4** JBL formation at the distal tip of the junction during DLAV anastomosis. **a** Schematic representation of the mClav2-UCHD photoconversion experiment. **b** Image of photoconverted and unconverted mClav2-UCHD cells in the DLAV of an *Tg(Hit:Gal4<sup>Ubs3</sup>;UAS:mClav2-UCHD<sup>Ubs27</sup>)* embryo, at 32 hpf. **c** A close up of the inset in **b**. Arrows point to differentially labeled JBL and asterisk (\*) marks the junction outside JBL. Scale bar 5  $\mu$ m

proximal end of the protrusion (Fig. 5d, 0–36 s.). However, at later time points (Fig. 5d, 72 s.), we observed EGFP-ZO1 accumulation also at the front edge of the JBL, indicating the formation of a new junction at this site (Fig. 5d). To directly differentiate the distribution of VE-cadherin and ZO1, we injected a mCherry-ZO1 encoding plasmid into VE-cad-Venus recipients. The differential localization of both proteins confirmed our previous observations and showed that ZO1 distribution is largely restricted to cell junctions. In contrast, VE-cad was also found within areas outside of these junctions (Fig. 5e, f, Supplementary Movie 7).

Therefore, the respective distribution of ZO1 and VE-cad represent different aspects of JBL formation and illustrates a stepwise mechanism of JBL function. First, F-actin based JBL emanate from EC junctions, which are maintained. The JBL contains diffusely distributed VE-cad. This population of VE-cad precedes formation of the new junction in front of the JBL and may therefore provide adhesive properties for the JBL prior to formation of the new junction. Interestingly, a gradual movement of the old junction towards the new junction was observed in the EGFP-ZO1 movies (Fig. 5d). This indicates that the proximal junction is not resolved in situ, but is actually pulled forward and eventually merges with the distal junction.

#### F-actin is required for JBL formation and junction elongation.

To elucidate the molecular mechanism underlying JBL function during endothelial cell movements, we examined the requirement of F-actin dynamics by pharmacological interference. Latrunculin B and NSC23766 (a Rac1 inhibitor) are potent inhibitors of F-actin polymerization and lamellipodial F-actin remodeling, respectively<sup>22,23</sup>. We used acute treatments to avoid secondary effects and performed live-imaging on rearranging endothelial cell junctions. Inhibition of F-actin polymerization led to pronounced defects in JBL formation. In 5 movies, we observed only 13 JBL, compared to 50 JBL in control embryos (Fig. 6a, b, Supplementary Movies 8 and 9). Moreover, those JBL, which did

form in the presence of Latrunculin B, lasted longer, indicating additional defects in lamellipodial dynamics. Inhibition of Rac1 did not interfere as strongly with JBL formation as inhibition of F-actin polymerization. Here, we observed 49 JBL in 10 movies. However, these JBL displayed prolonged duration indicating defects in JBL dynamics (Fig. 6a, b, Supplementary Movie 10).

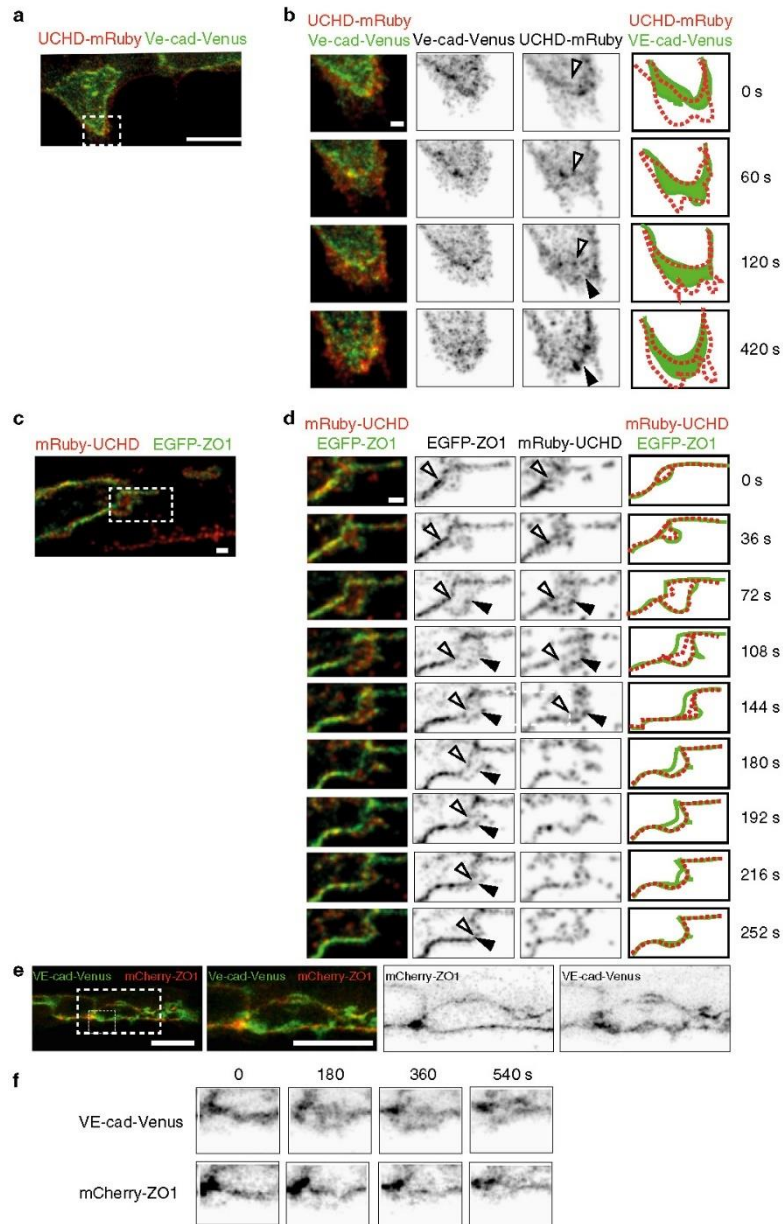
To test whether interfering with F-actin and JBL dynamics has consequences for endothelial cell rearrangements, we analyzed the effect of Latrunculin B and NSC23766 on junction elongation. Both compounds inhibited the elongation of the junction during DLAV formation (Fig. 6c, d) indicating that proper function of JBL is necessary for junctional elongation during anastomosis.

Although the gross morphology of JBL—based on VE-cad-Venus—looked relatively normal upon Rac1 inhibition, we wondered whether localization of other junctional proteins was affected. During the late phase of JBL oscillation, ZO1 is often localized in two lines outlining the distal (new) and proximal (old) junctions (Fig. 5d). When we compared EGFP-ZO1 distribution in control and NSC23766 treated embryos, we found that distal junctions were forming, showing that Rac1 inhibition did not abrogate de novo junction formation (Fig. 6e). Furthermore, despite the appearance of double junctions, we still did not observe any junction elongation in these instances.

As the above results suggested that Rac1 is primarily involved in the regulation of JBL dynamics rather than their structural properties, we analyzed the dynamics of junctional F-actin intensity oscillations (Supplementary Fig. 3b–d). In control embryos we observed a periodic pattern of JBL dynamics, but in NSC23766-treated embryos the periodicity was reduced (Supplementary Fig. 3e), indicating that junctional F-actin oscillations become less coordinated upon Rac1 inhibition.

#### VE-cadherin/F-actin interaction is required for JBL function.

Next, we wanted to explore the role of VE-cad in JBL function, because several lines of evidence suggested that VE-cad may play



an important role in this process. In *ve-cadherin* zebrafish null mutants (*ve-cad/cdh5<sup>ub58</sup>*), blood vessel architecture is generally disrupted and discontinuous lumens prohibit blood flow<sup>13,24</sup>. These defects are caused by an inability of mutant ECs to perform coordinated cell junction elongation, which is required for multicellular tube formation during angiogenesis. Furthermore, the

*ve-cad* mutant defects in junction elongation can be copied by the inhibition of F-actin polymerization<sup>13</sup>.

Our finding that VE-cad accumulates in JBL prior to junction formation is consistent with the above observations, and collectively, they indicate a functional interaction between VE-cad and F-actin during junction elongation. To address this

**Fig. 5** Distinct dynamics of VE-cadherin, F-actin and ZO1 during JBL formation. **a, b** Still images (Supplementary Movie 5) of an embryo showing the DLAV around 32 hpf in an embryo expressing both mRuby2-UCHD and VE-cad-Venus *Tg(flii:Gal4<sup>ff</sup><sup>bs3</sup>;UAS:mRuby2-UCHD<sup>ubs20</sup>;BAC(cdh5:cdh5-Venus))*. **b** A time series magnification of the inset in **a**. Individual channels are shown in inverted contrast. Similar observations were made in 11 movies. Open arrow head points to established junctions and black arrowhead to pioneering junction. **c** and **d** Still images of an embryo showing DLAV around 32 hpf (Supplementary Movie 5) in an embryo expressing EGFP-ZO1 and mRuby2-UCHD *Tg(flii:Gal4<sup>ff</sup><sup>bs3</sup>;UAS:mRuby2-UCHD<sup>ubs20</sup>;UAS:EGFP-hZO1<sup>ubs5</sup>)*. Imaged at rate of 12 s/stack. Similar observations were made in 9 movies. Open arrow head points to established junctions and black arrowhead to pioneering junction. **e** Images of endothelial cells in a VE-cad-Venus expressing embryo injected with mCherry-ZO1 encoding plasmid *Tg(BAC(cdh5:cdh5-ts)); flii:ep:mCherry-ZO1)* ( $n = 7$  embryos). **f** Close-up from panel **e**. Both channels are shown in inverted contrast. Scale bars 1  $\mu\text{m}$  (**b-d**) and 10  $\mu\text{m}$  (**a, e**)

possibility, we generated a targeted mutation in *ve-cad* (*cdh5<sup>ubs25</sup>*), which results in a “tailless” protein, lacking a portion of the cytoplasmic domain of VE-cad including the  $\beta$ -catenin binding site, essential for VE-cad/F-actin interaction (Supplementary Fig. 4).

Despite the deletion, the VE-cadherin protein correctly localizes in the endothelial cell-cell junctions (Fig. 7h, k and Supplementary Fig. 4e). Homozygous *ve-cad<sup>ubs25</sup>* mutants are embryonic lethal and display phenotypes similar to those of null mutants, including tip cell/stalk cell dissociation and defective blood circulation (Supplementary Fig. 5a-e)<sup>13</sup>. However, some of the defects are less pronounced and we observed blood flow in the DA and—in rare cases—in the DLAV (Supplementary Fig. 5a, Supplementary Movie 11). This shows that the extracellular domain of VE-cad mediates some inter-endothelial adhesion, which leads to a hypomorphic phenotype.

To assess the requirement for VE-cadherin/F-actin interaction for JBL formation, we first examined whether the junctional rings of VE-cad truncation (*cdh5<sup>ubs25</sup>*) mutants displayed polarized thickness during anastomosis. Immunofluorescent staining for ZO1 revealed that medial junctions of mutants were narrower compared to heterozygotes, while the thickness of the lateral sides was not affected (Fig. 7a, b). We then tested whether the dynamics of F-actin protrusions were affected in VE-cad truncation (*cdh5<sup>ubs25</sup>*) mutants. Time-lapse analyses in embryos expressing EGFP-UCHD indicated that F-actin protrusions oscillated more slowly in *cdh5<sup>ubs25</sup>* mutants compared to wild-types in a manner similar to how protrusions behaved in the presence of the Rac1 inhibitor (Fig. 7c). Furthermore, by measuring the time-intervals between the end and the beginning of a JBL cycle, we found that this “lag phase” is more than doubled (Supplementary Fig. 4f) suggesting that full-length VE-cad is required for the initiation of JBL formation.

To test whether these defects in JBL have consequences for vascular morphogenesis, we examined the junctional architecture of forming SeA. In *cdh5<sup>ubs25</sup>* mutants, we observed increased interjunctional gaps, which indicate a defect in multicellular tube formation due to a failure in junction elongation (Fig. 7d-l). We also compared relative nuclear movements, which are associated with stalk cell elongation. Consistent with the observed defects in junctional rearrangement, *cdh5<sup>ubs25</sup>* mutants displayed significantly slower rearrangement of EC cell nuclei compared to wild-types (Fig. 7m, n). Taken together, these findings show that VE-cadherin plays an important role in F-actin dynamics and that the VE-cadherin/F-actin interaction is essential for JBL function, junction elongation and endothelial cell rearrangements in vivo.

## Discussion

In this study, we have investigated the mechanisms by which junctional dynamics contribute to endothelial cell movements during blood vessel formation in vivo.

By time-lapse imaging of different structural components of endothelial cell junctions, we observe a dynamic and differential deployment of these proteins during junctional remodeling, which leads to the formation of transient lamellipodia-like

protrusions, that we call JBL. Together with our analyses of F-actin dynamics and VE-cad function, our findings suggest a mechanism of cellular and molecular interactions, which allows endothelial cells to use each other as adhesive substrates and for force transmission during cell migration and elongation (Fig. 8). In essence, JBL act by a ratchet-like mechanism, which consists of F-actin-based protrusions and VE-cad based interendothelial cell adhesion. While F-actin protrusions provide the motive force, VE-cad based adhesion serves as an intercellular clutch.

Our time-lapse experiments show that junction elongation is associated with oscillating JBL, which occur at a frequency of about one every 6 min. This oscillatory behavior, their polarized localization at the leading edge of the junction, their role in cell movements together with their dependency on F-actin polymerization as well as Rac1 GTPase activity indicates that these protrusions share a functional basis with “classical” lamellipodia<sup>25</sup>. However, and in contrast with “classical” lamellipodia, the protrusions, which we are describing, emanate from inter-endothelial cell junctions and require VE-cad for adhesion and force transmission.

Here, we describe the role of JBL during angiogenesis in the zebrafish, where they promote endothelial cell elongation and rearrangements. It remains to be seen, whether JBL are unique to endothelial cells or employed more widely during morphogenetic processes of different cell types. Cadherin-based cell interactions have been shown to be essential for dynamic cell movements in several morphogenetic processes (reviewed by refs. <sup>26,27</sup>). In some aspects, the mechanism of JBL function appears to be similar to the one described for border cell migration during *Drosophila* oogenesis<sup>28</sup>. Here, actin-based cell protrusions and E-cadherin interactions between border and nurse cells are thought to be important to form an anchor point at the leading edge of border cells.

Oscillatory junctional protrusions of endothelial cells have also been described in cultured HUVECs<sup>29,30</sup>. Here, so-called junction-associated intermittent lamellipodia (JAIL) form in similar intervals as JBL. However, several characteristic differences suggest that JAIL and JBL represent different cellular activities. As the name indicates, JAIL formation is preceded by the local dissolution of the existing junction, which is thought to trigger the formation of an actin-based protrusion followed by the formation and stabilization of a new junction. In contrast, JBL formation is not associated with the dissolution of an existing junction. This leads to the formation of a characteristic double junction (proximal and distal) at the pole of the junctional ring (Fig. 8). Conceptually, maintenance of cell junctions should be a prerequisite for endothelial cell rearrangements in a perfused vessel in order to maintain the vascular seal and to prevent hemorrhage. We therefore predict that in the in vivo situation (i.e. developmental angiogenesis), JBL may be more prevalent than JAIL.

The distinct temporal and spatial distribution of VE-cad, F-actin and ZO1 during JBL oscillation suggested that these proteins also partake in JBL function. In agreement with this view, interference with VE-cadherin function, as well as F-actin dynamics inhibited JBL dynamics and junction elongation.

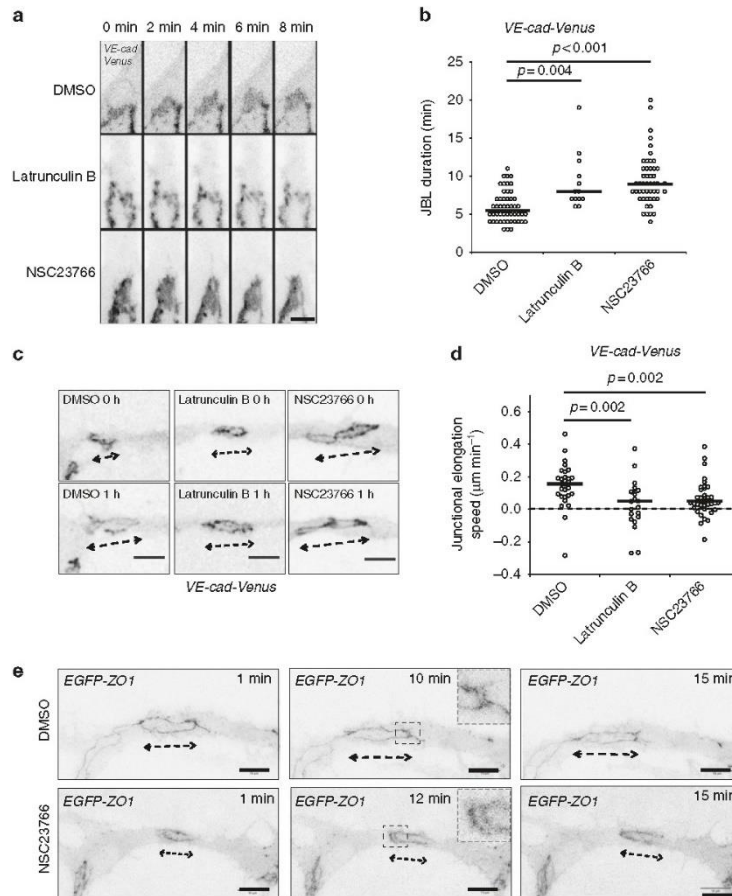
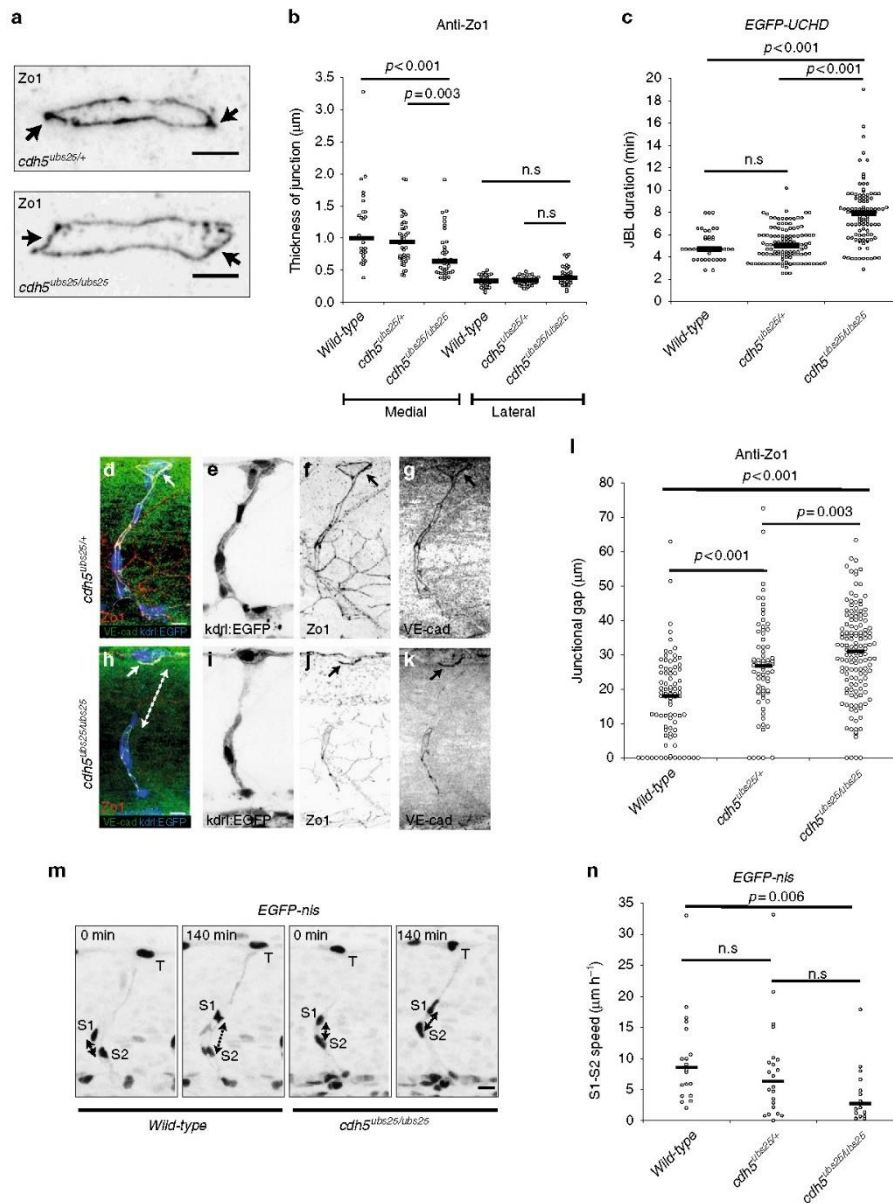


**Fig. 6** Junction elongation and JBL formation are functionally linked. **a** Still images from a movie of an VE-cad-Venus expressing embryo *Tg(BAC(cdh5:cdh5-ts))* during anastomosis in the DLAV (around 32 hpf), in the presence of DMSO (1%), Latrunculin B ( $150 \text{ ng ml}^{-1}$ ) or NSC23766 ( $900 \mu\text{M}$ ). **b** Scatter plot quantitation of the duration of the JBL. DMSO,  $n = 50$  (6 movies); Latrunculin B,  $n = 13$  (5 movies); NSC23766,  $n = 49$  (10 movies); black lines show median values. Non-parametric Kruskal-Wallis statistical test was used. **c** Confocal images of a *Tg(BAC(cdh5:cdh5-ts))* embryo during junctional elongation after DLAV anastomosis. Top panels  $t = 0$  and bottom panels after 1 h incubation. **d** Quantification of the junctional elongation velocity in the presence of different chemicals using *Tg(BAC(cdh5:cdh5-ts))* embryos. DMSO (1%),  $n = 29$  junctions (11 embryos); Latrunculin B ( $150 \text{ ng ml}^{-1}$ ),  $n = 21$  (6 embryos); NSC23766 ( $300 \mu\text{M}$ ),  $n = 41$  (11 embryos). Dotted line indicated no movement observed, black lines are medians. Non-parametric Kruskal-Wallis statistical test was used. **e** Confocal images of anastomosing DLAV of EGFP-ZO1 embryos (*Tg(fli:Gal4ff<sup>ubs3</sup>;UAS:EGFP-hZO1<sup>ubs5</sup>)*) treated with DMSO or NSC23766. Scale bar  $10 \mu\text{m}$

Previous studies have emphasized the importance for VE-cadherin in dynamic endothelial cell interactions including cell rearrangements<sup>11,12</sup> and cell elongation<sup>13</sup>. We generated a *ve-cad* mutation, which disrupts VE-cad/F-actin interaction. The phenotype observed in these mutants is slightly milder than in the null mutant suggesting that the mutant protein still allows interendothelial adhesion. Nevertheless, the increase of discontinuous junctions in SeAs illustrates an inability of mutant endothelial cells to generate multicellular tubes, which in turn suggests defects in cell rearrangements. Consistent with this view, *ve-cad<sup>ubs25</sup>* show reduced spatial distribution of cell nuclei in the SeA. Furthermore, analysis of JBL showed that polarity and oscillatory behavior are disturbed in *ve-cad<sup>ubs25</sup>* mutants. Taken

together, these results show that VE-cadherin actively contributes to morphogenetic cell movements via its interaction with the F-actin cytoskeleton.

The connection between VE-cad and F-actin in JBL function is also supported by F-actin interference experiments. Blocking F-actin polymerization by latrunculin-B effectively inhibits JBL formation and those JBL, which do form, show decreased oscillation. Furthermore, junctional rings do not elongate during this treatment. Inhibition of Rac1 by NSC23766 treatment did not lead to obvious defects in JBL formation, but in a reduction in their oscillation frequency as well as a defect in junction elongation. During NSC23766 treatment JBL looked relatively normal. When using a EGFP-ZO1 reporter, we also observed “double



junctions”, indicating that JBL are able to form a distal junction and that Rac1 may be required during later stages of JBL function.

A recent study has shown that JAIL formation requires polarized Rac1 at endothelial cell junctions in HUVECs<sup>30</sup>. It is therefore surprising that Rac1 inhibition does not block formation of JBL in zebrafish embryos. It is possible that even at high doses, we do not achieve full Rac1 inhibition in vivo.

Alternatively, Rac1 may have a different function in JBL than in JAIL and formation of either protrusion may require different regulators.

Taken together, we have uncovered a hitherto non-described junction-based mechanism of active cell movements, which can be used by endothelial cell (and possibly other cell types) to rearrange and adapt their shape as needed. Inhibition of JBL

**Fig. 7** Truncation of Ve-cadherin inhibits both JBL and endothelial cell remodeling. **a** Images of anti-ZO1 immunostained junctions in *cdh5<sup>ubs25/+</sup>* and *cdh5<sup>ubs25/ubs25</sup>* embryos. Arrows point to medial site of the junction. **b** Quantitation of the medial and lateral junctional thickness, based on immunostaining for ZO1; *cdh5<sup>ubs25/+</sup>*, *n* = 44 junctions (17 embryos); *cdh5<sup>ubs25/ubs25</sup>*, *n* = 40 (11 embryos); wild-type *n* = 28 (9 embryos). Black lines are medians. Non-parametric Kruskal-Wallis statistical test was used. **c** Quantitation of the duration of JBL based on EGFP-UCHD signal; *cdh5<sup>ubs25/+</sup>*, *n* = 122 (8 embryos), *cdh5<sup>ubs25/ubs25</sup>* *n* = 103 (8 embryos) and wild-type *n* = 43 (3 embryos). All embryos carry the UAS:EGFP-UCHD transgene *Tg(fli:GFP<sup>ubs3</sup>;UAS:EGFP-UCHD<sup>ubs18</sup>)*. **d-l** *Tg(kdr:EGFP<sup>843</sup>)*; *cdh5<sup>ubs25/+</sup>* (**d-g**) and *Tg(kdr:EGFP<sup>843</sup>)*; *cdh5<sup>ubs25/ubs25</sup>* (**h-k**) embryos stained for VE-cadherin (rabbit antibody, green) and ZO1 (red). Individual channels are shown in inversed contrast. Both wild-type and mutant VE-cad show junctional localization (solid arrow in panels **d, f, h, and j**). The junctional gap in the VE-cadherin staining of a SeA in a mutant embryo (*cdh5<sup>ubs25/ubs25</sup>*) is marked with dashed double arrow in panel **h**. **l** Quantification of the length of junctional gaps in control (*cdh5<sup>ubs25/+</sup>*, *n* = 72 gaps, 23 embryos) and mutant (*cdh5<sup>ubs25/ubs25</sup>*, *n* = 139 gaps, 33 embryos) embryos. Black lines are medians. Non-parametric Mann-Whitney statistical test was used. **m** Still images from a confocal time-lapse of endothelial nuclei (*Tg(kdr:nsEGFP<sup>ubs1</sup>)*) in wild-type or *cdh5<sup>ubs25/ubs25</sup>* embryos during SeA formation. T tip cell, S1 stalk cell 1, S2 stalk cell 2; double-headed arrow indicates the distance of S1 and S2 nuclei. **n** Quantification of movement of stalk cell 1 (S1) nuclei in relation to stalk cell 2 (S2) nuclei during cell rearrangements in SeA; *cdh5<sup>ubs25/+</sup>*, *n* = 22 SeA (4 embryos); *cdh5<sup>ubs25/ubs25</sup>*, *n* = 17 SeA (4 embryos); wild-type *n* = 20 SeA (4 embryos). Black lines are medians. Non-parametric Kruskal-Wallis statistical test was used. Scale bars 5  $\mu$ m (**a**), 10  $\mu$ m (**d, h, m**)

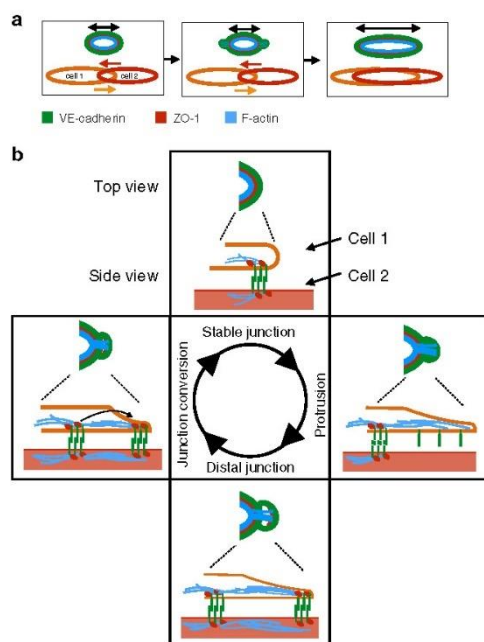


**Fig. 8** A Ratchet-like molecular mechanism of junction remodeling. **a** Stepwise elongation of an endothelial cell junction during anastomosis. As two endothelial cells move over each other (bottom), the junction becomes elongated. The three proteins investigated in this study are indicated in different colors. **b** Proposed oscillatory mechanism of JBL function. A single cycle is depicted. F-actin protrusions emanate distally from a stable junction. These protrusions also contain diffuse VE-cadherin, but not ZO1. At the distal end of the protrusion, F-actin, ZO1 and VE-cadherin are components of a newly formed junction with VE-cadherin-mediated contact to the underlying cell. Eventually, dynamic F-actin remodeling pulls the proximal junction towards the new junction

function blocks these processes and results in a failure to form multi-cellular tubes and prevents formation of a patent vasculature. The salient feature of our proposed JBL model is that endothelial cells use each other as migratory substrates via VE-cadherin. Our model suggests that VE-cadherin provides an extracellular clutch, by generating an intercellular adhesion patch,

which serves as an anchor for intracellular actomyosin contractions. This cell-cell interaction may be analogous to integrin-ECM-based adhesion patches of classical lamellipodia. Furthermore, these VE-cadherin adhesion complexes give rise to a distal junction with an underlying F-actin arc. Similar F-actin arcs have been described to be essential for the function of lamellipodia during migration of human endothelial cells (HUVECs) in vitro<sup>31</sup>. Future studies will aim to uncover the exact mechanisms of traction force generation and transmission during JBL-driven junction elongation. While F-actin dynamics are essential for junction elongation, we have never observed prominent stress fibers in this process, suggesting that F-actin-based traction forces are acting locally rather than over the longitudinal extent of the endothelial cells.

Although we have focused our studies on JBL formation and function in the process of blood vessel anastomosis, we observed JBL also within larger caliber vessels such as the dorsal aorta at stages, when endothelial cells are extensively rearranging and undergoing cell shape changes<sup>21</sup>. Our studies therefore indicate that endothelial cells employ JBL as a general means for rearrangements and shape changes during blood vessel assembly and vascular remodeling. Using interendothelial adhesion for force transmission allows dynamic endothelial activities while maintaining the vascular seal. We therefore envision that JBL may underlie many morphogenetic endothelial cell behaviors during blood vessel expansion, normalization, regression and endothelial shear stress response. Remodeling and reorganization of adherens junctions is essential for developmental morphogenesis<sup>32,33</sup>. Whether similar JBL occur also in different tissues, besides vasculature and endothelial cells, remains to be elucidated.

## Methods

**Fish strains and maintenance.** Maintenance of fish and experimental procedures involving zebrafish embryos were carried out at the Biozentrum/Universität Basel according to Swiss national guidelines of animal experimentation (TSchV). Zebrafish lines were generated and maintained under licenses 1014H and 1014G1 issued by the Veterinäramt-Basel-Stadt. Fish strains carrying following transgenes and mutations were used in this study: *kdr:EGFP<sup>843</sup>*<sup>34</sup>, *VE-cad-Venus* (*BAC(cdh5:cdh5-TS)*, *fli:GFP<sup>ubs3</sup>*<sup>19</sup>, *UAS:EGFP-hZO1<sup>ubs19</sup>*, *UAS:EGFP-UCHD<sup>ubs18</sup>*<sup>13</sup>, *UAS:mRuby2-UCHD<sup>ubs20</sup>* (this study), *UAS:mClav2-UCHD<sup>ubs27</sup>* (this study), *UAS:mRFP<sup>85</sup>*, *cdh5<sup>ubs25</sup>* (this study), and *Tg(kdr:EGFP<sup>ubs1</sup>)<sup>ubs1</sup>*<sup>36</sup>. The fish were maintained using standard procedures and embryos obtained via natural spawning<sup>37</sup>.

**Generation of transgenic fish lines.** The EGFP sequence of pT24xnrUAS:EGFP-UCHD was replaced by the sequence of mRuby2 (amplified from pcDNA3-mRuby2 was a gift from Michael Lin; Addgene plasmid #40260)<sup>38</sup> or by the sequence of mClav2 (amplified from pmClavGR2-NT; Allele Biotechnology) to generate the final plasmids pT24xnrUAS:mRuby2-UCHD and pT24xnrUAS:mClav2-UCHD respectively. These final plasmids were injected individually, together with *tol2* RNA into *Tg(fli:Gal4ff)*<sup>ubs3</sup> embryos and that were raised to adulthood and eventually stable transgenic fish lines *Tg(UAS:mRuby2-UCHD)<sup>ubs20</sup>* and *Tg(UAS:mClav2-UCHD)<sup>ubs27</sup>* were isolated and maintained.

**Transient expression of mCherry-ZO1 in zebrafish embryos.** To transiently express mCherry-ZO1 in endothelial cells of zebrafish embryo, ~50 pg of plasmid *file:mCherry-ZO1*<sup>39</sup> was injected together with Tol2-transposase mRNA into 1–4 cell stage embryos (*Tg(BAG(adh5:adh5-ts))*). Twenty-four hours after injection healthy embryos expressing mCherry were selected, mounted in low-melting point agarose and imaged using Leica SP5 confocal microscope.

**Generation of ve-cadherin mutants.** The ve-cadherin truncation allele (*adh5<sup>ubs25</sup>*) was generated using CRISPR/CAS technology<sup>40</sup>. We sequenced exon 12 of *adh5* (encoding the cytoplasmic domain) of ABC, Tübingen (TU) and tupfel:long-fin (TL) strains and found a potential target sequence in ABC (5'-GGGACCTGCACTCTATGCCATGG-3'). Target guide RNA and Cas9 protein were synthesized by standard procedures<sup>40</sup> and co-injected into ABC/TU embryos. Offspring of G0 fish containing germline mutations were screened by PCR analysis for the loss of a *NcoI* restriction site, which is present on the wild-type allele. For subsequent genotyping, multiplex PCR was performed using allele-specific primers:

VE-cad-fwd: 5'-GAAACCCATATCAACAGACCTGC-3',  
VE-cad-rev: 5'-CAGAGCCGCTACTCCATAAAGC-3',  
VE-cad-ubs25-fwd: 5'-GACCTGCACTCTATGGAA-3',  
VE-cad-wild-type-rev: 5'-GCAGGAGGTTTCTTACC-3'.

The genotyping protocol of *adh5<sup>ubs25</sup>* has been described earlier<sup>13</sup>. Following primers were used:

cdh5-FWD: 5'-TTGGTGAAGTCAACAATGGGG-3'  
cdh5-REV: 5'-ACAGTCCTGGGTTTACCATTGGG-3'  
cdh5-WT-FWD: 5'-ATCCCGTTTTCGATCTGAC-3'  
cdh5-ubs8-REV: 5'-CTGATGGATCCAGATTGGAATC-3'

**Live imaging of zebrafish embryos.** Embryos were anesthetized using Tricaine (MS-222, 160 mg l<sup>-1</sup>, #E10521 Sigma-Aldrich) and embedded in 0.7% low-melting point agarose (Sigma-Aldrich) supplemented with Tricaine in glass-bottom dish. After the agarose solidified, it was overlaid with E3-medium supplemented with Tricaine. All the imaging was performed at 28.5 °C. The imaging was performed using Leica SP5 Matrix confocal microscope equipped with resonance scanner using ×63 NA 1.2 or ×40 NA 1.1 water immersion objectives. For imaging of JBL, the time points were 60–120 s intervals and in case of double-color imaging, 12–60 s.

For the pharmacological experiments, the treatment of embryos with inhibitors (DMSO 1%, Latrunculin B (150 ng ml<sup>-1</sup>), NSC23766 (300–900 μM)) begun 1 h prior to embedding into low-melting point-agarose and confocal imaging. The inhibitors were present throughout the whole experiment.

**Generation of polyclonal rat anti-zf-VE-CAD antibodies.** A cDNA fragment encoding a polypeptide comprising the extracellular domain of zebrafish VE-cad (Ala22 to Lys464) was expressed in *E. coli* using the T7 expression system. The protein was purified on Ni-charged IMAC resin (BioRad) under denaturing conditions. Antiserum was raised in rats by ThermoFisher Scientific using standard immunization procedures.

**Immunofluorescence analysis.** Embryos were fixed with 2% paraformaldehyde (Electron Microscopy Sciences) in PBST (PBS + 0.1% Tween-20) at room temperature for 90 min, and immunostained using following protocol: Fixation with 2% PPA/PBST (PBS + 0.1% Tween-20) for 90 min at room temperature followed by washes with PBST. After permeabilization (PBST + 0.5% Triton X-100, 30 min), the samples were blocked (PBST + 0.1% Triton X100 + 10% normal goat serum + 1% BSA + 0.01% Sodium Azide, overnight, 4 °C). Subsequently, primary antibodies were added (diluted in Pierce Immunostain enhancer, #46644, ThermoFisher Scientific) and incubated overnight at 4 °C. After several washes with PBST at room temperature, the secondary antibodies were added (1:2000 dilution in Pierce staining Enhancer) and incubated overnight at 4 °C. After several washes with PBST at room temperature, the embryos were mounted onto glass-bottom dishes using low-melting point agarose.

Mouse anti-hZO1 (dilution 1:400, Invitrogen #33-9100; use in zebrafish in ref. <sup>36</sup>), rat anti-VE-cad (dilution 1:500) and rabbit anti-VE-cad (dilution 1:500) primary antibodies were used. Rat anti-VE-cad was validated by immunofluorescence by using *ve-cad* null mutant (*adh5<sup>ubs8</sup>, Tg(kdhl:EGFP<sup>843</sup>)*) embryos<sup>13</sup> as control for specificity (Supplementary Fig. 2). Rabbit anti-VE-cad has been described and validated previously<sup>36</sup> and also validated with *ve-cad* null mutants<sup>13</sup>. Fluorescent secondary antibodies Alexa-568 goat anti-mouse IgG, Alexa-633 goat anti-rat IgG, and Alexa-633 goat anti-rabbit IgG (all from Invitrogen) were used.

**Photoconversion experiment.** Twenty-four hours post fertilization zebrafish embryos (*Tg(Fli:GFP<sup>ubs3</sup>, UAS:mClav2-UCHD<sup>ubs27</sup>)*) were embedded in 0.7% low-melting point agarose onto 35 mm glass bottom dishes. Tip cells of vascular sprouts of segmental arteries were photoconverted on a Leica SP5 confocal microscope using a ×40 NA 1.1 water immersion objective. Photoconversion was performed with a 405 nm laser (20% power) until no further increase in converted UCHD-mClav2 signal was observed (conversion time 10–30 s). After this the embryos were allowed to develop for ~4 h before imaging of anastomosis events in DLAV.

**Junction elongation experiment.** Junctional elongation was analyzed by observing anastomosis and elongation of isolated junctional rings during DLAV formation. Inhibitor treatments Latrunculin B (150 ng ml<sup>-1</sup>), NSC23766 (300–900 μM) or DMSO (1%) were applied 1 h before mounting of embryos into 0.7% low-melting point agarose and imaging the junctions for 1–2 h on a Leica SP5 (×40 NA 1.1 water immersion objective).

**Cell rearrangement experiment.** Embryos carrying nuclear GFP (*Tg(kdhl:EGFP<sup>ubs1</sup>)*) were used. Confocal Z-stacks were obtained as described above in 12–14 min intervals. To control small variations in the developmental phases of the individual SeA,  $t = 0$  min was the time point when tip cell had reached the dorsal side and started to sprout in anteroposterior directions. The endpoint for analysis was 10 time points later ( $t = 10; 120–140$  min). At  $t = 0$  and  $t = 10$  the distance ( $d$ ) of stalk cell S1 and S2 was measured using Fiji. Speed of movement of S1 and S2 in relative to each other was calculated using equation:

$$\text{speed} = \frac{|d_{t0} - d_{t10}|}{\Delta t} \quad (1)$$

**Image analysis and preparation.** Image analysis and measurements were performed using Fiji. Deconvolution was performed using Huygens Remote Manager software<sup>41</sup>. Maximum Z-projections were used. Noise was reduced using Gaussian filtering (radius 1.0) and background subtracted (rolling ball radius 50) using Fiji. Contrast and brightness of images were linearly adjusted. Kymographs were generated from the sum Z-projections of time-lapse series using Fiji. Perpendicular straight line across the junction was drawn and kymograph generated using reslice tool. Colocalization analysis was performed using Fiji. First, background was subtracted (rolling ball radius 25), regions of interests (ROIs) of separate cell-cell junctions were selected and then colocalization analysis was done on these ROIs using Colocalization Test plugin with Fay image randomization ((written by Tony Collins, McMaster University, Hamilton, Canada). Publication figures were prepared using Fiji, OMERO Fig. and Adobe Illustrator.

**Statistical analyses.** Statistical analyses were performed using Microsoft Excel, IBM SPSS statistics 22 and GraphPad Prism version 6.05 for Windows software. Non-parametric two-sided Kruskal–Wallis  $H$ -test, Mann–Whitney  $U$ -test and binomial probability (photoconversion experiments, test probability 0.5) were used. The data reasonably met the assumptions of the tests. In Fig. 1e, f, where the data was non-normal and heteroscedastic similar  $p$ -values were obtained with Kruskal–Wallis  $H$ -test, Welch's  $t$ -test and median test.

No statistical power analysis was used to determine sample size. Systematic randomization was not used. Experiments with *adh5<sup>ubs25</sup>* (Fig. 7) were performed essentially blinded as the genotype was determined after data capture and analysis. In all other experiments blinding was not used. Samples of low technical quality were excluded from the subsequent analyses. In all figures (exception Fig. 2f and Supplementary Fig. 3d) the individual data points are plotted and median indicated with horizontal line as has been recommended<sup>42</sup>. In Fig. 2f, Supplementary Fig. 1a and c, the data are binned and the number of events in the given bin is plotted.

To formally analyze periodicity of F-actin intensity fluctuations, we calculated the autocorrelation function (ACF) using IBM SPSS statistics 22 software. Next, we analyzed the level of noise in the fluctuations (phase diffusion) that gradually reduces the oscillation of the ACF. To quantify this effect, we fitted each of the ACFs using a sinusoidal function enveloped by an exponential decay using Igor Pro 6.37 (WaveMetrics Inc, Lake Oswego, OR, USA). The function used was:

$$\text{ACF}(t) = A \times \sin(f \times t + \theta) \times e^{-t/\tau} \quad (2)$$

where  $t$  is the lagtime of the ACF,  $A$  is amplitude,  $f$  the frequency,  $\theta$  is the phase, and  $\tau$  is the characteristic lifetime of the decay.

#### Data availability

The data that support the findings of this study are available from the corresponding authors upon reasonable request.

Received: 7 April 2017 Accepted: 26 July 2018

Published online: 31 August 2018

#### References

- Carmeliet, P. Angiogenesis in health and disease. *Nat. Med.* **9**, 653–660 (2003).
- Potente, M., Gerhardt, H. & Carmeliet, P. Basic and therapeutic aspects of angiogenesis. *Cell* **146**, 873–887 (2011).
- Betz, C., Lenard, A., Belting, H.-G. & Affolter, M. Cell behaviors and dynamics during angiogenesis. *Development* **143**, 2249–2260 (2016).



4. Schuermann, A., Helker, C. S. M. & Herzog, W. Angiogenesis in zebrafish. *Semin. Cell. Dev. Biol.* **31**, 106–114 (2014).
5. Wacker, A. & Gerhardt, H. Endothelial development taking shape. *Curr. Opin. Cell Biol.* **23**, 676–685 (2011).
6. Christ, B., Poelmann, R. E., Mentink, M. M. & Gittenberger-de Groot, A. C. Vascular endothelial cells migrate centripetally within embryonic arteries. *Anat. Embryol.* **181**, 333–339 (1990).
7. Sato, Y. et al. Dynamic analysis of vascular morphogenesis using transgenic quail embryos. *PLoS ONE* **5**, e12674 (2010).
8. Lamallice, L., Le Boeuf, F. & Huot, J. Endothelial cell migration during angiogenesis. *Circ. Res.* **100**, 782–794 (2007).
9. Michaelis, U. R. Mechanisms of endothelial cell migration. *Cell. Mol. Life Sci.* **71**, 4131–4148 (2014).
10. Jakobsson, L. et al. Endothelial cells dynamically compete for the tip cell position during angiogenic sprouting. *Nature* **12**, 943–953 (2010).
11. Bentley, K. et al. The role of differential VE-cadherin dynamics in cell rearrangement during angiogenesis. *Nature* **16**, 309–321 (2014).
12. Perryn, E. D., Czirik, A. & Little, C. D. Vascular sprout formation entails tissue deformations and VE-cadherin-dependent cell-autonomous motility. *Dev. Biol.* **313**, 545–555 (2008).
13. Sauter, L. et al. Cdh5/VE-cadherin promotes endothelial cell interface elongation via cortical actin polymerization during angiogenic sprouting. *Cell Rep.* **9**, 504–513 (2014).
14. Xu, C. et al. Arteries are formed by vein-derived endothelial tip cells. *Nat. Commun.* **5**, 5758 (2014).
15. Franco, C. A. et al. Dynamic endothelial cell rearrangements drive developmental vessel regression. *PLoS Biol.* **13**, e1002125 (2015).
16. Dejana, E., Tournier-Lasserre, E. & Weinstein, B. M. The control of vascular integrity by endothelial cell junctions: molecular basis and pathological implications. *Dev. Cell* **16**, 209–221 (2009).
17. Harris, T. J. C. & Tessier, U. Adherens junctions: from molecules to morphogenesis. *Nat. Rev. Mol. Cell Biol.* **11**, 502–514 (2010).
18. Legendijk, A. K. & Hogan, B. M. VE-cadherin in vascular development: a coordinator of cell signaling and tissue morphogenesis. *Curr. Top. Dev. Biol.* **112**, 325–352 (2015).
19. Herwig, L. et al. Distinct cellular mechanisms of blood vessel fusion in the zebrafish embryo. *Curr. Biol.* **21**, 1942–1948 (2011).
20. Lenard, A. et al. In vivo analysis reveals a highly stereotypic morphogenetic pathway of vascular anastomosis. *Dev. Cell* **25**, 492–506 (2013).
21. Legendijk, A. K. et al. Live imaging molecular changes in junctional tension upon VE-cadherin in zebrafish. *Nat. Commun.* **8**, 1402 (2017).
22. Coué, M., Brenner, S. L., Spector, I. & Korn, E. D. Inhibition of actin polymerization by latrunculin A. *FEBS Lett.* **213**, 316–318 (1987).
23. Gao, Y., Dickerson, J. B., Guo, P., Zheng, J. & Zheng, Y. Rational design and characterization of a Rac GTPase-specific small molecule inhibitor. *Proc. Natl Acad. Sci. USA* **101**, 7618–7623 (2004).
24. Sauter, L., Affolter, M. & Belting, H.-G. Distinct and redundant functions of Esam and VE-cadherin during vascular morphogenesis. *Development* **144**, 1554–1565 (2017).
25. Ridley, A. J., Paterson, H. F., Johnston, C. L., Diekmann, D. & Hall, A. The small GTP-binding protein rac regulates growth factor-induced membrane ruffling. *Cell* **70**, 401–410 (1992).
26. Friedl, P. & Mayor, R. Tuning collective cell migration by cell–cell junction regulation. *Cold Spring Harb. Perspect. Biol.* **9**, a029199 (2017).
27. Mayor, R. & Etienne-Manneville, S. The front and rear of collective cell migration. *Nat. Rev. Mol. Cell Biol.* **17**, 97–109 (2016).
28. Cai, D. et al. Mechanical feedback through E-cadherin promotes direction sensing during collective cell migration. *Cell* **157**, 1146–1159 (2014).
29. Abu Taha, A., Taha, M., Seebach, J. & Schnitfler, H.-J. ARP2/3-mediated junction-associated lamellipodia control VE-cadherin-based cell junction dynamics and maintain monolayer integrity. *Mol. Biol. Cell* **25**, 245–256 (2014).
30. Cao, J. et al. Polarized actin and VE-cadherin dynamics regulate junctional remodelling and cell migration during sprouting angiogenesis. *Nat. Commun.* **8**, 2210 (2017).
31. Burnette, D. T. et al. A role for actin arcs in the leading-edge advance of migrating cells. *Nature* **13**, 371–381 (2011).
32. Nishimura, T. & Takeichi, M. Remodeling of the adherens junctions during morphogenesis. *Curr. Top. Dev. Biol.* **89**, 33–54 (2009).
33. Takeichi, M. Dynamic contacts: rearranging adherens junctions to drive epithelial remodelling. *Nat. Rev. Mol. Cell Biol.* **15**, 397–410 (2014).
34. Jin, S.-W., Beis, D., Mitchell, T., Chen, J.-N. & Stainier, D. Y. R. Cellular and molecular analyses of vascular tube and lumen formation in zebrafish. *Development* **132**, 5199–5209 (2005).
35. Asakawa, K. et al. Genetic dissection of neural circuits by Tol2 transposon-mediated Gal4 gene and enhancer trapping in zebrafish. *Proc. Natl Acad. Sci. USA* **105**, 1255–1260 (2008).
36. Blum, Y. et al. Complex cell rearrangements during intersegmental vessel sprouting and vessel fusion in the zebrafish embryo. *Dev. Biol.* **316**, 312–322 (2008).
37. Westerfield, M. *The Zebrafish Book: A Guide for the Laboratory Use of Zebrafish Danio rerio* (University of Oregon Press, Eugene, 2000).
38. Lam, A. J. et al. Improving FRET dynamic range with bright green and red fluorescent proteins. *Nat. Methods* **9**, 1005–1012 (2012).
39. Phng, L.-K., Stanchi, F. & Gerhardt, H. Filopodia are dispensable for endothelial tip cell guidance. *Development* **140**, 4031–4040 (2013).
40. Gagnon, J. A. et al. Efficient mutagenesis by Cas9 protein-mediated oligonucleotide insertion and large-scale assessment of single-guide RNAs. *PLoS ONE* **9**, e98186 (2014).
41. Ponti, A., Schwarz, P., Gulati, A. & Bäcker, V. Huygens remote manager: a web interface for high-volume batch deconvolution. *Imaging Microsc.* **9**, 57–58 (2007).
42. Weissgerber, T. L., Milic, N. M., Winham, S. J. & Garovic, V. D. Beyond bar and line graphs: time for a new data presentation paradigm. *PLoS Biol.* **13**, e1002128 (2015).

**Acknowledgements**

We thank Kumuthini Kulendra for fish care and the Imaging Core Facility of the Biozentrum (University of Basel) for microscopy support. We thank Johanna Ivaska for support and acknowledge Zebrafish Core Facility (Turku Centre for Biotechnology, University of Turku and Abo Akademi University). This work has been supported by the Kantons Basel-Stadt and Basel-Land and by a grant from the Swiss National Science Foundation to M.A. I.P. was supported by a post-doctoral fellowship from the Finnish Cultural Foundation and Foundations' Post-Doc Pool. M.L., C.W., and L.S. were supported by a Fellowship of Excellence, Biozentrum, University of Basel.

**Author contributions**

H.G.B., I.P., and M.A. conceived the idea and directed the work. I.P. and H.G.B. designed the experiments. I.P., L.S., M.L., C.W., and D.H. performed experiments. D.B., A.K.L., and B.M.H. provided unpublished reagents. C.G. helped with data analysis. I.P. and H.G.B. wrote the manuscript. All authors reviewed the manuscript.


**Additional information**

**Supplementary Information** accompanies this paper at <https://doi.org/10.1038/s41467-018-05851-9>.

**Competing interests:** The authors declare no competing interests.

**Reprints and permission information** is available online at <http://npg.nature.com/reprintsandpermissions/>

**Publisher's note:** Springer Nature remains neutral with regard to jurisdictional claims in published maps and institutional affiliations.

 **Open Access** This article is licensed under a Creative Commons Attribution 4.0 International License, which permits use, sharing, adaptation, distribution and reproduction in any medium or format, as long as you give appropriate credit to the original author(s) and the source, provide a link to the Creative Commons license, and indicate if changes were made. The images or other third party material in this article are included in the article's Creative Commons license, unless indicated otherwise in a credit line to the material. If material is not included in the article's Creative Commons license and your intended use is not permitted by statutory regulation or exceeds the permitted use, you will need to obtain permission directly from the copyright holder. To view a copy of this license, visit <http://creativecommons.org/licenses/by/4.0/>.

© The Author(s) 2018

## 8.2 Building the complex architectures of vascular networks: Where to branch, where to connect and where to remodel?

Yin J, **Heutschi D**, Belting HG, Affolter M.

[Curr Top Dev Biol. 2021; PMID: 33820624](#)

I commented and proofread the manuscript and prepared figures to illustrate the processes described in the review. In the end it was decided to keep the review short and not to include the figures.

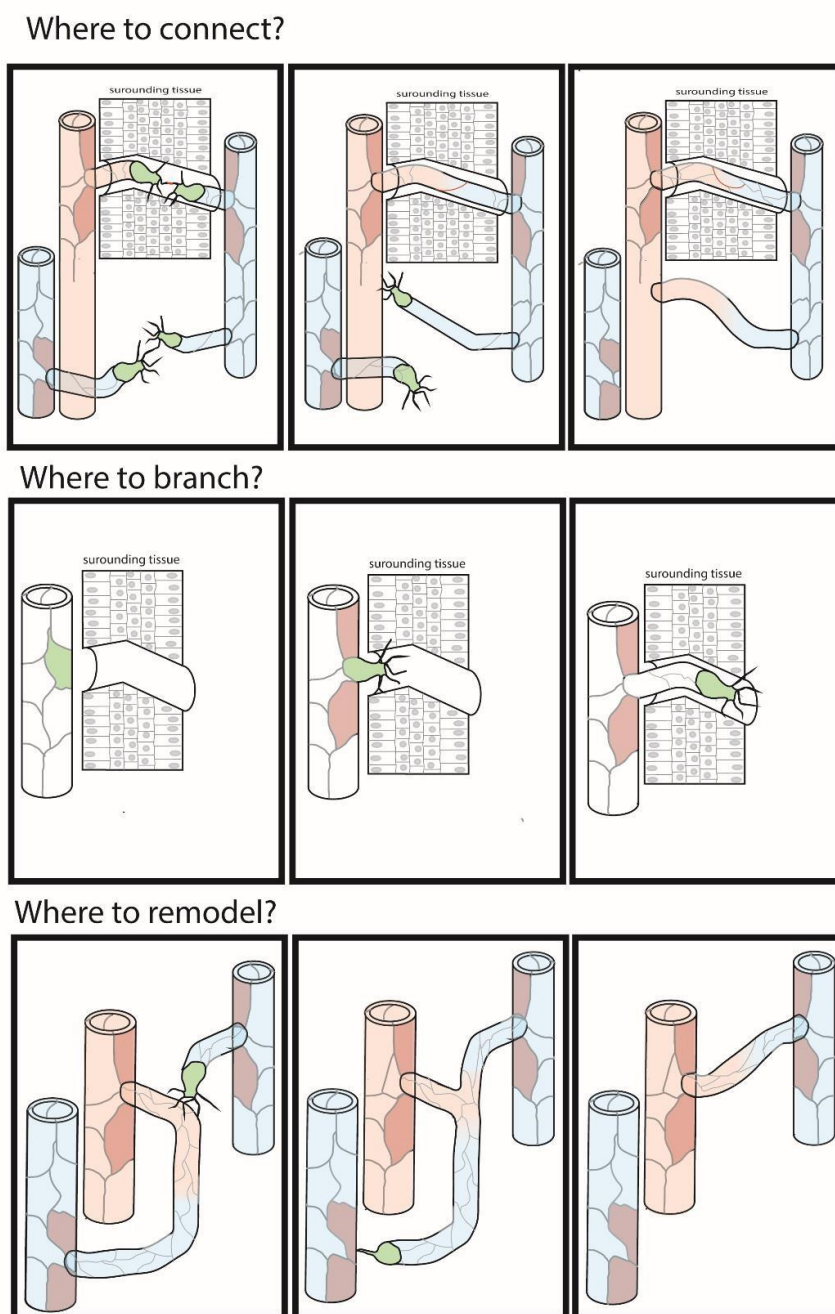


Figure 22 Preview of the prepared figures for the review



# Building the complex architectures of vascular networks: Where to branch, where to connect and where to remodel?

Jianmin Yin, Daniel Heutschi, Heinz-Georg Belting, and Markus Affolter\*

Biozentrum der Universität Basel, Basel, Switzerland

\*Corresponding author: e-mail address: markus.affolter@unibas.ch

## Contents

1. Introduction	282
2. Where to branch: Generating new branches via sprouting	284
3. Where to connect: Formation of an interconnected network via anastomosis	288
4. Where to remodel: Optimizing flow in vascular networks via pruning	292
5. Concluding remarks and outlook	293
References	294

## Abstract

The cardiovascular system is the first organ to become functional during vertebrate embryogenesis and is responsible for the distribution of oxygen and nutrients to all cells of the body. The cardiovascular system constitutes a circulatory loop in which blood flows from the heart through arteries into the microvasculature and back through veins to the heart. The vasculature is characterized by the heterogeneity of blood vessels with respect to size, cellular architecture and function, including both larger vessels that are found at defined positions within the body and smaller vessels or vascular beds that are organized in a less stereotyped manner. Recent studies have shed light on how the vascular tree is formed and how the interconnection of all branches is elaborated and maintained. In contrast to many other branched organs such as the lung or the kidney, vessel connection (also called anastomosis) is a key process underlying the formation of vascular networks; each outgrowing angiogenic sprout must anastomose in order to allow blood flow in the newly formed vessel segment. It turns out that during this “sprouting and anastomosis” process, too many vessels are generated, and that blood

flow is subsequently optimized through the removal (pruning) of low flow segments. Here, we reflect on the cellular and molecular mechanisms involved in forming the complex architecture of the vasculature through sprouting, anastomosis and pruning, and raise some questions that remain to be addressed in future studies.



## 1. Introduction

Living structures of a branched nature have fascinated scientists for many decades. Branching is a common feature in the plant kingdom and the most prominent aspect of the visual appearance of flowers and trees. The branching pattern of leaves and twigs is often species-specific, and therefore can serve for systematic classification. In the animal kingdom, branched organs are not readily visible since branching occurs in internal tissues such as the vasculature, the lung, the kidney and many different glands. In insects, branching is observed in the trachea, an ancient respiratory system. In general, organ branching facilitates either transport to all cells of the organism (e.g., trachea and vasculature), and/or increases the surface area for efficient gas and liquid exchange (e.g., lung, kidney, pancreas). Branching of such structures in animals is usually achieved during development, and how distinct branching patterns arise has been an interesting topic of research, even more so since biological sciences have advanced at the cellular and molecular level in the past decades.

Many branched organs occupy a limited area within the body (such as the lung, the kidney and many glands) and the underlying branching pattern are organ-specific and in part genetically determined (Goodwin & Nelson, 2020; see other articles in this issue). In contrast, the vasculature needs to provide oxygen and nutrition to all cells in the body, and thus needs to adapt, both structurally and functionally, to each developing body part while remaining connected to the major transport routes, the larger arteries and veins. From an outsider's view, one would thus think that the branching pattern, and ultimately the overall anatomy of the vasculature, is established in response to instructions obtained from the tissue environment, which dictates specific, stereotypical vascular branching patterns. This is likely the case for larger arteries and veins, which often represent a highly similar anatomy in different individuals of the same species. For example, there are fixed branching sites, branching angles, vessel curvature and size gradation from the aorta for arteries supplying the head, internal organs and legs and arms (Fig. 1) (Horowitz & Simons, 2008). This is not the case for vascular beds made up of smaller vessels, such as the microvasculature.



**Fig. 1** Corrosion preparation of a human head. The large arteries towards the head are colored with different plastic materials. Picture obtained from Magdalena Müller-Gerbl from the Anatomical Museum of the University of Basel. Note that the microvasculature is not visible in these preparations.

Since the vasculature is a closed circulatory network, mechanisms that lead to the complete interconnection of temporary “dead ends” must exist. Several mechanisms underlying the development of the vasculature help to assure this interconnection. In most cases, new branches arise via budding from existing branches through a process called sprouting angiogenesis, thereby maintaining a connection to the initial functional network right from the onset of the formation of new structures. Sprouts extend until they reach other blunt-ended sprouts or already functional branches, connect to these in a process called anastomosis, and thereby form novel, interconnected loops. Vessels with reduced or no flow are eventually pruned and disappear; no blunt-ended branches persist in the mature vasculature, in sharp contrast to most other branched structures, including the lymphatic vasculature, which are made up of blunt-ended tubes.

Here, we would like to briefly address the following questions regarding the development of the vasculature. (1) *Where do new branches arise, or in*

other words, how is the branching pattern determined? And how is branch formation directed (or limited) to defined positions to give rise to a conserved vascular anatomy? (2) *Where do branches connect*, or in other words, how do circulatory loops form? Do sprouts simply connect upon contact between endothelial cells (ECs), or are there mechanisms that control the specificity of branch connections to ensure specific architectural features? (3) *Where do vessel segments prune*, or in other words, how is the ultimate vascular network established? Recent genetic and molecular analyses have started to provide a more detailed view of vascular branching, but many intriguing questions remain to be investigated in the future.

This essay is not a comprehensive review of the existing literature, but rather is based on a selection of a few examples presenting answers to the questions raised above. In many places, we refer the reader to excellent reviews on the topics discussed.



## 2. Where to branch: Generating new branches via sprouting

While the primary axial blood vessels, which make up the initial circulatory loop, are formed by vasculogenesis, the majority of blood vessels are formed by sprouting angiogenesis, the formation of new branches out of existing vessels (Hogan & Schulte-Merker, 2017; Potente, Gerhardt, & Carmeliet, 2011). At the cellular level, angiogenesis is accomplished by many different morphogenetic mechanisms brought about by distinct endothelial cell (EC) behaviors including polarization, proliferation, migration, rearrangement and lumen formation (Campinho, Vilfan, & Vermot, 2020; Fonseca, Barbacena, & Franco, 2020; Okuda & Hogan, 2020; Szymborska & Gerhardt, 2018). The locations at which new branches arise via sprout formation is tightly controlled in the initial phases of vascular development in the embryo and assures that each developing organ, body part or body segment is appropriately connected to the initial vascular loop. The rather strict spatial control of sprouting is reflected in the observation that the vascular network of individuals of the same species is almost identical with respect to the larger vessels (which in many cases form early during development), allowing a conserved nomenclature of individual vessels; the stereotypic anatomical organization of the vasculature is even shared by different vertebrate species and has allowed to use a common nomenclature in mammals and fish (discussed by Isogai, Horiguchi, & Weinstein, 2001).

How can sprouts be initiated at specific places in an existing vessel in a manner which is identical in different individuals? A striking situation in which the formation of such conserved vasculature patterns can be studied are the intersegmental vessels (ISVs), which develop very early during embryogenesis and eventually form segmental structure reiterated along the body axis in vertebrates. In the last few years, much has been learned about how the angiogenic sprouts of the ISVs are restricted to specific locations along the dorsal aorta (DA) in the zebrafish embryo (see Fig. 2; reviewed in Vila Ellis et al., 2020).

ISVs are formed upon the induction of endothelial tip cells in the DA. Angiogenic sprouts initially consist of a leading tip cell with exploratory filopodia which migrates alongside intersomitic boundaries. These tip cells migrate dorsally, followed by stalk cells, until they eventually form extensions along the anterior-posterior axis above the dorsal side of the neural tube and anastomose with tip cells of neighboring sprouts to form the dorsal longitudinal anastomotic vessel (DLAV). Sprouting is induced by Vegf ligands from the surrounding somites via the initiation of VegfR2 signaling in EC and the activation of the downstream targets Erk kinase (Shin et al., 2016) and Plcg1 (Lawson, Mugford, Diamond, & Weinstein, 2003).

Notch (N)-Delta (Dll) signaling plays a key role in singling out individual tip cells leading to sprout formation at specific locations along the dorsal aorta. It has been shown that Dll4/N signaling is required for the selection of single tip cells during the budding process, and that Dll4 expression in tip cells suppresses tip cell behavior in adjacent cells in the DA via N (Eilken & Adams, 2010; Herbert & Stainier, 2011; Jakobsson, Bentley, & Gerhardt, 2009; Siekmann, Affolter, & Belting, 2013). In an elegant and more recent study, it was shown that this process can be monitored via endothelial Ca<sup>2+</sup> oscillations and is rather dynamic as tip cells start to migrate out of the DA and inhibit neighboring cells from adopting the same fate (Yokota et al., 2015).

As angiogenic sprouts grow out from the DA, they need to be guided along the correct path to the dorsal side of the embryo. PlexinD1, which is encoded by the gene *out of bounds* (*obd*; Torres-Vázquez et al., 2004), is expressed in ECs and is required for pathway selection; in *obd* mutants, ISVs fail to follow their normal pathway leading to a non-stereotypic and highly aberrant pattern of ISVs. The ligands of PlexinD1, Semaphorin3a and 3b, are expressed in the somites and repel the angiogenic sprouts such that they follow the somite boundaries. The segmental organization of the

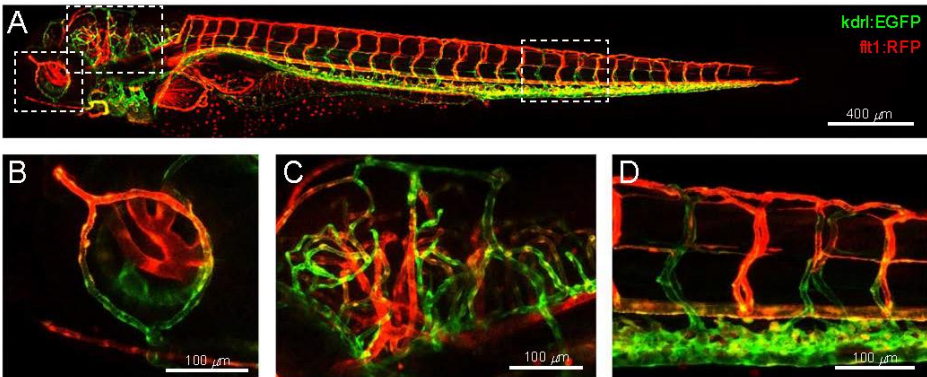


**Fig. 2** (A) Confocal imaging of a 4 days old zebrafish embryo. Using markers for arterial vessels (*flt1*:RFP, red) and venous vessels (*kdr1*:EGFP, green), the complex architecture of a living zebrafish embryo can be visualized. (B) Eye. (C) Hindbrain. (D) ISVs. Note the segmentally repeated organization of the intersegmental vessels (ISVs) in the trunk vasculature.



trunk by a series of somites, which express Vegfs and Semaphorins, thereby sets up the segmental vascular pattern by combining a global pro-angiogenic signal with a metamerically repellent activity.

*obd* mutants also display an increased number of tip cells emerging from the DA. It thus appears that PlexinD1 signaling, in addition to restricting the migratory path of tip cells, also restricts the angiogenic potential along the DA, and it appears to do so via the transcriptional upregulation of the soluble version of Flt1 (sFlt1), thereby downregulating Vegf signaling in inappropriate places (Zygmunt et al., 2011). There are thus several molecular mechanisms ensuring that sprouts are exclusively formed at very specific locations and migrate along certain routes (between the somites in this particular case), thereby determining the architecture of the branching pattern of the ISVs in the vertebrate trunk. Similar mechanisms appear to be used in other places, as it has been shown that Vegfs and sFlt1 are also involved in the organization of trunk vessels around the spinal cord (Matsuoka et al., 2016; Wild et al., 2017).

Compared to the conserved metamerically pattern in the zebrafish trunk, the vasculature of the brain appears more complex and heterogeneous in the different brain regions. Nevertheless, formation of central arteries (CtA) in the hindbrain also occurs in a metamerically fashion and genetic studies have shown that many of the principles underlying the formation of the ISVs (Vegfr signaling and N/Dll interplay) are conserved in the control of CtA formation (Fujita et al., 2011; Bussmann, Wolfe, & Siekmann, 2011). However, in addition to these signaling pathways, brain-specific regulators for CtA formation have been identified. Both the *gpr124* and the *reck* gene are required for CNS angiogenesis, but not for the formation of the trunk vasculature (Ulrich et al., 2016; Vanhollebeke et al., 2015). Gpr124 and Reck directly interact with each other and are required for Wnt signaling in CtAs, a prerequisite for their formation. The correct guidance of CtA sprouts also requires chemokine signaling; it has been shown that *cxcr4* and *cxcl12b* mutants display disruptions in the organization of CtA patterning due to misguidance and a failure to connect via anastomosis. The chemokine receptor Cxcr4 is expressed in ECs, while the ligand is expressed in the hindbrain neural keel, immediately adjacent to the assembling basilar artery (Bussmann et al., 2011; Fujita et al., 2011).

Guided migration of endothelial tip cells is of utmost importance for the overall architecture of vascular branching patterns. Once angiogenic sprout formation has been initiated, the migratory path of the tip cell eventually dictates the spatial location of the newly forming vessel within the organism,

and most likely also the place where anastomosis will ultimately be initiated (see below). Many different factors have been identified which contribute to vessel guidance. While Vegf signaling is clearly one of the key factors of vasculature patterning and has been linked to vessel guidance (see ISVs and sFlt1 above), many other molecules have been associated with tip cell guidance by providing both attracting and repelling cues. For example, recent studies have shown that chemokines such as Cxcl and the corresponding receptors (Cxcr) are important attractive determinants for sprout guidance (see for example, [Red-Horse & Siekmann, 2019](#)). Interestingly, many proteins involved in neural pathfinding have been shown to contribute to directed tip cell migration ([Eichmann & Thomas, 2013](#); see also Semaphorins mentioned above). Clearly, the generation of complex vascular networks in a developing vertebrate embryo involves a plethora of instructive and permissive guidance cues. In most cases, and due to the incredible complexity of the vasculature, the precise molecular nature of factors associated with the guidance of particular vessels is not known to date. Furthermore, topological constraints are certainly of key importance as well and the ECM and its local composition plays a central role ([Chaqour & Karrasch, 2020](#)). In addition, arteries and veins often align in mature vascular beds (see for example, [Kidoya et al., 2015](#)), and so do vessels and nerves (see for example, [Kwon et al., 2013](#)), contributing important aspects to generation of the final architecture of vascular networks.



### **3. Where to connect: Formation of an interconnected network via anastomosis**

For newly-formed sprouts to be able to support blood flow, they have to connect to other sprouts or to existing vessels and form a continuous luminal space. This process is called anastomosis and has been described in much detail in the early zebrafish embryo. Interestingly, it was found that during sprout connection, lumenization is brought about by two different mechanisms, transcellular lumen formation and cord hollowing ([Herwig et al., 2011](#); [Lenard et al., 2013](#)). During the initial steps of anastomosis, new Adherens junction (AJ) proteins are deposited at the initial site of filopodial contacts between migrating ECs. The formation of these initial contacts is facilitated by filopodial activity ([Phng, Stanchi, & Gerhardt, 2013](#)) and results in a stabilization of novel EC-EC contacts via Ve-cad and Esama, which appear to play both redundant and non-redundant functions during anastomosis ([Sauteur, Affolter, & Belting, 2017](#)). Such stabilized, spot-like contact

points expand into ring-like structures, generating an apical membrane pocket between the two sprouts. During this process, bipolar EC are formed, with two independent apical domains at either end of the cell (Caviglia & Luschnig, 2014; Kotini, Mae, Belting, Betsholtz, & Affolter, 2019). During the cord hollowing process, which occurs when two non-lumenized sprouts connect, these two apical membrane compartments are brought together via cell rearrangements accompanied by extensive junctional remodeling, which ultimately leads to lumen coalescence and the formation of a multicellular vascular tube. Vessel anastomosis via transcellular lumen formation occurs in lumenized sprouts, with blood pressure being the major driving force, which leads to apical membrane extension and invagination into the tip/fusion cell, thereby generating a transcellular lumen. The membrane of this transcellular lumen eventually fuses with the de novo generated, distal apical membrane compartment at the contact site, thereby generating a transient unicellular tube in the anastomosing cell. This transcellular tube segment is rapidly transformed into a multicellular tube via cell rearrangements and cell splitting (see Betz, Lenard, Belting, & Affolter, 2016). As a result, both mechanisms of vascular anastomosis, cord hollowing and transcellular lumen formation, lead to the formation of multicellular tubes, and no apparent signs remain as a testimony that a particular vascular segment has been formed via an anastomosis process (reviewed in Kotini et al., 2019).

Anastomosis is a key process during the formation of the vasculature. Each newly formed sprout eventually has to anastomose either with another sprout (which is also called head-to-head anastomosis), or with an existing vessel (also called head-to-side anastomosis), in order to be incorporated into the functional network. While the highly dynamic EC behaviors underlying the anastomosis process are being further investigated at the cellular and molecular level, a key question with regard to the formation of the three-dimensional architecture of a given vasculature network is *where* emerging sprouts connect to either other sprouts or to functional branches, thereby giving rise to new vascular loops and shaping the architecture of the resulting network. While in some cases, generic anastomoses prevent dead ends in the vasculature, in other cases specific anastomosis events might ensure proper blood flow patterns.

In many cases, anastomosis might simply be initiated by the serendipitous contact of two endothelial tip cells migrating towards each other in the same tissue area. Such a scenario might be at work during the formation of the dorsal longitudinal vessel (DLAV) in the early zebrafish embryo, where

tip cell extensions are formed along the dorsal side of the neural tube in anterior and posterior directions, ultimately leading to filopodial contacts between tip cells of neighboring segments and the initiation of the anastomosis process (Blum et al., 2008; Herwig et al., 2011; Lawson & Weinstein, 2002). In the head vasculature, anastomosis events between a sprout tip cell and an existing, blood-carrying vessel have also been described in detail (Hubner et al., 2018; Kochhan et al., 2013; Lenard et al., 2013). The cellular activities underlying such anastomosis processes, which involve a single tip cell, are very similar to the anastomosis of two sprouting tips and require the formation of novel EC contacts and apical membrane deposition. Lumenization is then achieved via transcellular lumen formation by apical membrane invagination into the former tip cell, driven by the extant blood pressure from the functional vessel.

Interestingly, at least in one of the studied cases, efficient formation of anastomotic contacts has been shown to be regulated during the formation of the central arteries (CtA) (Hubner et al., 2018). Wnt signaling appears to suppress Shingosine-1 phosphatase receptor (S1pr) signaling during sprouting to enable the dynamic junction formation during anastomosis; in the absence of Wnt signaling, premature S1pr signaling reduces VE-cadherin and Esama levels at cell-cell junctions, thereby leading to inefficient anastomosis. In another case, the loss of Cxcr4 or Cxcl12 leads to a failure of vein sprouts to connect to arteries due to a failure in anastomosis (Kochhan et al., 2013). During zebrafish fin regeneration, the loss of Cxcl12 also leads to a failure in anastomosis of venous sprouts with arteries, and veins fuse back to veins (Xu et al., 2014). In both cases, it remains to be investigated in more detail whether Cxcr4/Cxcl12 signaling is required for directional migration toward the arteries only (eventually leading to EC contact and anastomosis), or whether it is more directly linked to anastomosis competence.

An interesting case to study the control of anastomosis processes are the secondary sprouts in the zebrafish embryo (Isogai, 2003). These sprouts initiate from the PCV and eventually connect to primary branches formed earlier from the DA. The secondary sprouts first migrate over the DA, but do not undergo anastomosis with this particular vessel. It is not clear why no stable EC-EC contacts are established between secondary sprouts and the DA, but it is possible that the basal lamina surrounding the DA at that stage prohibits filopodia contacts of secondary sprouts and ECs embedded in the DA. Once the sprouts reach the level of ECs embedded in primary sprouts, anastomosis is initiated by the formation and stabilization of

filopodial contacts. While one study suggests that only every other secondary sprout undergoes anastomosis with a primary branch and that branches keeping an arterial fate do not anastomose with sprouting veins (Weijts et al., 2018), another study argues that most secondary sprouts initiate and complete anastomosis, and that half of these connections subsequently prune (Geudens et al., 2019). In this second scenario, anastomosis itself does not need to be controlled, while in the first scenario, secondary sprouts either anastomose or fail to anastomose, and this would have to be controlled at the molecular level. Additional analyses will be needed to further address this important issue.

In the future, it will be important to try to clarify whether there is a “code” for anastomosis or whether the anastomosis process is simply a consequence of physical encounters of ECs and the formation and stabilization of novel *Ve-cad* and *Esam*-dependent cell-cell adhesion contacts. In the latter case, the environment in which a sprout navigates determines its potential connecting sprout or vessel. It is possible that veins selectively initiate anastomosis upon contacting arteries. Vessels might also be protected from anastomosis by maturation, which includes the recruitment of mural cells and the formation of a basal membrane. In certain cases, tissue macrophages might act as cellular chaperons for vascular anastomosis (Fantin et al., 2010).

Interestingly, Bautch and colleagues have shown that *mFlt1* levels affect the anastomosis process through the frequency and effectiveness of transient filopodial contacts between sprouts (Nesmith, Chappell, Cluceru, & Bautch, 2017). They propose that the location and timing of establishing a stable connection via spatially regulated, EC-intrinsic modulation of *mFlt1* is involved in the regulation of vascular network formation in vascular beds that do not have an imposed pre-pattern.

Much more needs to be learned about the anastomosis of sprouts within different vascular beds before general considerations about the importance of selective anastomosis in generating a given architecture of a vascular network can be made. We also do not know whether it is more common that two tip cells undergo anastomosis (head-to-head), or that sprouts connect to existing vessels (head-to-side). Since there are countless anastomosis events in a developing organism (many inducing subsequent pruning events, see below), the process needs to be better understood in order to get a clearer picture of the mechanisms underlying the architectural design of vascular networks.



#### 4. Where to remodel: Optimizing flow in vascular networks via pruning

Vascular networks formed by sprouting angiogenesis undergo extensive remodeling to form a mature and functional vasculature (reviewed in Korn & Augustin, 2015). In some cases, entire vascular beds are removed or regress (either during development, during pregnancy or in pathological conditions), a process that is most often accompanied by shedding of cells into the circulation or by EC apoptosis. In other cases, pruning of a previously formed, short vessel segment is required to optimize flow through the network, which is often associated with EC rearrangements.

Recently, vessel remodeling through pruning has been studied both in mouse and in zebrafish at the cellular and, to some extent, at the molecular level (see Campinho et al., 2020; Okuda & Hogan, 2020; Szymborska & Gerhardt, 2018). While in some vessels, apoptosis does occur during pruning (Kochhan et al., 2013), it has been observed in several cases that EC rearrangements are the drivers of the remodeling process; ECs in pruning vessels migrate into the adjacent, maintained vessel branches (Chen et al., 2012; Franco et al., 2015; Kochhan et al., 2013; Lenard et al., 2015). In the mouse retina, the pruning process was subdivided into four steps; branch selection, lumen stenosis, EC retraction and resolution (Franco et al., 2015). Using live imaging in zebrafish embryos at high resolution, vessel pruning has been described as “reverse anastomosis,” since the cellular events in pruning appear to occur in reverse order to those seen in anastomosis (Kochhan et al., 2013; Lenard et al., 2015); multicellular vessels give rise to unicellular vessels through cell rearrangements, ultimately leading to the complete loss of contact between ECs migrating into the two neighboring vessels, thereby resolving the connection (see Betz et al., 2016 for a more detailed description).

What leads to the pruning of distinct vessel segments during the development of functional vascular networks? Experimental manipulation of hemodynamics in the developing zebrafish embryo demonstrated that pruning in the brain vasculature occurs by lateral migration of ECs from vessels exposed to low and variable blood flow towards the neighboring vessel with stronger flow (Chen et al., 2012). Similarly, vessel pruning was also associated with blood flow changes in the zebrafish eye (Kochhan et al., 2013). Using high resolution cellular analysis combined with computational modeling of flow-induced shear forces, it was proposed that flow-induced, polarized migration of ECs breaks symmetry and leads to stabilization of

high flow/shear segments and regression of adjacent low flow/shear segments (Franco et al., 2015). Since ECs in arteries generally orient and migrate quite consistently against flow (see Red-Horse & Siekmann, 2019), it is possible that ECs migrating in high flow vessels pull neighboring EC they are connected to out of low flow vessels. Such a scenario is consistent with the numerous reports showing that pruning requires blood flow and does not occur when general flow through the vasculature is inhibited.

These studies start to provide important insights into the cellular processes underlying vascular remodeling, which ultimately leads to the formation of functional vascular branching patterns. In several cases, pruning might be the result of stereotyped anastomosis events, resulting in distinct changes in the blood flow patterns and the resulting hemodynamic forces in the local network, eventually causing the pruning of a defined vessel segment. This is the case for a characteristic blood vessel in the eye of the zebrafish embryo (Kochhan et al., 2013). In other cases studied so far, pruning is not stereotyped, meaning that different branches are pruned in different individuals (Chen et al., 2012; Franco et al., 2015; Lenard et al., 2015). Such “non-stereotyped” pruning events might predominantly occur in those places in which the development of a mature vascular network includes the formation of a vascular plexus. Since studies on the process of pruning are only at the beginning (Korn & Augustin, 2015), there is still much to be learned about vascular remodeling and its contribution to the generation of the final architecture of the mature vasculature.



## 5. Concluding remarks and outlook

Over the last decades, much has been learned about sprouting, anastomosis and pruning, key routines involved in the formation and shaping of vascular circuits. Molecular players involved in these complex cellular processes have been identified, and it has become clearer how the three processes can be controlled in a precise manner, thereby resulting in discrete and predictable events of sprouting, anastomosis and pruning, ultimately resulting in conserved architectural features of the anatomy of the vasculature. It is interesting to note that despite the large number of cells building up the vasculature, key features underlying angiogenesis, such as sprouting and anastomosis, are processes involving single ECs and their immediate neighbors. Sprouting and anastomosis involving large vessels are not commonly seen in vascular development, although they do occasionally occur (fusion of the two separate dorsal vessels in early chick development, for example).

Blood circulation through the forming network plays a key role in all aspects of vascular development, from angiogenic sprouting to lumen formation, vascular pruning, and the regulation of vessel caliber (Campinho et al., 2020). In addition to its involvement in the genetically hard-wired development of specific vessels mentioned above, blood flow and blood pressure provide constant and essential input into the formation of an efficient vascular network. In particular, fluid shear stress sensing by the endothelial layer underlies many developmental and physiological vascular processes and the hierarchical organizations of vessel diameter in the vascular tree (Baeyens & Schwartz, 2016; Roux, Bougaran, Dufourcq, & Couffignal, 2020). Recent data suggest that blood flow also plays a key role in the migration of venous-derived cells towards arteries during plexus remodeling (see Red-Horse & Siekmann, 2019), uncovering a conserved mode of artery formation.

It also turns out, somewhat surprisingly, that several organ-specific vascular beds do not arise by angiogenesis only (sprouting from existing vessels), but rather by a combination of vasculogenesis and angiogenesis. This is the case for certain aspects of the brain vasculature (Proulx, Lu, & Sumanas, 2010) as well as for the formation of the SIV plexus, which eventually gives rise to the intestinal vasculature (Goi & Childs, 2016; Hen et al., 2015; Koenig et al., 2016). In this latter case, angioblasts detach from existing vessels, and form an initial vessel from which sprouts subsequently arise. How these vascular beds connect to existing vessels remains to be investigated in detail.

Furthermore, it is well established that the vasculature is essential for the development of other organs but that its role is not restricted to oxygen or nutrient supply. Indeed, paracrine signals from endothelial cells, also known as angiocrine factors, are important for organ morphogenesis and cell differentiation (Raffi, Butler, & Ding, 2016; Tata & Ruhrberg, 2018). The developing vasculature is thus not simply following the formation of other organs but interacts and shapes these systems to some extent.

There is still much to be learned about how complex vascular network architectures arise and one can look with excitement to the future and await further pieces of the puzzle to be placed and thereby contribute to the bigger picture.

## References

- Baeyens, N., & Schwartz, M. A. (2016). Biomechanics of vascular mechanosensation and remodeling. *Molecular Biology of the Cell*, 27, 7–11. E14-11-1522.
- Betz, C., Lenard, A., Belting, H. G., & Affolter, M. (2016). Cell behaviors and dynamics during angiogenesis. *Development*, 143, 2249–2260.



- Blum, Y., Belting, H. G., Ellertsdottir, E., Herwig, L., Luders, F., & Affolter, M. (2008). Complex cell rearrangements during intersegmental vessel sprouting and vessel fusion in the zebrafish embryo. *Developmental Biology*, 316, 312–322.
- Bussmann, J., Wolfé, S. A., & Siekmann, A. F. (2011). Arterial-venous network formation during brain vascularization involves hemodynamic regulation of chemokine signaling. *Development*, 138, 1717–1726.
- Campinho, P., Vilfan, A., & Vermot, J. (2020). Blood flow forces in shaping the vascular system: A focus on endothelial cell behavior. *Frontiers in Physiology*, 11, 552.
- Caviglia, S., & Luschnig, S. (2014). Tube fusion: Making connections in branched tubular networks. *Seminars in Cell & Developmental Biology*, 31, 82–90.
- Chaqour, B., & Karrasch, C. (2020). Eyeing the extracellular matrix in vascular development and microvascular diseases and bridging the divide between vascular mechanics and function. *International Journal of Molecular Sciences*, 21, 1–22.
- Chen, Q., Jiang, L., Li, C., Hu, D., Bu, J.-W., Cai, D., et al. (2012). Haemodynamics-driven developmental pruning of brain vasculature in zebrafish. *PLoS Biology*, 10, e1001374.
- Eichmann, A., & Thomas, J. L. (2013). Molecular parallels between neural and vascular development. *Cold Spring Harbor Perspectives in Medicine*, 3, a006551.
- Eilken, H. M., & Adams, R. H. (2010). Dynamics of endothelial cell behavior in sprouting angiogenesis. *Current Opinion in Cell Biology*, 22, 1–9. Elsevier Ltd.
- Fantin, A., Vieira, J. M., Gestri, G., Denti, L., Schwarz, Q., Prykhodzhiy, S., et al. (2010). Tissue macrophages act as cellular chaperones for vascular anastomosis downstream of VEGF-mediated endothelial tip cell induction. *Blood*, 116, 829–840.
- Fonseca, C. G., Barbacena, P., & Franco, C. A. (2020). Endothelial cells on the move: Dynamics in vascular morphogenesis and disease. *Vascular Biology (Bristol, England)*, 2, H29–H43.
- Franco, C. A., Jones, M. L., Bernabeu, M. O., Geudens, I., Mathivet, T., Rosa, A., et al. (2015). Dynamic endothelial cell rearrangements drive developmental vessel regression. *PLoS Biology*, 13, e1002125.
- Fujita, M., Cha, Y. R., Pham, V. N., Sakurai, A., Roman, B. L., Gutkind, J. S., et al. (2011). Assembly and patterning of the vascular network of the vertebrate hindbrain. *Development*, 138, 1705–1715.
- Geudens, I., Coxam, B., Alt, S., Gebala, V., Vion, A. C., Meier, K., et al. (2019). Artery-vein specification in the zebrafish trunk is pre-patterned by heterogeneous Notch activity and balanced by flow-mediated fine-tuning. *Development*, 146, 1–13.
- Goi, M., & Childs, S. J. (2016). Patterning mechanisms of the sub-intestinal venous plexus in zebrafish. *Developmental Biology*, 409, 114–128.
- Goodwin, K., & Nelson, C. M. (2020). Branching morphogenesis. *Development*, 147, 1–6.
- Hen, G., Nicenboim, J., Mayseless, O., Asaf, L., Shin, M., Busolin, G., et al. (2015). Venous-derived angioblasts generate organ-specific vessels during zebrafish embryonic development. *Development*, 142, 4266–4278.
- Herbert, S. P., & Stainier, D. Y. R. (2011). Molecular control of endothelial cell behaviour during blood vessel morphogenesis. *Nature Reviews. Molecular Cell Biology*, 12, 551–564.
- Herwig, L., Blum, Y., Krudewig, A., Ellertsdottir, E., Lenard, A., Belting, H. G., et al. (2011). Distinct cellular mechanisms of blood vessel fusion in the zebrafish embryo. *Current Biology*, 21, 1942–1948.
- Hogan, B. M., & Schulte-Merker, S. (2017). How to plumb a Pisces: Understanding vascular development and disease using zebrafish embryos. *Developmental Cell*, 42, 567–583.
- Horowitz, A., & Simons, M. (2008). Branching morphogenesis. *Circulation Research*, 104, 784. Am Heart Assoc.
- Hubner, K., Cabochette, P., Dieguez-Hurtado, R., Wiesner, C., Wakayama, Y., Grassme, K. S., et al. (2018). Wnt/beta-catenin signaling regulates VE-cadherin-mediated anastomosis of brain capillaries by counteracting S1pr1 signaling. *Nature Communications*, 9, 4860.

- Isogai, S. (2003). Angiogenic network formation in the developing vertebrate trunk. *Development*, *130*, 5281–5290.
- Isogai, S., Horiguchi, M., & Weinstein, B. M. (2001). The vascular anatomy of the developing zebrafish: An atlas of embryonic and early larval development. *Developmental Biology*, *230*, 278–301.
- Jakobsson, L., Bentley, K., & Gerhardt, H. (2009). VEGFRs and notch: A dynamic collaboration in vascular patterning. *Biochemical Society Transactions*, *37*, 1233–1236.
- Kidoya, H., Naito, H., Muramatsu, F., Yamakawa, D., Jia, W., Ikawa, M., et al. (2015). APJ regulates parallel alignment of arteries and veins in the skin. *Developmental Cell*, *33*, 247–259.
- Kochhan, E., Lenard, A., Ellertsdóttir, E., Herwig, L., Affolter, M., Belting, H.-G., et al. (2013). Blood flow changes coincide with cellular rearrangements during blood vessel pruning in zebrafish embryos. *PLoS One*, *8*, e75060.
- Koenig, A. L., Baltrunaite, K., Bower, N. I., Rossi, A., Stainier, D. Y., Hogan, B. M., et al. (2016). Vegf signaling promotes zebrafish intestinal vasculature development through endothelial cell migration from the posterior cardinal vein. *Developmental Biology*, *411*, 115–127.
- Korn, C., & Augustin, H. G. (2015). Mechanisms of vessel pruning and regression. *Developmental Cell*, *34*, 5–17.
- Kotini, M. P., Mae, M. A., Belting, H. G., Betsholtz, C., & Affolter, M. (2019). Sprouting and anastomosis in the Drosophila trachea and the vertebrate vasculature: Similarities and differences in cell behaviour. *Vascular Pharmacology*, *112*, 8–16.
- Kwon, H. B., Fukuhara, S., Asakawa, K., Ando, K., Kashiwada, T., Kawakami, K., et al. (2013). The parallel growth of motoneuron axons with the dorsal aorta depends on Vegf/Vegfr3 signaling in zebrafish. *Development*, *140*, 4081–4090.
- Lawson, N. D., Mugford, J. W., Diamond, B. A., & Weinstein, B. M. (2003). Phospholipase C gamma-1 is required downstream of vascular endothelial growth factor during arterial development. *Genes & Development*, *17*, 1346–1351.
- Lawson, N. D., & Weinstein, B. M. (2002). In vivo imaging of embryonic vascular development using transgenic zebrafish. *Developmental Biology*, *248*, 307–318.
- Lenard, A., Ellertsdóttir, E., Herwig, L., Krudewig, A., Sauter, L., Belting, H. G., et al. (2013). In vivo analysis reveals a highly stereotypic morphogenetic pathway of vascular anastomosis. *Developmental Cell*, *25*, 492–506.
- Lenard, A., Daetwyler, S., Betz, C., Ellertsdóttir, E., Belting, H. G., Huisken, J., et al. (2015). Endothelial cell self-fusion during vascular pruning. *PLoS Biology*, *13*, e1002126.
- Matsuoka, R. L., Marass, M., Avdesh, A., Helker, C. S., Maischein, H. M., Grosse, A. S., et al. (2016). Radial glia regulate vascular patterning around the developing spinal cord. *eLife*, *5*, 1–24.
- Nesmith, J. E., Chappell, J. C., Cluceru, J. G., & Bautch, V. L. (2017). Blood vessel anastomosis is spatially regulated by Flt1 during angiogenesis. *Development*, *144*, 889–896.
- Okuda, K. S., & Hogan, B. M. (2020). Endothelial cell dynamics in vascular development: Insights from live-imaging in zebrafish. *Frontiers in Physiology*, *11*, 842.
- Phng, L. K., Stanchi, F., & Gerhardt, H. (2013). Filopodia are dispensable for endothelial tip cell guidance. *Development*, *140*, 4031–4040.
- Potente, M., Gerhardt, H., & Carmeliet, P. (2011). Basic and therapeutic aspects of angiogenesis. *Cell*, *146*, 873–887.
- Proulx, K., Lu, A., & Sumanas, S. (2010). Cranial vasculature in zebrafish forms by angioblast cluster-derived angiogenesis. *Developmental Biology*, *348*, 34–46.
- Rafii, S., Butler, J. M., & Ding, B. S. (2016). Angiocrine functions of organ-specific endothelial cells. *Nature*, *529*, 316–325.
- Red-Horse, K., & Siekmann, A. F. (2019). Veins and arteries build hierarchical branching patterns differently: Bottom-up versus top-down. *BioEssays*, *41*, e1800198.

- Roux, E., Bougaran, P., Dufourcq, P., & Couffinhal, T. (2020). Fluid shear stress sensing by the endothelial layer. *Frontiers in Physiology*, *11*, 861.
- Sauteur, L., Affolter, M., & Belting, H. G. (2017). Distinct and redundant functions of Esam and VE-cadherin during vascular morphogenesis. *Development*, *144*, 1554–1565.
- Shin, M., Beane, T. J., Quillien, A., Male, I., Zhu, L. J., & Lawson, N. D. (2016). Vegfa signals through ERK to promote angiogenesis, but not artery differentiation. *Development*, *143*, 3796–3805.
- Siekman, A. F., Affolter, M., & Belting, H.-G. (2013). The tip cell concept ten years after: New players tune in for a common theme. *Experimental Cell Research*, *319*, 1255–1263.
- Szymborska, A., & Gerhardt, H. (2018). Hold me, but not too tight-endothelial cell-cell junctions in angiogenesis. *Cold Spring Harbor Perspectives in Biology*, *10*, 1–16.
- Tata, M., & Ruhrberg, C. (2018). Cross-talk between blood vessels and neural progenitors in the developing brain. *Neural Signaling*, *2*, NS20170139.
- Torres-Vázquez, J., Gitler, A. D., Fraser, S. D., Berk, J. D., Pham, V. N., Fishman, M. C., et al. (2004). Semaphorin-Plexin signaling guides patterning of the developing vasculature. *Developmental Cell*, *117*, 123.
- Ulrich, F., Carretero-Ortega, J., Menendez, J., Narvaez, C., Sun, B., Lancaster, E., et al. (2016). Reck enables cerebrovascular development by promoting canonical Wnt signaling. *Development*, *143*, 147–159.
- Vanhollebeke, B., Stone, O. A., Bostaille, N., Cho, C., Zhou, Y., Maquet, E., et al. (2015). Tip cell-specific requirement for an atypical Gpr124- and Reck-dependent Wnt/beta-catenin pathway during brain angiogenesis. *eLife*, *4*, 1–25.
- Vila Ellis, L., Cain, M. P., Hutchison, V., Flodby, P., Crandall, E. D., Borok, Z., et al. (2020). Epithelial Vegfa specifies a distinct endothelial population in the mouse lung. *Developmental Cell*, *52*, 617–630 e6.
- Weijts, B., Gutierrez, E., Saikin, S. K., Ablooglu, A. J., Traver, D., Groisman, A., et al. (2018). Blood flow-induced notch activation and endothelial migration enable vascular remodeling in zebrafish embryos. *Nature Communications*, *9*, 5314.
- Wild, R., Klems, A., Takamiya, M., Hayashi, Y., Strahle, U., Ando, K., et al. (2017). Neuronal sFlt1 and Vegfaa determine venous sprouting and spinal cord vascularization. *Nature Communications*, *8*, 13991.
- Xu, C., Hasan, S. S., Schmidt, I., Rocha, S. F., Pitulescu, M. E., Bussmann, J., et al. (2014). Arteries are formed by vein-derived endothelial tip cells. *Nature Communications*, *5*, 5758.
- Yokota, Y., Nakajima, H., Wakayama, Y., Muto, A., Kawakami, K., Fukuhara, S., et al. (2015). Endothelial Ca<sup>2+</sup> oscillations reflect VEGFR signaling-regulated angiogenic capacity in vivo. *eLife*, *4*, 1–26.
- Zygmunt, T., Gay, C. M., Blondelle, J., Singh, M. K., Flaherty, K. M., Means, P. C., et al. (2011). Semaphorin-PlexinD1 signaling limits angiogenic potential via the VEGF decoy receptor sFlt1. *Developmental Cell*, *21*, 301–314.

## 9 Acknowledgements

First and foremost, I would like to thank Prof. Dr. Markus Affolter, for giving me the opportunity to achieve my goal of earning a PhD-title. I want to especially thank him for his always optimistic and encouraging nature, which always helped me to remotivate myself, and try to do the next step. This laboratory was always a place to feel welcomed and a place where you would want to come back to every day.

Then I would like to thank my PhD advisory committee members, Prof. Dr. Alexander Schier and Prof. Dr. Anna Jazwinska for their constructive criticism during the committee meetings, that helped to keep my project focused.

Further I would like to express my gratitude to the people who keep the lab running day in, day out. Dr. Martin Müller, Helen Mawer and Dr. Heinz-Georg Belting. Special thanks to Dr. Heinz-Georg Belting for his critical questions that during this time always pushed me to rethink my assumptions and to keep me on my toes.

I want to thank Kumuthini Kulendra, Fabio Tschudin and Marina Signer and the rest of the fish group for taking such good care of our most important employees. our zebrafish lines.

Additionally I would like the imaging and proteomics Core Facilities of the Biozentrum for their expertise and their generous help with all the questions I could possibly think of. I want to especially mention Kai Schleicher from the imaging facility and Alexander Schmidt from the proteomics core facility. Kai was always there when I had some questions regarding the microscopes I was using, when something wasn't working or what the best way to process the images was. Alex Schmidt was strongly involved in designing the reference peptides and the proteomics measurements and further helped me with analysing the data and provided me with some more complicated calculations.

Then I want to thank all the lab members. You made me understand why Markus sometimes refers to the people in the lab as a second family. I want to thank especially Dr. Etienne Schmelzer who was a big help in getting the project started, not only with his initial experiments which laid the groundwork, but also for his discussions in the early stages of the project, and his kind words towards the end of it. I want to thank Dr. Alessandra Vigano who helped me continuously during the time of my PhD-research. From advice of how to clone, to shared generation of fish lines or setting up of RT-qPCR reactions, she had always an open ear and great advice.

Then I want to thank Milena Bauer, Gustavo Aguillar, Maria Kotini and Sheida Hadji Rasouliha for their emotional support, the scientific discussions, the distractions and especially their friendship which made this experience a lot more fun.

Finally I want to thank my family. My parents, Jacqueline und Roger, who always and unconditionally, believed in me and supported me no matter which choices I made, my sisters, Jeaninne and Ladina

who were always there for me regardless of when and where and Alexandra Tanner without whom nothing of this would have happened because I wouldn't have had the strength. Special thanks also to my friends Michel Mongiat, Luca Grünig, Marcel Zehnder, Patrick Huber, Michael Tschannen, Andreas Bösch and Aurel Holzschuh for keeping me grounded, distracted and sane.

## 10 Appendix

### 10.1 *rab7* knockdown leads to vascular phenotypes

To test whether *rab7* has a similar function in lumen development in the zebrafish vasculature as it has in tracheal fusion in flies, three splice morpholinos have been designed to inhibit splicing at the donor site of exon2 in each of the three *rab7* genes; since exon2 contains the start codon, this should result in a knock-down of the corresponding *rab7* paralog. Morpholinos were injected into *Tg(kdrl:EGFP-CAAX); BAC(lamp2:LAMP2-RFP)* embryos, visualizing the apical membrane in green and late endosomes and lysosomes in red. Knock-down has been confirmed by RT-PCR using primers within Exon1 and Exon 3 as well as loss of signal in a PCR with Primers in Exon 2 and Exon 3 (Figure 23A).

While knockdown of *rab7a* and *rab7bb* did not impair initial lumen formation, *rab7ba* knockdown resulted in fragmentation of the lumen. Additionally, *rab7a* knockdown resulted in ectopic sprouting and a patterning of ISVs that did not respect the somite boundaries (Figure 23B). *rab7ba* and *rab7bb* knock-down lead to a partial loss of interconnections in the DLAV after 48hpf. At 72hpf fragmented lumen in *rab7b*-MO injected fish has recovered and blood flow could be observed in all embryos. For *rab7a*-MO injected fish however blood vessel architecture could not be corrected and 40% of embryos still showed ectopic vascular architecture. In *rab7bb*-MO injected fish, although initial lumen formation was normal. Blood flow could not be established in 66% of embryos when injected with a dose of 1pM of MO. At lower dose (< 0.4pM) however this defect couldn't be observed anymore. In general injection doses were chosen that did not result in an increased lethality compared to standard-MO injected embryos. The dose of 0.4pM proofed to be the most reliable in not generating an excessive amount of dead or strongly malformed embryos.

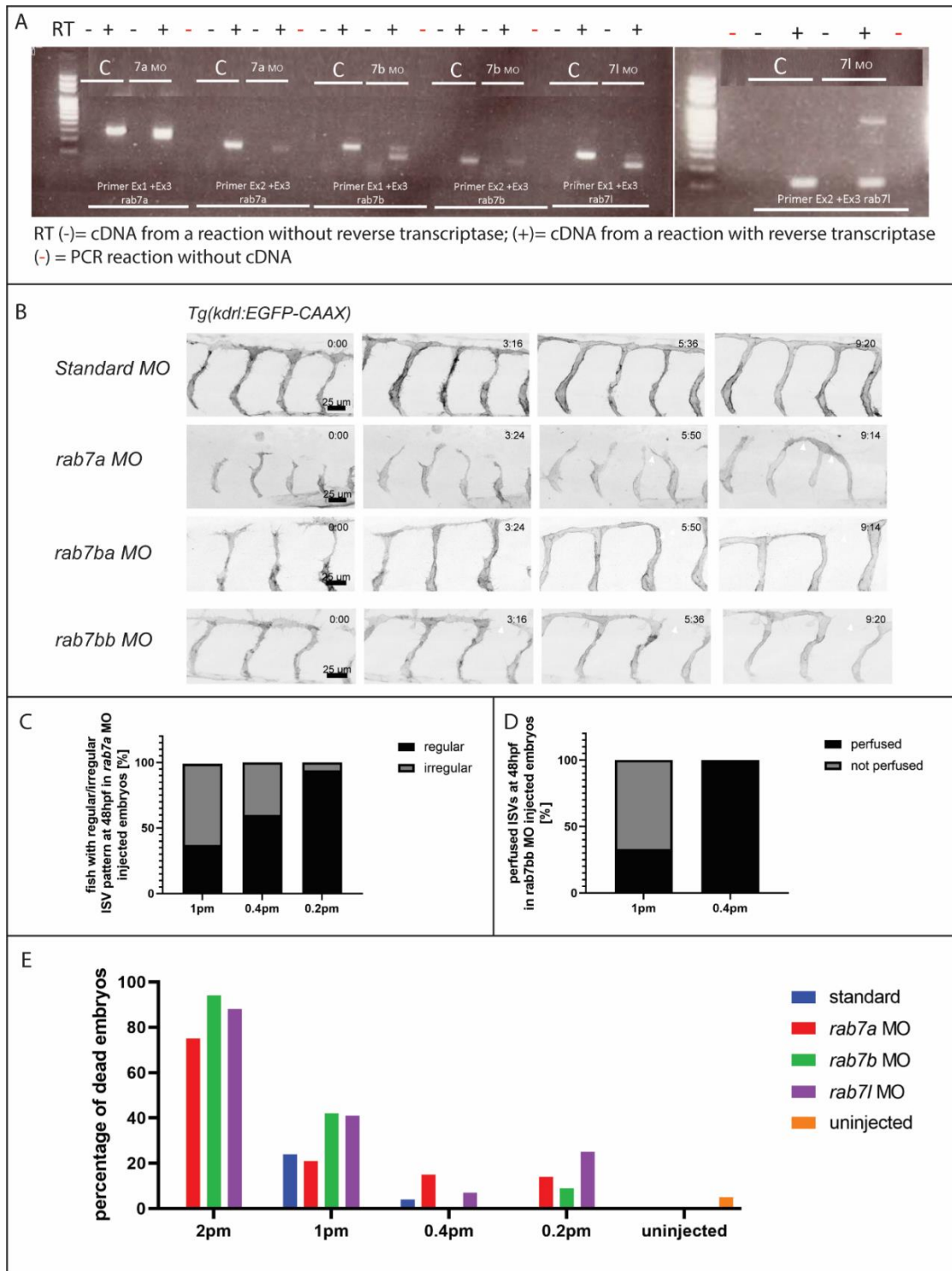


**Figure 23 Validation and description of *rab7* isoform specific morpholinos**

**A** Agarose gel of RT-PCR with primers in exon 1 and exon 3 or exon 2 and exon 3 to check for loss of exon 2 on the mRNA level after injection against the respective *rab7* gene. Double bands in reactions with primers in exon1 and exon3 show two populations of mRNA lengths. Lower band lacks exon2 upper band is full length mRNA. **B** Confocal still pictures from time-lapse movies (starting around 32 hpf) showing lateral views (anterior to the left) of SeA morphogenesis in transgenic *Tg(kdrl:EGFP-CAAX)*; *BAC(lamp2:LAMP2-RFP)* embryos injected with morpholinos against *rab7a*, *rab7ba* or *rab7bb*. **C** Number of embryos injected with different concentrations of *rab7a*-MO that showed irregular architecture of the ISVs and ectopic sprouting (N= 16 embryos). **D** Number of embryos injected with different concentrations of *rab7bb*-MO that showed no blood flow in the ISVs after 48hpf (1pM of MO N= 56 embryos; 0.4pM N=74).

## 11 References

Ali, B. R. (2004). "Multiple regions contribute to membrane targeting of Rab GTPases." Journal of Cell Science **117**(26): 6401-6412.

Ando, K., S. Fukuhara, N. Izumi, H. Nakajima, H. Fukui, R. N. Kelsh and N. Mochizuki (2016). "Clarification of mural cell coverage of vascular endothelial cells by live imaging of zebrafish." Development **143**(8): 1328-1339.

Andrews, N. W., P. E. Almeida and M. Corrotte (2014). "Damage control: cellular mechanisms of plasma membrane repair." Trends in Cell Biology **24**(12): 734-742.

Andrews, N. W., M. Corrotte and T. Castro-Gomes (2015). "Above the fray: Surface remodeling by secreted lysosomal enzymes leads to endocytosis-mediated plasma membrane repair." Seminars in Cell & Developmental Biology **45**: 10-17.

Antonescu, C. N., F. Aguet, G. Danuser and S. L. Schmid (2011). "Phosphatidylinositol-(4,5)-bisphosphate regulates clathrin-coated pit initiation, stabilization, and size." Molecular Biology of the Cell **22**(14): 2588-2600.

Antonny, B., C. Burd, P. De Camilli, E. Chen, O. Daumke, K. Faelber, M. Ford, V. A. Frolov, A. Frost, J. E. Hinshaw, T. Kirchhausen, M. M. Kozlov, M. Lenz, H. H. Low, H. McMahon, C. Merrifield, T. D. Pollard, P. J. Robinson, A. Roux and S. Schmid (2016). "Membrane fission by dynamin: what we know and what we need to know." The EMBO Journal **35**(21): 2270-2284.

Araujo, M. E. G., G. Liebscher, M. W. Hess and L. A. Huber (2020). "Lysosomal size matters." Traffic **21**(1): 60-75.

Barouch, W., K. Prasad, L. E. Greene and E. Eisenberg (1994). "ATPase activity associated with the uncoating of clathrin baskets by Hsp70." Journal of Biological Chemistry **269**(46): 28563-28568.

Bayless, K. J. and G. E. Davis (2002). "The Cdc42 and Rac1 GTPases are required for capillary lumen formation in three-dimensional extracellular matrices." J Cell Sci **115**(Pt 6): 1123-1136.

Best, B. T. and M. Leptin (2020). "Multiple Requirements for Rab GTPases in the Development of Drosophila Tracheal Dorsal Branches and Terminal Cells." G3 Genes|Genomes|Genetics **10**(3): 1099-1112.

Betz, C., A. Lenard, H.-G. Belting and M. Affolter (2016). "Cell behaviors and dynamics during angiogenesis." Development **143**(13): 2249-2260.

Blanco, R. and H. Gerhardt (2013). "VEGF and Notch in Tip and Stalk Cell Selection." Cold Spring Harbor Perspectives in Medicine **3**(1): a006569-a006569.

Borg Distefano, M., L. H. Haugen, Y. Wang, H. Perdreau-Dahl, I. Kjos, D. Jia, J. P. Morth, J. Neefjes, O. Bakke and C. Progida (2018). "TBC1D5 controls the GTPase cycle of Rab7b." Journal of Cell Science **131**(17): jcs216630.



- Borg, M., O. Bakke and C. Progida (2014). "A novel interaction between Rab7b and actomyosin reveals a dual role in intracellular transport and cell migration." Journal of Cell Science **127**(22): 4927-4939.
- Bournele, D. and D. Beis (2016). "Zebrafish models of cardiovascular disease." Heart Failure Reviews **21**(6): 803-813.
- Brocker, C., A. Kuhlee, C. Gatsogiannis, H. J. Kleine Balderhaar, C. Honscher, S. Engelbrecht-Vandre, C. Ungermann and S. Raunser (2012). "Molecular architecture of the multisubunit homotypic fusion and vacuole protein sorting (HOPS) tethering complex." Proceedings of the National Academy of Sciences **109**(6): 1991-1996.
- Bryant, D. M., A. Datta, A. E. Rodríguez-Fraticelli, J. Peränen, F. Martín-Belmonte and K. E. Mostov (2010). "A molecular network for de novo generation of the apical surface and lumen." Nature Cell Biology **12**(11): 1035-1045.
- Burger, A., H. Lindsay, A. Felker, C. Hess, C. Anders, E. Chiavacci, J. Zaugg, L. M. Weber, R. Catena, M. Jinek, M. D. Robinson and C. Mosimann (2016). "Maximizing mutagenesis with solubilized CRISPR-Cas9 ribonucleoprotein complexes." Development **143**(11): 2025-2037.
- Carroll, B., N. Mohd-Naim, F. Maximiano, Marieke, J. McCormack, M. Finelli, Sigrid, L. Perdios, R. Daigaku, Richard, C. Futter, I. Dikic and Vania (2013). "The TBC/RabGAP Armus Coordinates Rac1 and Rab7 Functions during Autophagy." Developmental Cell **25**(1): 15-28.
- Casie Chetty, S., M. S. Rost, J. R. Enriquez, J. A. Schumacher, K. Baltrunaite, A. Rossi, D. Y. R. Stainier and S. Sumanas (2017). "Vegf signaling promotes vascular endothelial differentiation by modulating etv2 expression." Developmental Biology **424**(2): 147-161.
- Castellano, B. M., A. M. Thelen, O. Moldavski, M. Feltes, R. E. N. Van Der Welle, L. Mydock-Mcgrane, X. Jiang, R. J. Van Eijkeren, O. B. Davis, S. M. Louie, R. M. Perera, D. F. Covey, D. K. Nomura, D. S. Ory and R. Zoncu (2017). "Lysosomal cholesterol activates mTORC1 via an SLC38A9-Niemann-Pick C1 signaling complex." Science **355**(6331): 1306-1311.
- Cauvin, C., M. Rosendale, N. Gupta-Rossi, M. Rocancourt, P. Larraufie, R. Salomon, D. Perrais and A. Echard (2016). "Rab35 GTPase Triggers Switch-like Recruitment of the Lowe Syndrome Lipid Phosphatase OCRL on Newborn Endosomes." Curr Biol **26**(1): 120-128.
- Caviglia, S., M. Brankatschk, E. J. Fischer, S. Eaton and S. Luschnig (2016). "Staccato/Unc-13-4 controls secretory lysosome-mediated lumen fusion during epithelial tube anastomosis." Nature Cell Biology **18**(7): 727-739.
- Chalfie, M., Y. Tu, G. Euskirchen, W. Ward and D. Prasher (1994). "Green fluorescent protein as a marker for gene expression." Science **263**(5148): 802-805.
- Chan, J., P. E. Bayliss, J. M. Wood and T. M. Roberts (2002). "Dissection of angiogenic signaling in zebrafish using a chemical genetic approach." Cancer Cell **1**(3): 257-267.
- Chehab, T., N. C. Santos, A. Holthenrich, S. N. Koerdt, J. Disse, C. Schuberth, A. R. Nazmi, M. Neeft, H. Koch, K. N. M. Man, S. M. Wojcik, T. F. J. Martin, P. Van Der Sluijs, N. Brose and V. Gerke (2017).

"A novel Munc13-4/S100A10/annexin A2 complex promotes Weibel–Palade body exocytosis in endothelial cells." Molecular Biology of the Cell **28**(12): 1688-1700.

Cook, N. R., P. E. Row and H. W. Davidson (2004). "Lysosome associated membrane protein 1 (Lamp1) traffics directly from the TGN to early endosomes." Traffic **5**(9): 685-699.

Corvera, S., A. D'Arrigo and H. Stenmark (1999). "Phosphoinositides in membrane traffic." Current Opinion in Cell Biology **11**(4): 460-465.

Davis, G. E. and K. J. Bayless (2003). "An Integrin and Rho GTPase-Dependent Pinocytic Vacuole Mechanism Controls Capillary Lumen Formation in Collagen and Fibrin Matrices." **10**(1): 27-44.

De Duve, C. (2005). "The lysosome turns fifty." Nature Cell Biology **7**(9): 847-849.

De Luca, M. and C. Bucci (2014). "A new V-ATPase regulatory mechanism mediated by the Rab interacting lysosomal protein (RILP)." Communicative & Integrative Biology **7**(5): e971572.

De Luca, M., L. Cogli, C. Progida, V. Nisi, R. Pascolutti, S. Sigismund, P. P. Di Fiore and C. Bucci (2014). "The Rab-interacting lysosomal protein (RILP) regulates vacuolar ATPase acting on the V1G1 subunit." Journal of Cell Science **127**(12): 2697-2708.

Deinhardt, K., S. Salinas, C. Verastegui, R. Watson, D. Worth, S. Hanrahan, C. Bucci and G. Schiavo (2006). "Rab5 and Rab7 Control Endocytic Sorting along the Axonal Retrograde Transport Pathway." Neuron **52**(2): 293-305.

Doherty, G. J. and H. T. McMahon (2009). "Mechanisms of Endocytosis." Annual Review of Biochemistry **78**(1): 857-902.

Dou, T., C. Ji, S. Gu, F. Chen, J. Xu, X. Ye, K. Ying, Y. Xie and Y. Mao (2005). "Cloning and Characterization of a novel splice variant of human Rab18 gene (RAB18)." DNA Sequence **16**(3): 230-234.

Echard, A., F. J. M. Opdam, H. J. P. C. De Leeuw, F. Jollivet, P. Savelkoul, W. Hendriks, J. Voorberg, B. Goud and J. A. M. Fransen (2000). "Alternative Splicing of the Human Rab6A Gene Generates Two Close but Functionally Different Isoforms." Molecular Biology of the Cell **11**(11): 3819-3833.

Escobar-Aguirre, M., Y. M. Elkouby and M. C. Mullins (2017). *Localization in Oogenesis of Maternal Regulators of Embryonic Development*, Springer International Publishing: 173-207.

Fetcho, J. R., K. J. A. Cox and D. M. O'Malley (1998). The Histochemical Journal **30**(3): 153-167.

Gagnon, J. A., E. Valen, S. B. Thyme, P. Huang, L. Ahkmetova, A. Pauli, T. G. Montague, S. Zimmerman, C. Richter and A. F. Schier (2014). "Efficient Mutagenesis by Cas9 Protein-Mediated Oligonucleotide Insertion and Large-Scale Assessment of Single-Guide RNAs." PLoS ONE **9**(5): e98186.

Gallien, S., E. Duriez, C. Crone, M. Kellmann, T. Moehring and B. Domon (2012). "Targeted proteomic quantification on quadrupole-orbitrap mass spectrometer." Molecular & cellular proteomics : MCP **11**(12): 1709-1723.

- Ge, X., D. Grotjahn, E. Welch, J. Lyman-Gingerich, C. Holguin, E. Dimitrova, E. W. Abrams, T. Gupta, F. L. Marlow, T. Yabe, A. Adler, M. C. Mullins and F. Pelegri (2014). "Hecate/Grip2a Acts to Reorganize the Cytoskeleton in the Symmetry-Breaking Event of Embryonic Axis Induction." PLoS Genetics **10**(6): e1004422.
- Gebala, V., R. Collins, I. Geudens, L.-K. Phng and H. Gerhardt (2016). "Blood flow drives lumen formation by inverse membrane blebbing during angiogenesis in vivo." Nature Cell Biology **18**(4): 443-450.
- Glass, A. S. and R. Dahm (2004). "The Zebrafish as a Model Organism for Eye Development." Ophthalmic Research **36**(1): 4-24.
- Griffiths, G., R. Back and M. Marsh (1989). "A quantitative analysis of the endocytic pathway in baby hamster kidney cells." Journal of Cell Biology **109**(6): 2703-2720.
- Grunwald, D. J., C. B. Kimmel, M. Westerfield, C. Walker and G. Streisinger (1988). "A neural degeneration mutation that spares primary neurons in the zebrafish." Developmental Biology **126**(1): 115-128.
- Guerra, F. and C. Bucci (2016). "Multiple Roles of the Small GTPase Rab7." Cells **5**(3): 34.
- Helker, C. S., A. Schuermann, C. Pollmann, S. C. Chng, F. Kiefer, B. Reversade and W. Herzog (2015). "The hormonal peptide Elabela guides angioblasts to the midline during vasculogenesis." eLife **4**.
- Henne, W. M., E. Boucrot, M. Meinecke, E. Evergren, Y. Vallis, R. Mittal and H. T. McMahon (2010). "FCHo Proteins Are Nucleators of Clathrin-Mediated Endocytosis." Science **328**(5983): 1281-1284.
- Herwig, L., Y. Blum, A. Krudewig, E. Ellertsdottir, A. Lenard, H.-G. Belting and M. Affolter (2011). "Distinct Cellular Mechanisms of Blood Vessel Fusion in the Zebrafish Embryo." Current Biology **21**(22): 1942-1948.
- Hogan, B. M., R. Herpers, M. Witte, H. Heloterä, K. Alitalo, H. J. Duckers and S. Schulte-Merker (2009). "Vegfc/Flt4 signalling is suppressed by Dll4 in developing zebrafish intersegmental arteries." Development **136**(23): 4001-4009.
- Horiuchi, H., R. Lippé, H. M. McBride, M. Rubino, P. Woodman, H. Stenmark, V. Rybin, M. Wilm, K. Ashman, M. Mann and M. Zerial (1997). "A Novel Rab5 GDP/GTP Exchange Factor Complexed to Rabaptin-5 Links Nucleotide Exchange to Effector Recruitment and Function." Cell **90**(6): 1149-1159.
- Howley, C. and R. K. Ho (2000). "mRNA localization patterns in zebrafish oocytes." Mechanisms of Development **92**(2): 305-309.
- Huotari, J. and A. Helenius (2011). "Endosome maturation." The EMBO Journal **30**(17): 3481-3500.

- Jayanandanan, N., R. Mathew and M. Leptin (2014). "Guidance of subcellular tubulogenesis by actin under the control of a synaptotagmin-like protein and Moesin." Nature Communications **5**(1).
- Jimenez-Orgaz, A., A. Kvainickas, H. Nägele, J. Denner, S. Eimer, J. Dengjel and F. Steinberg (2018). "Control of RAB 7 activity and localization through the retromer-TBC1D5 complex enables RAB 7-dependent mitophagy." The EMBO Journal **37**(2): 235-254.
- Kakahara, K., K. Shinmyozu, K. Kato, H. Wada and S. Hayashi (2008). "Conversion of plasma membrane topology during epithelial tube connection requires Arf-like 3 small GTPase in *Drosophila*." Mechanisms of Development **125**(3-4): 325-336.
- Kawamura, N., G.-H. Sun-Wada, M. Aoyama, A. Harada, S. Takasuga, T. Sasaki and Y. Wada (2012). "Delivery of endosomes to lysosomes via microautophagy in the visceral endoderm of mouse embryos." Nature Communications **3**(1): 1071.
- Kawauchi, T., K. Sekine, M. Shikanai, K. Chihama, K. Tomita, K.-I. Kubo, K. Nakajima, Y.-I. Nabeshima and M. Hoshino (2010). "Rab GTPases-Dependent Endocytic Pathways Regulate Neuronal Migration and Maturation through N-Cadherin Trafficking." Neuron **67**(4): 588-602.
- Kinchen, J. M. and K. S. Ravichandran (2010). "Identification of two evolutionarily conserved genes regulating processing of engulfed apoptotic cells." Nature **464**(7289): 778-782.
- Kohli, V., Jennifer, Sharina, K. Rehn and S. Sumanas (2013). "Arterial and Venous Progenitors of the Major Axial Vessels Originate at Distinct Locations." Developmental Cell **25**(2): 196-206.
- Kornfeld, S. and I. Mellman (1989). "The Biogenesis of Lysosomes." Annual Review of Cell Biology **5**(1): 483-525.
- Kuchitsu, Y. and M. Fukuda (2018). "Revisiting Rab7 Functions in Mammalian Autophagy: Rab7 Knockout Studies." Cells **7**(11): 215.
- Lagendijk, A. K., A. S. Yap and B. M. Hogan (2014). "Endothelial cell-cell adhesion during zebrafish vascular development." Cell Adhesion & Migration **8**(2): 136-145.
- Laue, K., S. Rajshekar, A. J. Courtney, Z. A. Lewis and M. G. Goll (2019). "The maternal to zygotic transition regulates genome-wide heterochromatin establishment in the zebrafish embryo." Nature Communications **10**(1).
- Lawrence, R. E. and R. Zoncu (2019). "The lysosome as a cellular centre for signalling, metabolism and quality control." Nature Cell Biology **21**(2): 133-142.
- Lawson, N. D. (2003). "phospholipase C gamma-1 is required downstream of vascular endothelial growth factor during arterial development." Genes & Development **17**(>11): 1346-1351.
- Lawson, N. D., R. Li, M. Shin, A. Grosse, O. Yukselen, O. A. Stone, A. Kucukural and L. Zhu (2020). "An improved zebrafish transcriptome annotation for sensitive and comprehensive detection of cell type-specific genes." eLife **9**.

- Lenard, A., E. Ellertsdottir, L. Herwig, A. Krudewig, L. Sauteur, H.-G. Belting and M. Affolter (2013). "In Vivo Analysis Reveals a Highly Stereotypic Morphogenetic Pathway of Vascular Anastomosis." Developmental Cell **25**(5): 492-506.
- Li, F., L. Yi, L. Zhao, A. Itzen, R. S. Goody and Y. W. Wu (2014). "The role of the hypervariable C-terminal domain in Rab GTPases membrane targeting." Proceedings of the National Academy of Sciences **111**(7): 2572-2577.
- Liu, G., P. Sanghavi, K. E. Bollinger, L. Perry, B. Marshall, P. Roon, T. Tanaka, A. Nakamura and G. B. Gonsalvez (2015). "Efficient Endocytic Uptake and Maturation in Drosophila Oocytes Requires Dynamitin/p50." Genetics **201**(2): 631-649.
- Mackiewicz, P. and E. Wyroba (2009). "Phylogeny and evolution of Rab7 and Rab9 proteins." BMC Evolutionary Biology **9**(1): 101.
- MacLean, B., D. M. Tomazela, N. Shulman, M. Chambers, G. L. Finney, B. Frewen, R. Kern, D. L. Tabb, D. C. Liebler and M. J. MacCoss (2010). "Skyline: an open source document editor for creating and analyzing targeted proteomics experiments." Bioinformatics (Oxford, England) **26**(7): 966-968.
- Madeira, F., Y. M. Park, J. Lee, N. Buso, T. Gur, N. Madhusoodanan, P. Basutkar, A. R. N. Tivey, S. C. Potter, R. D. Finn and R. Lopez (2019). "The EMBL-EBI search and sequence analysis tools APIs in 2019." Nucleic acids research **47**(W1): W636-W641.
- Marks, M. S., H. F. Heijnen and G. Raposo (2013). "Lysosome-related organelles: unusual compartments become mainstream." Current Opinion in Cell Biology **25**(4): 495-505.
- Marwaha, R., S. B. Arya, D. Jagga, H. Kaur, A. Tuli and M. Sharma (2017). "The Rab7 effector PLEKHM1 binds Arl8b to promote cargo traffic to lysosomes." The Journal of cell biology **216**(4): 1051-1070.
- Mascia, A., F. Gentile, A. Izzo, N. Mollo, M. De Luca, C. Bucci, L. Nitsch and G. Calì (2016). "Rab7 Regulates CDH1 Endocytosis, Circular Dorsal Ruffles Genesis, and Thyroglobulin Internalization in a Thyroid Cell Line." Journal of Cellular Physiology **231**(8): 1695-1708.
- Meeker, N. D., S. A. Hutchinson, L. Ho and N. S. Trede (2007). "Method for isolation of PCR-ready genomic DNA from zebrafish tissues." BioTechniques **43**(5): 610-614.
- Megason, S. G. and S. E. Fraser (2003). "Digitizing life at the level of the cell: high-performance laser-scanning microscopy and image analysis for in toto imaging of development." Mechanisms of Development **120**(11): 1407-1420.
- Mizoguchi, T., H. Verkade, J. K. Heath, A. Kuroiwa and Y. Kikuchi (2008). "Sdf1/Cxcr4 signaling controls the dorsal migration of endodermal cells during zebrafish gastrulation." Development **135**(15): 2521-2529.
- Murphy, R. F., S. Powers and C. R. Cantor (1984). "Endosome pH measured in single cells by dual fluorescence flow cytometry: rapid acidification of insulin to pH 6." Journal of Cell Biology **98**(5): 1757-1762.

- Naslavsky, N., M. Boehm, P. S. Backlund and S. Caplan (2004). "Rabenosyn-5 and EHD1 Interact and Sequentially Regulate Protein Recycling to the Plasma Membrane." Molecular Biology of the Cell **15**(5): 2410-2422.
- Naslavsky, N. and S. Caplan (2005). "C-terminal EH-domain-containing proteins: consensus for a role in endocytic trafficking, EH?" Journal of Cell Science **118**(18): 4093-4101.
- Naslavsky, N. and S. Caplan (2011). "EHD proteins: key conductors of endocytic transport." Trends in Cell Biology **21**(2): 122-131.
- Naslavsky, N., J. Rahajeng, M. Sharma, M. Jović and S. Caplan (2006). "Interactions between EHD Proteins and Rab11-FIP2: A Role for EHD3 in Early Endosomal Transport." Molecular Biology of the Cell **17**(1): 163-177.
- Nightingale, T. and D. Cutler (2013). "The secretion of von Willebrand factor from endothelial cells; an increasingly complicated story." Journal of Thrombosis and Haemostasis **11**(s1): 192-201.
- Norris, M. L., A. Pauli, J. A. Gagnon, N. D. Lord, K. W. Rogers, C. Mosimann, L. I. Zon and A. F. Schier (2017). "Toddler signaling regulates mesodermal cell migration downstream of Nodal signaling." eLife **6**.
- O'Brien, L. E., T.-S. Jou, A. L. Pollack, Q. Zhang, S. H. Hansen, P. Yurchenco and K. E. Mostov (2001). "Rac1 orientates epithelial apical polarity through effects on basolateral laminin assembly." Nature Cell Biology **3**(9): 831-838.
- Paatero, I., L. Sauter, M. Lee, A. K. Lagendijk, D. Heutschi, C. Wiesner, C. Guzmán, D. Bieli, B. M. Hogan, M. Affolter and H.-G. Belting (2018). "Junction-based lamellipodia drive endothelial cell rearrangements in vivo via a VE-cadherin-F-actin based oscillatory cell-cell interaction." Nature Communications **9**(1).
- Pankiv, S., E. A. Alemu, A. Brech, J.-A. Bruun, T. Lamark, A. Øvervatn, G. Bjørkøy and T. Johansen (2010). "FYCO1 is a Rab7 effector that binds to LC3 and PI3P to mediate microtubule plus end-directed vesicle transport." Journal of Cell Biology **188**(2): 253-269.
- Peterson, A. C., J. D. Russell, D. J. Bailey, M. S. Westphall and J. J. Coon (2012). "Parallel reaction monitoring for high resolution and high mass accuracy quantitative, targeted proteomics." Molecular & cellular proteomics : MCP **11**(11): 1475-1488.
- Pfeffer, S. R. (2017). "Rab GTPases: master regulators that establish the secretory and endocytic pathways." Molecular Biology of the Cell **28**(6): 712-715.
- Phng, L.-K. and H.-G. Belting (2021). "Endothelial cell mechanics and blood flow forces in vascular morphogenesis." Seminars in Cell & Developmental Biology.
- Poteryaev, D., S. Datta, K. Ackema, M. Zerial and A. Spang (2010). "Identification of the Switch in Early-to-Late Endosome Transition." Cell **141**(3): 497-508.
- Poteryaev, D., H. Fares, B. Bowerman and A. Spang (2007). "Caenorhabditis elegans SAND-1 is essential for RAB-7 function in endosomal traffic." The EMBO Journal **26**(2): 301-312.

- Progida, C., L. Cogli, F. Piro, A. De Luca, O. Bakke and C. Bucci (2010). "Rab7b controls trafficking from endosomes to the TGN." Journal of Cell Science **123**(9): 1480-1491.
- Reischauer, S., O. A. Stone, A. Villasenor, N. Chi, S.-W. Jin, M. Martin, M. T. Lee, N. Fukuda, M. Marass, A. Witty, I. Fiddes, T. Kuo, W.-S. Chung, S. Salek, R. Lerrigo, J. Alsjö, S. Luo, D. Tworus, S. M. Augustine, S. Mucenieks, B. Nystedt, A. J. Giraldez, G. P. Schroth, O. Andersson and D. Y. R. Stainier (2016). "Cloche is a bHLH-PAS transcription factor that drives haemato-vascular specification." Nature **535**(7611): 294-298.
- Rios-Barrera, L. D. and M. Leptin (2021). "An endosome-associated actin network involved in directed apical plasma membrane growth." bioRxiv: 2021.2001.2007.425786.
- Risau, W. (1997). "Mechanisms of angiogenesis." Nature **386**(6626): 671-674.
- Robinson, O., D. Dylus and C. Dessimoz (2016). "Phylo.io : Interactive Viewing and Comparison of Large Phylogenetic Trees on the Web." Molecular Biology and Evolution **33**(8): 2163-2166.
- Rodríguez-Fraticelli, A. E., J. Bagwell, M. Bosch-Forteza, G. Boncompain, N. Reglero-Real, M. J. García-León, G. Andrés, M. L. Toribio, M. A. Alonso, J. Millán, F. Perez, M. Bagnat and F. Martín-Belmonte (2015). "Developmental regulation of apical endocytosis controls epithelial patterning in vertebrate tubular organs." Nature Cell Biology **17**(3): 241-250.
- Rojas, R., T. Van Vlijmen, G. A. Mardones, Y. Prabhu, A. L. Rojas, S. Mohammed, A. J. R. Heck, G. A. Raposo, P. Van Der Sluijs and J. S. Bonifacino (2008). "Regulation of retromer recruitment to endosomes by sequential action of Rab5 and Rab7." Journal of Cell Biology **183**(3): 513-526.
- Sacharidou, A., A. N. Stratman and G. E. Davis (2012). "Molecular Mechanisms Controlling Vascular Lumen Formation in Three-Dimensional Extracellular Matrices." Cells Tissues Organs **195**(1-2): 122-143.
- Saftig, P. and J. Klumperman (2009). "Lysosome biogenesis and lysosomal membrane proteins: trafficking meets function." Nature Reviews Molecular Cell Biology **10**(9): 623-635.
- Sanford, J. C., Y. Pan and M. Wessling-Resnick (1995). "Properties of Rab5 N-terminal domain dictate prenylation of C-terminal cysteines." Molecular Biology of the Cell **6**(1): 71-85.
- Sauteur, L., A. Krudewig, L. Herwig, N. Ehrenfeuchter, A. Lenard, M. Affolter and H.-G. Belting (2014). "Cdh5/VE-cadherin Promotes Endothelial Cell Interface Elongation via Cortical Actin Polymerization during Angiogenic Sprouting." Cell Reports **9**(2): 504-513.
- Schier, A. F. (2001). "Axis formation and patterning in zebrafish." Current Opinion in Genetics & Development **11**(4): 393-404.
- Scott, C. C., F. Vacca and J. Gruenberg (2014). "Endosome maturation, transport and functions." Seminars in Cell & Developmental Biology **31**: 2-10.
- Shin, M., T. J. Beane, A. Quillien, I. Male, L. J. Zhu and N. D. Lawson (2016). "Vegfa signals through ERK to promote angiogenesis, but not artery differentiation." Development **143**(20): 3796-3805.

Solinger, J. A. and A. Spang (2013). "Tethering complexes in the endocytic pathway: CORVET and HOPS." FEBS Journal **280**(12): 2743-2757.

Stenmark, H. (2009). "Rab GTPases as coordinators of vesicle traffic." Nature Reviews Molecular Cell Biology **10**(8): 513-525.

Stenmark, H., R. G. Parton, O. Steele-Mortimer, A. Lütcke, J. Gruenberg and M. Zerial (1994). "Inhibition of rab5 GTPase activity stimulates membrane fusion in endocytosis." The EMBO Journal **13**(6): 1287-1296.

Streisinger, G., C. Walker, N. Dower, D. Knauber and F. Singer (1981). "Production of clones of homozygous diploid zebra fish (*Brachydanio rerio*)." Nature **291**(5813): 293-296.

Takei, K., V. I. Slepnev, V. Haucke and P. De Camilli (1999). "Functional partnership between amphiphysin and dynamin in clathrin-mediated endocytosis." Nature Cell Biology **1**(1): 33-39.

Torres-Vázquez, J., A. D. Gitler, S. D. Fraser, J. D. Berk, N. P. Van, M. C. Fishman, S. Childs, J. A. Epstein and B. M. Weinstein (2004). "Semaphorin-Plexin Signaling Guides Patterning of the Developing Vasculature." Developmental Cell **7**(1): 117-123.

Tung, J. J., I. W. Tattersall and J. Kitajewski (2012). "Tips, Stalks, Tubes: Notch-Mediated Cell Fate Determination and Mechanisms of Tubulogenesis during Angiogenesis." Cold Spring Harbor Perspectives in Medicine **2**(2): a006601-a006601.

Van Der Kant, R., A. Fish, L. Janssen, H. Janssen, S. Krom, N. Ho, T. Brummelkamp, J. Carette, N. Rocha and J. Neefjes (2013). "Late endosomal transport and tethering are coupled processes controlled by RILP and the cholesterol sensor ORP1L." Journal of Cell Science **126**(15): 3462-3474.

Verma, A., R. Bhattacharya, I. Remadevi, K. Li, K. Pramanik, G. V. Samant, M. Horswill, C. Z. Chun, B. Zhao, E. Wang, R. Q. Miao, D. Mukhopadhyay, R. Ramchandran and G. A. Wilkinson (2010). "Endothelial cell-specific chemotaxis receptor (ecscr) promotes angioblast migration during vasculogenesis and enhances VEGF receptor sensitivity." Blood **115**(22): 4614-4622.

Wacker, A. and H. Gerhardt (2011). "Endothelial development taking shape." Current Opinion in Cell Biology.

Wagner, D. D. and P. S. Frenette (2008). "The vessel wall and its interactions." Blood **111**(11): 5271-5281.

Weibel, E. R. and G. E. Palade (1964). "NEW CYTOPLASMIC COMPONENTS IN ARTERIAL ENDOTHELIA." The Journal of Cell Biology **23**(1): 101-112.

Wu, M., T. Wang, E. Loh, W. Hong and H. Song (2005). "Structural basis for recruitment of RILP by small GTPase Rab7." The EMBO Journal **24**(8): 1491-1501.

Zerial, M. and H. McBride (2001). "Rab proteins as membrane organizers." Nature Reviews Molecular Cell Biology **2**(2): 107-117.



Zhong, T. P., S. Childs, J. P. Leu and M. C. Fishman (2001). "Gridlock signalling pathway fashions the first embryonic artery." Nature **414**(6860): 216-220.

Zygmunt, T., Carl, J. Blondelle, Manvendra, Kathleen, Paula, L. Herwig, A. Krudewig, H.-G. Belting, M. Affolter, Jonathan and J. Torres-Vázquez (2011). "Semaphorin-PlexinD1 Signaling Limits Angiogenic Potential via the VEGF Decoy Receptor sFlt1." Developmental Cell **21**(2): 301-314.

## 12 Curriculum Vitae

# Daniel Heutschi, Ph.D.

*Elsässerstrasse 34, 4056 Basel | 09.09.1991 | Swiss | (+41) 079 576 43 17 |  
daniel.heutschi@hotmail.com | linkedin.com/in/daniel-heutschi/*

## Summary

---

Continuously eager to learn Ph.D. graduate with 7 years of experience in molecular biology laboratories. My independent and well prioritizing work style were useful for long and short running projects during my Ph.D. and my time in the Spiez laboratory. My caring nature makes me a reliable and dedicated worker as well as a fast learner and resilient problem solver. Due to my social skills and adaptability, I was able to integrate seamlessly in even the most diverse teams.



## Working experience:

---

From 08/2023

**Intern, FHNW MuttENZ, Switzerland, Research Group Laura Suter-Dick**

- Studying mitochondrial respiration rate using the Seahorse microwell analyser for human hepatocyte cell culture and isolated mitochondria

02/2022-11/2022:

**Postdoctoral Associate, University of Basel, Switzerland;  
Research Group Markus Affolter and Dr. Maria Kotini**

- Using high resolution long-term (>48 hours) light sheet microscopy to study endothelial junction architecture in the zebrafish brain vasculature
- Establishing advanced whole mount immunostainings and clearing protocols
- Collaborating with the in-house imaging facility to develop 3d multiview reconstruction scripts and training artificial intelligence for post-acquisition image processing of low signal imaging

03/2017-12/2021:

**Ph.D. candidate, Biozentrum, University of Basel, Switzerland;  
Research Group Markus Affolter**

- Extraction and purification of RNA, DNA and Protein from zebrafish embryos for RT-qPCR and regular PCR
- Validating the generated mutant zebrafish lines using targeted mass spectrometry in collaboration with the proteomics Core facility at the Biozentrum

- Using confocal and spinning disk confocal imaging to study the generated mutants and their effects on the formation of the zebrafish early vasculature
- Analysing the raw data using imaging analysis software and putting together a manuscript in preparation for publication
- Teaching and supervision of Bachelor students during courses and practicals and supervision of Matura students for their thesis

10/2015-08/2016:

### Scientific Associate during military duty, Labor Spiez, Spiez, Switzerland

- Planning and coordinating a nationwide tick survey from urban areas
- Preparation of 1100 tick samples with the MagNa Pure High-throughput-system

## Education:

12/2021	Ph.D. in Molecular Biology, Biozentrum, University of Basel, Switzerland  Developmental Biology, Prof. Dr. M. Affolter, <u>Thesis: "Genetic analysis of genes linked to lumen formation in the zebrafish vasculature"</u>
10/2015:	M.Sc. in Molecular Biology, Biozentrum, University of Basel, Switzerland  Developmental Biology, Prof. Dr. M. Affolter, <u>Thesis: "Mutagenesis of the Zebrafish <i>ve-cadherin</i> locus via the CRISPR/Cas9 genome editing technique"</u>
07/2014:	B.Sc. in Biology, University of Basel, Switzerland  Additional Courses in Physics, Mathematics, Nanoscience and basic Informatics

## Publications:

1. Daniel Heutschi, Etienne Schmelzer, Vahap Aydogan, Alexander Schmidt, Heinz-Georg Belting, Anne Spang, Markus Affolter, Maria P. Kotini; **Genetic analysis of rab7 mutants in zebrafish**; bioRxiv 2023.03.09.531857 (Submitted to G3 03/2023)
2. Jianmin Yin , Daniel Heutschi , Heinz-Georg Belting , Markus Affolter ; **Building the complex architectures of vascular networks: Where to branch, where to connect and where to remodel?**; *Curr Top Dev Biol*
3. Paatero, Ilkka, Sauteur, Loïc, Lee, Minkyung, Lagendijk, Anne K., Heutschi, Daniel, Wiesner, Cora, Guzmán, Camilo, Bieli, Dimitri, Hogan, Benjamin M., Affolter, Markus, Belting, Heinz Georg; **Junction-based lamellipodia drive endothelial cell rearrangements in vivo via a VE-cadherin-F-actin based oscillatory cell-cell interaction**; *Nature Communications*, 9(1)
4. Corinne P. Oechslin, Daniel Heutschi, Nicole Lenz, Werner Tischhauser, Olivier Péter, Olivier Rais, Christian M. Beuret, Stephen L. Leib, Sergei Bankoul, and Rahel Ackermann; **Prevalence of tick-borne pathogens in questing Ixodes ricinus ticks in urban and suburban areas of Switzerland**; *Parasite Vectors*

## References:

---

PhD supervisor:	Prof. Dr. Markus Affolter Mail: markus.affolter@unibas.ch Phone: +41 61 207 20 72
Supervisor as Technician:	Dr. Maria Kotini Mail: maria.kotini@unibas.ch Phone: +41 61 207 71 66
Supervisor in Spiez:	Dr. Rahel Ackermann Mail: rahel.ackermann@ne.ch Phone: +41 32 967 21 01

## Skills and interests:

---

Computer skills:	Proficient in <b>Mac and Windows</b> operating systems with basic knowledge of Linux and Ubuntu. Proficient in <b>Microsoft Office</b> with deeper understanding of Microsoft Excel, Word and PowerPoint and basic knowledge of LaTeX. Basic understanding of <b>programming with Python</b> <b>Additional Programs:</b> Adobe Illustrator, SnapGene, ImageJ, Fiji, Omero
Languages:	<b>German</b> (mother tongue), <b>English</b> (working language for 7years), <b>French</b> (good), <b>Italian</b> (basics)
Leadership experience:	<b>Fasnacht:</b> Instructing the kids and adults since 2009. Obmann (President) of the kids section since 2022 <b>Football:</b> Playing from 1996-2019 and refereeing the children from 2015-2019.